BLISTER FORMATION AND LAYER TRANSFER OF N-IMPLANTED GaAs

by

Rachel R. Collino

A dissertation submitted in partial fulfillment
of the requirements for the degree of
Doctor of Philosophy
(Mechanical Engineering)
in The University of Michigan
2010

Doctoral Committee:

Professor Michael Thouless, Co-Chair

Professor Rachel S. Goldman, Co-Chair

Professor Michael Atzmon

Assistant Professor Kevin P. Pipe

© Rachel R. Collino 2010
All Rights Reserved

ACKNOWLEDGEMENTS

I would like to thank my co-advisors, Michael Thouless and Rachel S. Goldman for their guidance, support, and encouragement. I would also like to thank my committee members Michael Atzmon and Kevin P. Pipe for their helpful discussion and suggestions.

Special thanks go to all of my fellow students in my ‘adopted’ department in Materials Science and Engineering, first and foremost the undergraduates that have worked with me on this project: Natalie Estrada, Brian Dick, Da Mao, Kai-Hsiung Tsao, and Ellen Burgunder. I would also like to thank my fellow Goldman group members including Xiaojun Weng, Yu Jin, Vaishno Dasika, Adam Wood, Jia-Hung Wu, Mike Warren, Justin Canniff, Weifeng Ye, and Leon Webster. Support from the National Science Foundation under grant CMMI-0700301, the AFOSR through the MURI program under Contract No. FA9950-08-1-0340, and graduate fellowships from the Michigan Memorial Phoenix Energy Institute and NSF are gratefully acknowledged.

Finally, I am indebted to my family, friends, and fiancé Jason, for their encouragement and support.

TABLE OF CONTENTS

ACKNOWLEDGEMENTS…………………………………………………..……ii

LIST OF TABLES……………………………………………………………...vii

LIST OF FIGURES……………………………………………………………viii

LIST OF APPENDICES………………………………………………..…..xix

ABSTRACT……………………………………………………………………xx

CHAPTER

1. INTRODUCTION…………………………………………..…..……1

1.1 Overview……………………………………………………….....1

1.2 Unique Physical Properties of Nanostructured Materials………2

1.3 N-incorporation in GaAs and Matrix Seeded Growth of Nanostructures…………………………………………………….3

1.4 Gas-ion-implantation-induced Blister Formation………………..5

1.5 Semiconductor Thin Film Integration and Layer Transfer……...6

1.6 Dissertation Objectives……………………………………………8

1.7 Outline of the Dissertation………………………………………..10

1.8 References……………………………………………………...13

2. EXPERIMENTAL PROCEDURES……………………………………..26

2.1 Overview…………………………………………………………26

2.2 Ion Implantation and Rapid Thermal Annealing………………..27

2.3 Scanning Electron Microscopy.……..…………………………..29

2.3.1 Environmental Scanning Electron Microscopy..…..…30

2.3.2 X-ray Energy Dispersive Spectroscopy……….…..…31

2.4 Atomic Force Microscopy…………………………………...…31

2.5 Ion Beam Analysis……………………………………..……32

2.5.1 Channeling-Rutherford Backscattering Spectrometry……………………………………………..33

2.5.2 Nuclear Reaction Analysis.……...……………………..34

2.6 Wafer Bonding…………………………………………….……37

2.7 Transmission Electron Microscopy…………………………...39

2.8 Nanoindentation………………………………………………..40

2.9 Characterization of Electrical and Thermal. Properties..……...41

2.9.1 Hall and Resistivity Measurements……..…..…………41

2.9.2 Seebeck Measurements………………………………..42

2.10 Wafer Curvature Measurements and Estimation of Implantation-induced Stress…………………………………………44

2.11 References……………………………………………………45

3. BLISTER FORMATION IN ION-IMPLANTED GaAs: ROLE OF DIFFUSIVITY……..…………………………………………………………64

3.1 Overview…………………………………………………………..64

3.2 Background……………………………………………………..65

3.3 Experiments and Simulations…………………..………………67

3.4 Surface Morphology and Retained N Fluence………………...68

3.5 Lattice Damage Profiles……..…………………………………..70

3.6 Diffusivity-driven Blister Formation…………….………………73

3.7 Conclusions………………………………………………………77

3.8 References………………………………………………………...79

4. MORPHOLOGY, ELECTRICAL, AND THERMAL PROPERTIES OF GaAs:N LAYERS……………………………………………………………..93

4.1 Overview……………………………………………….…………93

4.2 Background……………………………………….……………..94

4.2.1 Surface Buckle Formation……………………………...94

4.2.2 Electrical and Thermal Properties of III-V-material-based Nanocomposites………………………………………95

4.3 Experimental Details…………………………………………..…97

4.4 Surface Morphology of Annealed GaAs:N Layers.……………98

4.5 N-implantation-induced Stress in GaAs:N……………………101

4.6 N-implantation-induced Stiffness Reduction in GaAs:N…….104

4.7 Structure of Annealed GaAs:N Layers………………………..105

4.8 Electrical Properties of GaAs:N Films….……………………...107

4.9 Seebeck Coefficient of GaAs:N Films…..……………………..111

4.10 Conclusions………………………..……………………...112

4.11 References……………………..…………………………114

5. ION-CUT-SYNTHESIS OF GaAs:N NANOCOMPOSITE LAYERS…………………………………………………………………130

5.1 Overview…………………………………………………………130

5.2 Background......…………………………………………………131

5.2.1 Semiconductor Thin-film Materials Integration by Wafer Bonding……………………………………………131

5.2.2 Ion-cut…………………………………………………..132

5.2.3 Progress Toward Patterned Layer Transfer by Ion-cut………………………………………………………...133

5.3 Experimental Procedures………………………………………135

5.4 Bonding and Alternative Substrates…………………………...139

5.4.1 Materials Selection: Substrates for Layer Transfer..140

5.4.2 Materials Selection: Bonding Agent ………….……..142

5.5 Layer transfer of GaAs:N Nanocomposite Layers to Alumina and Aluminum Nitride Substrates………………………...…….146

5.6 Conclusions…………………………………………………..148

5.7 References……………………………………………………150

6. SUMMARY AND SUGGESTIONS FOR FUTURE WORK…………..170

6.1 Summary………………………………………………………170

6.2 Suggestions for Future Work………………………………...172

6.2.1 Thermal Conductivity of GaAs:N Nanocomposite Films…………………………………………………...…172

6.2.2 Alternative Substrates for Ion-cut-synthesis………..173

6.2.3 Photoluminescence of Transferred GaAs:N Layers……………………………………………….…..175

6.3 References……………………………………………………178

APPENDICES…………………………………………………......................183

LIST OF TABLES

Table

3.1 Comparison of reported diffusion parameters for various ions in GaAs and Si. In each case, the ion implantation or film growth details are listed along with the temperature T associated with diffusion parameters given by the Arrhenius expression $D = D_o\exp(-Q/RT)$, where D is the diffusivity or diffusion coefficient, D_0 is the diffusion coefficient pre-factor, Q is the activation energy for diffusion, and R is the gas constant (8.314 J-mol^{-1}K^{-1}). For comparison at a typical blister formation temperature, D is extrapolated to 300 °C where applicable. The estimated D(300 °C) of GaAs:N is orders of magnitude lower than that of other light ions in GaAs and Si (see references in table)…...……………………….75

4.1 Wafer curvature data for GaAs before and after N implantation. The radius of curvature, R, is determined from profilometry measurements of the spatial dependence of the surface height. The R values are averages (± standard deviation) of six surface scans for each sample. The significant decrease from R_i (before implantation) to R_f (after implantation) suggests a high implantation-induced residual stress……………………………………….....103

6.1 Compositions and properties of selected glasses for alternative substrates for ion-cut-synthesis. The softening point is the temperature at which glass will deform under its own weight. For comparison, the TEC of GaAs at room temperature is ~6.0x10^{-6} /°C…………………………………………………………………...174

LIST OF FIGURES

Figure

1.1 Predicted pseudo-binary phase diagram for the GaAs-GaN system, exhibiting a miscibility gap. In this diagram, x = 0 corresponds to GaAs and x = 1 corresponds to GaN, with the single-phase region corresponding to the alloy $GaAs_{1-x}N_x$. This alloy will tend to undergo spinodal decomposition, with the bimodal and spinodal lines indicated by the solid and dashed line, respectively. Reprinted figure with permission from J. Neugebauer and C. Van de Walle, Phys. Rev. B Vol. 51, 10568 (1995). Copyright 1995 by the American Physical Society…..…………………….…………………23

1.2 Ion beam synthesis of nitride nanostructures. In (a), a high dose of nitrogen ions (5.0×10^{17} cm^{-2} at 100 keV) is implanted into an epitaxial GaAs film to produce a supersaturated “amorphous” layer. In (b), after thermal annealing, nano-scale crystallites form within the disordered matrix………………………………..……………..24

1.3 Schematic of the ion-cut process for silicon-on-insulator materials integration. In (a), light ions are implanted into a donor Si wafer, which is subsequently bonded to a receiver Si wafer with an oxide intermediate layer. In (c), thermal annealing leads to the splitting of the donor wafer and transfer to the receiver wafer………………..25

2.1 Schematic of an ion implanter, adapted from Ref. 1. The system consists of an ion source, and accelerating column containing extraction electrodes. A magnetic mass separation system is used to separate the ion to be implanted from other charged particles and contaminants. Finally, electrostatic lenses are used to focus and direct the beam towards the target chamber…..……………..48

2.2 Diagram of the rapid thermal annealing setup. The sample sits on a silicon wafer with a thermocouple contact on the underside. The chamber is purged with flowing nitrogen or argon gas and the sample is heated by a halogen lamp housed inside a quartz window……………………………..……………………………….49

2.3 Schematic of electron emission near a sample surface feature, illustrating the origin of image contrast due to surface topography. The incident (scanning) electron paths are represented by solid lines and the emitted electrons by dashed lines. Electrons that are emitted in depressions in the sample surface may be blocked by higher surface features, creating a shadowing effect. Adapted from Ref. 4………………………..........……………………………….50

2.4 Schematic of electron-beam imaging of an electrically insulating sample in low-vacuum SEM. The imaging electrons collide with gaseous atoms (e.g., water vapor) introduced into the chamber, to generate additional electrons through ionization cascades. The electrons resulting from these cascades are collected by the positively biased detector. The corresponding positive ions drift to the sample, counteracting the negative charge build-up on the insulating surface. Adapted from Ref. 7……………….……….51

2.5 Components of an atomic-force microscope operating in tapping mode. Adapted from Ref. 8. ……………………………………….52

2.6 Geometry of a backscattering experiment, illustrating the collection of backscattered particles in a solid angle Ω. Adapted from Ref.12……………………………………………………….……..53

2.7 Channeling in (a) a perfect crystal, for which the incident ion undergoes only small-angle scattering within the channel. Dechanneling may occur when the incident ion interacts with lattice defects, as shown in (b). Adapted from Ref.11…….…..…………..54

2.8 Example of a nuclear reaction, illustrating the formation of a compound nucleus, which decays into a product nucleus and reaction product. The particles corresponding to the $^{14}N(d,\alpha)^{12}C$ reaction are labeled……………………….……………………………..55

2.9 NRA spectrum from N-implanted GaAs. The energies of the α_1 and α_0 reaction products are highlighted by dashed lines……………..56

2.10 $^{14}N(d,\alpha_1)^{12}C$ reaction cross-section as a function of energy. The relatively constant cross-section of the reaction between ~1.0 and ~1.3 MeV makes it convenient for depth-profiling measurements. Reprinted from Nuclear Instruments and Methods in Physics Research B, Vol. 219-220, S. Pellegrino, L. Beck, and Ph. Trouslard, "Differential cross-sections for nuclear reactions $^{14}N(d,p_5)^{15}N$, $^{14}N(d,p_0)^{15}N$, $^{14}N(d,\alpha_0)^{12}C$ and $^{14}N(d,\alpha_1)^{12}C$," pp. 140-144, Copyright 2004, with permission from Elsevier……………….57

2.11 Experimental setup for NRA. For retained dose measurements, a foil is placed in front of the detector and the sample tilted to a low incidence angle (channeling condition) to maximize penetration depth. For depth profiling, the sample is tilted to a non-channeling condition and no foil is used, to minimize energy straggling….…58

2.12 Spin-on glass (SOG) chemistries used in GaAs bonding…………59

2.13 SOG-mediated bonding procedure for GaAs(:N) materials integration..………………………………………….……………60

2.14 Schematic of the two-beam imaging condition in TEM. An incident electron beam may be transmitted or diffracted at the Bragg condition. An objective aperture is used to select either the transmitted beam for bright-field imaging or a diffracted beam for dark-field imaging……………………………………………………61

2.15 Van der Pauw sample geometry used for resistivity and Hall measurements. Typically, l = 5 mm and t = 600 μm. ~0.5 mm In contacts are deposited at the corners of the sample……………..62

2.16 Schematic of micro-thermocouple setup used to measure the Seebeck coefficient of GaAs:N samples. The sample is placed between a heat source (thermistor) and a heat sink; the temperature gradient at the sample surface (T_1-T_2) is measured by micro-thermocouple contacts. The resulting voltage difference due to the Seebeck effect is measured at indium contacts at the edges of the sample. ……………………………………………………..63

3.1 SEM images of (a) as-grown (b) annealed (c) high-*T*-implanted and (d) high-*T*-implanted-plus-annealed GaAs. Surface features are not apparent in both (a) as-grown and (c) high-*T*-implanted samples. For the (b) annealed and (d) high-*T*-implanted-plus-annealed films, surface pitting and blistering are apparent, respectively. Reprinted with permission from R. R. Collino et al., Appl. Phys. Lett. 95, 111912 (2009). Copyright 2009, American Institute of Physics.….84

3.2 X-ray Energy dispersive spectra of (a) as-grown (b) rapid-thermal annealed (850 °C in N_2) (c) as-implanted and (d) implanted-plus-annealed GaAs layers, with features corresponding to $L_{\alpha 1}$ (K_{α}) x-ray emission from Ga and As (O and C). The corresponding SEM images are shown as insets and represent the entire sampled area (~200 μm^2). The annealed surfaces exhibit apparent loss of As. In the case of the implanted + annealed layers, spot scans (not shown) revealed similar surface stoichiometries for elongated features and craters. All of the spectra shown were collected with incident electron energy of 5.0 keV, for a duration of 240 s…...….85

3.3 NRA spectra of α_1 particle yield vs. energy in low-*T* and high-*T*-implanted GaAs. The similarity of counts vs. energy between the two samples indicates that the retained fluence (estimated from integrated peak areas) and [N] depth profile are similar for both. Reprinted with permission from R. R. Collino et al., Appl. Phys. Lett. 95, 111912 (2009). Copyright 2009, American Institute of Physics……………………………………………………………….86

3.4 SEM (AFM) images of (a, (b)) low-*T*-implanted and (c, (d)) high-*T*-implanted-plus-annealed samples. SEM images in (a) and (c) reveal circular blisters and craters ~2 μm in diameter (highlighted with solid and dashed circles, respectively in (a)) for both low- and high-temperature implantations. AFM images of the same areas are shown in (b) and (d). The cross-sectional profiles reveal crater depths of ~200 nm in both cases. Reprinted with permission from R. R. Collino et al., Appl. Phys. Lett. 95, 111912 (2009). Copyright 2009, American Institute of Physics……………………………………87

3.5 Depth profile predicted by Monte Carlo simulations (SRIM Code) for 100 keV N^+ ions implanted at $5x10^{17}$ cm^{-2}. Inputs to the calculation included a 7° angle of incidence and 100,000 ions……….........88

3.6 (a) SEM image (52° sample tilt) of a blistered surface with both circular blisters and craters. A FIB trench (shown in the box) was fabricated to view near-surface layers in cross-section. (b) Detail of cross section, cut through both intact blisters as well as crater, showing that the apparent crater 'floor' coincides with the depth of blister formation, suggesting that the craters are remnants of popped blisters.…………………………..…………………………89

3.7 Channeling-RBS spectra as a function of backscattered energy of GaAs layers (a) before and (b) after annealing, comparing low-*T*- (open symbols) and high-*T*- (closed symbols) implanted samples with GaAs in the random and (001) aligned configurations. In both cases, the normalized yield is similar for the low-*T* and high-*T* samples, suggesting similar lattice damage. The implanted-plus-annealed spectra in (b) exhibit local maxima at ~1480 keV (corresponding to ~200 nm), attributed to dechanneling by bubbles. Reprinted with permission from R. R. Collino et al., Appl. Phys. Lett. 95, 111912 (2009). Copyright 2009, American Institute of Physics…………………………………………………….................90

3.8 Model of platelet and bubble formation in H-implanted Si. In the first step, implanted H is thought to occupy bond-centered sites in the silicon lattice. In the second step, themal annealing results in silicon hydride that aids in the formation of {100} platelets by passivating internal surfaces. In the third step, further annealing leads to the coalescence of H_2 gas bubbles, resulting in blister formation or splitting. Reprinted with permission from T. Höchbauer, A. Misra, M. Nastasi, and J. W. Mayer, J. Appl. Phys. **92**, 2335 (2002). Copyright 2002, American Institute of Physics..91

3.9 Schematic models of diffusion by (a-d) the kick-out mechanism and (e-h) the dissociative mechanism (vacancy-assisted). In the kick-out mechanism, an atom diffuses interstitially (a) until it “kicks out” the shaded atom on a lattice site (b). The process repeats itself in (c) and (d). In the dissociative mechanism, the shaded atom initially on a lattice site (e) diffuses interstitially, creating a mobile vacancy (f). Eventually the atom will recombine with a vacancy (g) and settle on another lattice site (h). Adapted from N. A. Stolwijk, Defect Diffus. Forum **95-98,** 895 (1993)……………..……..………92

4.1 SEM images of implanted-plus-annealed samples for implantation temperatures of -196 °C (first column) and 300 °C (second column), and annealing temperatures of (a,d) 800, (b,e) 850, and (c,f) 900 °C. For both implant temperatures, the 800 °C annealed surfaces consist of circular features: blisters and craters (popped blisters). At higher annealing temperatures, the surface features transition from circular to predominantly elongated features at 900 °C (highlighted with a dashed line)……………….. ……………..118

4.2 AFM surface profiles of (a) as-implanted, (b) implanted plus 800 °C annealed, and (c) implanted plus 900 °C annealed GaAs:N surfaces. In the as-implanted case, a relatively small surface roughness is observed (x40 scale). For the 800 °C annealed surface, circular blisters are observed, and for the 900 °C annealed surface, larger surface rumples are apparent.…………………..……119

4.3 (a) Plan view SEM image of an implanted plus 800 °C annealed film with circular features. FIB material removal was performed to image a crater and blister in cross-section in (b). Both features appear to delaminate at a depth of ~200 nm, in agreement with the simulated N ion range, suggesting that the circular features result from gas pressure-induced blistering.…………..……………….…120

4.4 (a) Plan view SEM image of an implanted plus 900 °C annealed film with elongated features. FIB material removal was performed to image the sub-surface structure in cross-section in (b), revealing two distinct delamination depths corresponding to the interface between the near-surface crystalline and nanocomposite layers, as well as a deeper delamination at the bubble layer. The strain in the top layer is estimated by $(L-L_o)/L_o$, where L_o is the apparent length of the deformed top layer and L is the un-deformed surface length, as estimated from line-traces shown in (c).…………………...…..121

4.5 SEM images of implanted plus (a) 800 °C and (b) 900 °C annealed samples after FIB line cuts were milled into a (a) circular and (b) elongated feature. In both cases, the top layer of the sample exhibits no apparent relaxation, suggesting permanent (plastic) deformation. ………………………………………………….……...122

4.6 Profilometer measurements across the surface a GaAs wafer before and after N-implantation. In both cases, a gradient in surface height is observed due to both intrinsic curvature and residual stresses, as shown schematically in the inset. The reduction in the surface height gradient (and consequently radius of curvature) is likely due to an increase in near-surface compressive stresses due to ion implantation……………………………….……..123

4.7 Load versus displacement measured by nanoindentation of as-grown and N-implanted GaAs films. Larger displacements are observed for implanted films versus as-grown films for similar loads, suggesting reduced stiffness of the implanted films……..124

4.8 Large-area cross-sectional TEM of an (a) implanted plus 800 °C annealed film and (b) implanted plus 900 °C annealed film, showing the relatively large deformation of the top polycrystalline layer in (b)……………………………..…………………….............125

4.9 (a) Bright-field and (b) {111} dark-field TEM images of implanted plus 900 ⁰C annealed GaAs:N layers. In (a), three distinct layers are apparent, including the delaminating polycrystalline layer, the nanocomposite layer, and the GaAs near-substrate layers. The nanocrystalline nature of the middle layer is shown by the dark-field image in (b). In (c), HRTEM of the top layer reveals its polycrystalline structure, as observed by the varying directions of lattice fringes. SAED of an area including the nanocomposite layer and near-substrate layers is shown in (d), revealing both crystalline diffraction spots from the substrate as well as spotty rings associated with {101} and {110} wurtzite GaN, as labeled in the pattern…..…………………….………………………………...........126

4.10 Resistivity versus free carrier concentration of GaAs(:N) layers for (a) implanted layers and (b) MBE-grown layers from Jin *et al*. (Ref. 38) and Yu *et al*. (Ref. 37), illustrating the more pronounced effect of annealing on n and ρ of Te-doped, N-implanted GaAs layers versus MBE-grown Te-doped or Si-doped GaAs layers. As a guide to the eye, an example of the sequence of processing steps (implantation, followed by annealing) is indicated by an arrow for a Si-doped sample……………..…………………………….............127

4.11 Resistivity versus free carrier concentration for all n-doped GaAs(:N) films. Dotted lines are drawn as a guide to the eye, to illustrate the increase in resistivity for implanted-plus-800 ⁰C annealed layers versus as-grown layers. For comparsion, resistivities of MBE-grown layers from Chin *et al.* (Ref. 40) are shown…………………………………..………………………..128

4.12 Seebeck coefficient versus carrier concentration for as-grown, implanted plus 800 ⁰C annealed, and implanted plus 900 ⁰C annealed n-doped GaAs:N films. For comparison, values from Refs. 41-43 for n-doped GaAs are shown……………..............129

5.1 Schematic of the ion-cut-synthesis process. In (a), an ion-implanted GaAs substrate is bonded to a new substrate with a spin-on glass (SOG) intermediate layer. In (b), following thermal annealing, the GaAs:N nanocomposite layer forms and splits from the GaAs substrate, and the layer transfer is accomplished……155

5.2 (a) A schematic of the geometry used in the blade test. In (b) and (c), IR microscopy images of SOG-bonded GaAs/GaAs pair (b) before and (c) after delamination are shown. Note that the region shown in (c) is well behind the crack front, as shown in the accompanying schematic…..…………………. ……….................156

5.3 Schematic of the IR microscope system. Infrared radiation from a halogen lamp is transmitted through the bonded sample, and captured by an IR-sensitive CCD camera.………………. …….....157

5.4 (a) Thermal expansion coefficient and (b) thermal conductivity for various ceramic materials and Si over a range of temperatures..158

5.5 Calculated values for the energy release rate for bonded samples (semiconductor or ceramic/GaAs) as the annealing temperature deviates from the bonding temperature, i.e., the temperature at which the mismatch strain is zero.…………..…...…………………....159

5.6 Surface morphology of a GaAs:N layer transferred to an alumina substrate using 1 μm "thick" MSSQ SOG. The SEM image of the surface in (a) reveals "mud" cracking. The depth of these cracks, as shown in the AFM of the same layer in (b), suggest that the cracks originate in the SOG layer. Thus, the cracking is likely due to tensile stress in the SOG layer......................….……….…....160

5.7 Surface morphology of a GaAs:N layer transferred to an alumina substrate using a "thin" MSSQ layer. In (a), an SEM image of the transferred layer. In (b), AFM of this transferred layer reveals 'hole' defects (highlighted by dashed circles) with depths approximately equal to the transferred layer thickness, suggesting that localized blister formation occurs instead of layer transfer, possibly due to reduced bonding quality...…………………………..........……......161

5.8 The variation of measured coefficient of thermal expansion (CTE) with composition for a methyltrimethoxysilane - 1,2-bis(triethoxysilyl)ethane (BTSE-MTMS) co-polymer used as a bonding agent. The CTE decreases with increasing BTSE content (lower x-axis). For comparison, the CTE of GaAs is ~6 / ^{o}C); thus, BTSE content > 50% is desirable for CTE-matching to GaAs. Reprinted from: H. W. Ro, K. Char, E.-C. Jeon, H.-J. Kim, D. Kwon, H.-J. Lee, J.-K. Lee, H.-W. Rhee, C. L. Soles, and D. Y. Yoon: High-modulus Spin-on Organosilicate Glasses for Nanoporous Applications. Advanced Materials **19**, p. 706. Copyright Wiley-VCH Verlag GmbH & Co. KGaA. Reproduced with permission…….....162

5.9 Surface morphology of a GaAs:N layer transferred to an alumina substrate using ~200 nm thick thermally-matched BTSE layer. In (a), an SEM image of the transferred layer, revealing the apparent elimination of hole defects. In (b), AFM of this transferred layer reveals reduced roughness in comparison to the layer transferred with the non-thermally-matched SOG………………………..……..163

5.10 SEM image of a GaAs:N layer transferred to an alumina substrate, illustrating the “patchy” morphology, with isolated areas of layer transfer in a fractal-like pattern……………………….……….......164

5.11 Schematic of the predicted crack trajectory (indicated by the dotted line) leading to the ‘patchy’ morphology layer transfer.………….....165

5.12 (a) schematic and (b) SEM image (52° tilt) of a GaAs:N layer transferred to a GaAs substrate using a BTSE-SOG bonding layer, illustrating the relatively large area of transfer..…………………..166

5.13 (a) Bright-field and (b) {111} dark-field XTEM images of a GaAs:N layer transferred to an alumina substrate. A selected-area electron diffraction pattern of the GaAs:N layer is shown as an inset in (a) and indicates the pre ……………………….……........................167

5.14 (a) Bright-field and (b) {111} dark-field XTEM images of a GaAs:N layer transferred to an aluminum nitride substrate, A selected-area electron diffraction pattern of the GaAs:N layer is shown as an inset in (a) and indicates the presence of cubic GaN crystallites in addition to zincblende GaAs……………………………………..168

5.15 High-resolution TEM micrographs of a GaAs:N layer transferred to (a) Al_2O_3 and (b) AlN substrates, illustrating the polycrystalline nature of the transferred layers. Several crystals with different orientations (suggested by lattice fringes) are highlighted with solid circles. The dashed-line circle shows apparent Moiré fringes, possibly due to the overlap of two crystals with different orientations..……………………………………........................169

6.1 Schematic of the sample geometry for the "3ω" measurement of the thermal properties of a film. A metallic line with contact pads is deposited on the film surface, and an AC current input at the outermost pads (indicated by the solid line) with frequency ω. The metal line acts as a heat source as well as a thermometer, due to its temperature-dependent resistivity. The voltage response ,which varies as 3ω, is measured at the inner contacts (indicated by the dashed line), and can be related to the thermal conductivity of the film. Adapted from Ref. 5....………...181

6.2 Photoluminesence spectra from GaAs:N layers still on the parent GaAs substrate ("not transferred") and GaAs:N layers transferred to an alumina substrate ("transferred")….......................................182

LIST OF APPENDICES

Appendix

A Data Analysis……………………………………………………………184

B Wafer Bonding Experiments……………………………….…………190

C Focused-ion-beam (FIB) Lift-out……………………………………202

D Materials Parameters……………………….………………………207

ABSTRACT

BLISTER FORMATION AND LAYER TRANSFER OF N-IMPLANTED GaAs

by

Rachel R. Collino

Co-chairs: Michael Thouless and Rachel S. Goldman

In this thesis, the blister formation and layer transfer of GaAs:N nanocomposite layers produced by N-implantation, wafer bonding, and rapid thermal annealing (RTA) of GaAs were investigated. In addition, we examined the electrical and thermal transport properties of GaAs:N nanocomposite layers.

To examine blister formation mechanisms, the influence of implantation temperature on blister exfoliation depths, lattice damage depth profiles, and N ion fluences was examined. For implantation temperatures of -196 and 300 ºC, we observed an implantation-temperature-insensitivity of blister formation, in contrast to reports of GaAs:H and Si:H, likely due to the lower GaAs:N ion-matrix

diffusivity in comparison to that of GaAs:H or Si:H. These results illustrate the key role of diffusivity on the mechanisms of blister formation.

The influence of post-implantation RTA on the surface morphology, electrical properties, and Seebeck coefficient of GaAs:N nanocomposite films was examined for RTA temperatures between 800 and 900 °C. A transition in surface morphology from circular to predominantly elongated features was observed, and attributed to two distinct delamination behaviors. The influence of implantation and RTA on the free carrier concentration, n, and resistivity, ρ, of GaAs:N(Si) and GaAs:N(Te) was examined. For GaAs:N, ρ follows a log-log dependence on n, independent of the dopant species and RTA conditions. Following implantation plus RTA, decreased n and increased ρ were observed for both dopant types with a more significant increase in ρ for the Te-doped GaAs:N layer. In addition, the Seebeck coefficient of the GaAs:N nanocomposite layer is enhanced in comparison to that of GaAs.

Finally, the demonstration and optimization of a new process for simultaneous nanostructuring and layer transfer, termed "ion-cut-synthesis," is described. Indeed, the low ion-matrix diffusivity of GaAs:N enabled the formation of both nanocrystals and gas bubbles at high temperature. In this technique, N ion implantation, spin-on glass-mediated wafer bonding, and RTA are used to achieve simultaneous nanostructuring and transfer of GaAs:N films to Al_2O_3 and AlN substrates. We identify the critical role of thermal-expansion coefficient matching on the success of the ion-cut-synthesis process.

CHAPTER 1

INTRODUCTION

1.1 Overview

For many semiconductor thin film applications, materials integration with alternative substrates such as other semiconductors, glasses, or ceramics may be necessary for thermal, electrical, and/or fiscal requirements. For example, the integration of thermoelectric sensors with low-thermal-conductivity substrates is desirable to avoid thermal losses into the support substrate.[1,2] In contrast, for power electronics, high-thermal-conductivity substrates are of interest for increasing heat dissipation and reliability.[3-5] In the cases of photovoltaics and thermoelectrics, nanostructured thin films are expected to enable record conversion efficiencies.[6] For these and other device-driven applications, materials cost is often a critical factor. Thus, the ability to integrate nanostructured thin films on cheaper support substrates is of interest for reducing capital costs.

Thin film materials integration may be accomplished by methods including direct deposition (e.g., epitaxy), wafer bonding, and epitaxial lift-off. In this thesis, a technique for the simultaneous synthesis and layer transfer of a

nanocomposite film by nitrogen implantation, wafer bonding, and annealing of GaAs is discussed.

This chapter opens with a description of the unique physical properties predicted and observed in nanocomposite materials. Next, we provide motivation for studies of N incorporation in GaAs and ion-beam synthesis of nanocomposites. This is followed by a review of gas-ion-implantation-induced blister formation and a summary of thin film materials integration techniques. Finally, the chapter concludes with an outline and objectives of the dissertation.

1.2 Unique Physical Properties of Nanostructured Materials

The physical properties of nanocomposites may be tailored for specific applications by controlling the concentrations and sizes of nanocrystals.[7,8] For example, quantum-confined heterostructures, including semiconductor quantum dots, have been observed to exhibit composition-[9] and size-dependent[10] optical properties. Low-dimensional structures are also predicted to lead to an increased thermoelectric figure-of-merit, *ZT*, in comparison to bulk materials. *ZT* is defined as:

$$ZT = S^2\sigma T/\kappa \qquad (1.1)$$

where σ is the electrical conductivity, *S* is the Seebeck coefficient, *T* is temperature, and κ is the thermal conductivity. In bulk materials, including non-degenerate semiconductors,[11] the electrical conductivity and electronic

contribution to the thermal conductivity (κ_e) are linked by the Weidemann Franz law:

$$\kappa_e/\sigma T = C_{WFL} \tag{1.2}$$

where C_{WFL} is a constant (the Wiedemann-Franz-Lorenz coefficient). Thus, for most bulk materials, an increase in σ corresponds to a proportional increase in κ_e, and thus minimal net benefit in terms of *ZT*. However, for quantum-confined structures, it has been predicted[12] and observed[13] that the electrical and thermal conductivities may be decoupled. For example, Dresselhaus *et al.*[13] reported a simultaneous increase in $S^2\sigma$ and decrease in κ for a SiGe nanocomposite in comparison with an alloy of the same composition. Indeed, increased phonon scattering at phase boundaries between the nanoparticles and the matrix is expected to lead to a decrease in thermal conductivity.[14,15] Both bulk[16,17] and thin-film[18] nanostructured semiconductor alloys have been reported to exhibit $ZT > 1$, attributed in part to phonon scattering at matrix/nanoparticle interfaces. Furthermore, the quantum confinement in nanoparticles, leading to a delta-like density of states (DOS) near the chemical potential (Fermi level), is expected to lead to an enhancement of *S*.[12,19]

1.3 N-incorporation in GaAs and Matrix Seeded Growth of Nanostructures

GaAsN and related alloys have exhibited significant N-composition-dependent band-gap bowing.[20-24] The resulting x-dependent decrease in band-

gap energy of $GaAs_{1-x}N_x$ makes these alloys attractive for applications including long-wavelength light emitters and detectors[25] as well as high-efficiency photovoltaics.[24] However, due to the predicted miscibility gap,[26,27] N incorporation is expected to be limited to x < ~1%, as shown in Fig. 1.1. In practice, < 5% N has been observed by film growth techniques,[28-30] with phase separation occurring at higher N compositions.[31] Recently, low-temperature MBE was used for the growth of $GaAs_{1-x}N_x$ films apparently across the entire composition range, namely amorphous $GaAs_{1-x}N_x$ films with x ranging from 0.17 to 0.75 and crystalline $GaAs_{1-x}N_x$ films for x < 0.17 and x > 0.75.[32] In addition, ion-beam synthesis, consisting of N implantation followed by thermal annealing, has been used to increase N incorporation in $GaAs_{1-x}N_x$ alloys,[33-35] up to x = 0.12. Similar ion-beam synthesis approaches have also been used to synthesize GaAsN nanocomposite materials consisting of GaN crystallites in a GaAs matrix,[36-38,53] with nanocrystallite sizes as small as ~5 nm, as shown schematically in Fig. 1.2.

To achieve zero-dimensional quantum confinement in nanostructures, quantum dots (QDs) with sizes less than or comparable to the exciton Bohr radius[39] are needed. In the case of GaN, values of the Bohr radius between 2.8 and 11 nm have been reported.[40-42] Yet, the smallest QDs obtained by Stranski-Krastanow (SK) growth range from 10 to 20 nm in diameter.[43-45] For SK growth, the sizes of the quantum dots are limited by the misfit strain between the film and substrate.[46,47] Although this inherent limitation does not hold for droplet epitaxy of QDs,[48] the smallest droplet epitaxy GaN dots reported to date have similar

diameters (~10 to 30 nm).[49-51] In contrast, as discussed above, QDs as small as ~5 nm are possible with ion-beam synthesis.[37,52,53] Thus, ion-beam synthesis is a promising route to the controlled formation of GaN nanostructures with zero-dimensional quantum confinement.

1.4 Gas-ion-implantation-induced Blister Formation

Following N implantation and annealing of GaAs, the formation of both GaN nanocrystals[52,53] and nitrogen gas bubbles[54] has been reported. Weng *et al.* observed nanocrystals near the predicted depth of maximum ion-induced lattice damage, nitrogen gas bubbles at the predicted depth of maximum ion concentration, and surface blister formation. Similar bubble and blister formation has been reported following light-ion-implantation, including H and/or He in Si[55-58] and GaAs.[59-61]

The introduction of gas ions into semiconductors has been regarded as both a nuisance and a benefit, depending on the application. For example, hydrogen, which is often introduced into semiconductors during film growth or subsequent processing steps, may interact with other impurities or defects, shifting their energy levels and affecting their electronic and optical properties.[62] On the other hand, voids produced by H and He in silicon have been utilized as a means of gettering undesirable metallic impurities[63-65] as well as providing sinks for point defects.[66] Bubble formation has also been studied as a means to modify the properties of insulating layers in integrated circuits. For example,

noble-gas (Kr, Xe) implantation into SiO_2 films has been used to generate cavities that decrease the dielectric constant.[67,68] Recently, bubble formation has also been exploited as a means of transferring a thin film in the 'ion-cut' process, as discussed in the next section.

1.5 Semiconductor Thin Film Integration and Layer Transfer

The integration of semiconductor thin films with alternative substrates can be accomplished by direct deposition or by wafer bonding techniques. In the case of GaAs, materials cost and/or functionality may drive the need for heterogeneous integration. For example, the integration of GaAs with silicon is of interest for GaAs-based optoelectronics coupled with silicon-based circuitry. However, the integration of crystalline GaAs by direct epitaxy is challenging due to both lattice and thermal expansion incompatibilities. For example, epitaxial growth of GaAs on silicon has been achieved,[69-72] but with high threading dislocation densities ($\sim 10^7$ cm^{-2}), limiting its usefulness as a basis for devices. One approach to improving heteroepitaxial crystalline quality is the use of a so-called compliant substrate.[73-75] In this technique, a buffer layer is used to accommodate some of the mismatch strain and prevent the generation and propagation of threading dislocations in the deposited film.

Layer transfer techniques utilizing wet chemical etching as a means for material removal include crystal ion slicing (CIS) and epitaxial lift-off (ELO). For CIS, He implantation into oxides such as lithium niobiate[76,77] and potassium

tantalate[78] leads to the formation of a damaged layer that preferentially etches in hydrofluoric acid. Thus, using CIS, a thin layer may be transferred while preserving the domain structure and crystalline quality of ferroelectric films. In ELO, a grown-in etch layer is used to remove an epitaxial film by selective chemical etching. This film is subsequently bonded to another substrate either directly[79] or through the use of intermediate layers.[80-82] ELO has been used to transfer GaAs to sapphire, silicon and plastic.[83] In a related process, laser lift-off (LLO), localized laser excitation is used to damage a weak bonding layer[84] or to precipitate gas bubbles,[85,86] thereby inducing delamination and layer transfer. However, both the ELO and LLO approaches are limited by film cracking, which tends to occur during the lift-off process.[87]

In 1995, Bruel[88] introduced an approach for the transfer of Si layers for silicon-on-insulator[89-93] (SOI) structures using H-ion implantation and thermal annealing, termed "ion-cut," or "Smart-cut." In this first incarnation of ion-cut, a hydrogen-implanted Si wafer is bonded to another oxidized Si wafer, and subsequently annealed. The resulting subsurface gas bubble formation acts as a "knife," cleaving off a thin layer of crystalline Si onto the oxide film, creating the SOI structure, as shown in Fig. 1.3. Thus, using ion-cut, many of the disadvantages of heteroepitaxial and lift-off approaches may be circumvented and new materials combinations are made possible.

Following the initial SOI application, the ion-cut technique has been expanded to include other light ions such as He,[94] D,[95] as well as H/He co-implantation.[96,97] Thus, many thin-film materials combinations have been

realized, including the transfer of InP to glass,[98] SiGe to Si,[99,100] SiC to Si[101] and glass,[102] GaSb to glass[103] and GaAs,[104] Ge to Si,[105] garnet to Si, InP, and GaAs,[106] and complex oxides such as $SrTiO_3$ to glass[107] and $LiNbO_3$ to silicon.[108] In GaAs, blistering and exfoliation have been observed using ion implantation of H,[108-111] D,[112] and co-implantation of H and He.[113] In the case of SOI, ion-cut has been implemented commercially,[114] and has expanded into the transfer of strain-engineered layers,[115] micro-electrical-mechanical systems fabrication,[116] and the transfer of Si layers to glass substrates[117,118] for display applications.

In the demonstrations of ion-cut to date, the sole function of the implanted ions has been to transfer an “unstructured” film; any patterning or synthesis of the transferred film occurs as a separate step. In this thesis work, we demonstrate a new technique for the simultaneous nanostructuring and transfer of a layer, termed “ion-cut-synthesis.”[54,119] This unique combination of ultra-small nanocrystal synthesis with the ability to transfer films to a variety of substrates is promising for new nanocomposite functionalities and materials combinations.

1.6 Dissertation Objectives

The first part of this thesis work focuses on the blister formation process in N-implanted GaAs. The influence of substrate temperature during implantation (“implantation temperature”) on blister formation behavior, namely, exfoliation

depths, lattice damage depth profiles, and retained N ion fluences, was examined. We observe implantation-temperature-independent blister formation, in contrast to reports of implantation-temperature-dependent blister formation in higher-diffusivity systems such as GaAs:H and Si:H. These results illustrate the key role of diffusivity on the mechanisms of blister formation, and support a qualitative model for blister formation that relies on implantation-induced extended defect formation and ion diffusivity.

The middle part of this thesis is devoted to investigations of the influence of post-implantation annealing on the surface morphology, structure, electrical, and thermal properties of GaAs:N films. In addition, the influence of implantation, annealing, N incorporation method, and dopant species on the free carrier concentration, resistivity and Seebeck coefficient of GaAs:N films is examined.

In the final part of this thesis, the demonstration and optimization of a new process for simultaneous nanostructuring and layer transfer, termed ion-cut-synthesis, is described. In this technique, N ion implantation, SOG-mediated wafer bonding, and rapid thermal annealing are used to achieve simultaneous nanostructuring and transfer of GaAs:N films to Al_2O_3 and AlN substrates. We identify the critical role of thermal-expansion-coefficient (TEC) matching on the success of the ion-cut-synthesis process.

1.7 Outline of the Dissertation

The dissertation is organized as follows. Following this introductory chapter, Chapter 2 describes the experimental procedures used for this thesis work, including ion implantation, wafer bonding, scanning electron microscopy (SEM), atomic force microscopy (AFM), channeling-Rutherford backscattering spectrometry (RBS), and nuclear reaction analysis (NRA) measurements.

In Chapter 3, the key role of diffusivity on blister formation in GaAs:N is revealed. The influence of the implantation temperature on the surface morphology is studied by SEM and AFM. The implantation-temperature-independence of surface blister formation is discussed and compared to higher-diffusivity systems such as GaAs:H and Si:H. We find that the exfoliation depth is independent of implantation temperature, in contrast to GaAs:H and Si:H. In addition, RBS and NRA reveal the implantation-temperature-independence of the lattice disorder and retained ion depth profiles. This behavior is likely due to the lower diffusivity of N in GaAs in comparison to that of H in GaAs and Si.

Chapter 4 presents investigations of the annealing temperature on the surface morphology and thermal and electrical transport properties of GaAs:N films. With increasing RTA temperature, a transition in the morphology of the GaAs:N surfaces from circular to elongated features is observed. SEM and TEM studies reveal that each surface feature is associated with its own distinct delamination depth. Following low-temperature RTA, delamination of the circular

features occurs at the observed depth of cavities, suggesting that the circular features are blisters induced by coalescence of N bubbles. However, following high-temperature RTA, delamination of the elongated features occurs at the interface between the near-surface polycrystalline and nanocomposite layers. The elongated features exhibit a high strain, presumably due to relaxation of the implantation-induced stress via a creep-assisted mechanism.

The influence of implantation and RTA on the free carrier concentration, n, and resistivity, ρ, of GaAs:N(Si) and GaAs:N(Te) were examined. For GaAs, ρ follows a log-log dependence on n, independent of the dopant species and RTA conditions, consistent with literature reports. Following implantation plus RTA, decreased n and increased ρ were observed for both dopant types with a more significant increase in ρ for the Te-doped GaAs:N layer. Finally, for the implanted plus RTA GaAs:N nanocomposite layers, the measured Seebeck coefficient is slightly enhanced in comparison to that of GaAs.

In Chapter 5, the successful demonstration and optimization of the ion-cut-synthesis technique is discussed. The nanostructuring and transfer of GaAs:N films to Al_2O_3 and AlN substrates is achieved using a spin-on glass (SOG) bonding agent. The critical role of TEC matching on achieving ion-cut-synthesis is discussed. First, the bonding problem is analyzed neglecting the thickness of the SOG layer. Immediately following the high-temperature annealing step, much of the original substrate has been removed and the SOG layer thickness is on the order of the transferred film thickness. In this case, the thickness and

TEC of the SOG have a significant impact on the morphology of the transferred film.

1.8 References

[1] W. H. Lee, Y. T. Lee, H. Takao, K. Sawada, and M. Ishida, Jpn. J. Appl. Phys. **46**, 7232 (2007).

[2] M.-Y. Kim and T.-S. Oh, J. Electron. Mater. **38**, 1176 (2009).

[3] W. Werdecker and F. Aldinger, IEEE Transactions on Components, Hybrids, and Manufacturing Technology **4,** 399 (1984).

[4] K. A. Moores and Y. K. Joshi, Future Circuits International **7**, 45 (2001).

[5] D. P. Long and C. S. Dulcey, J. Electrochem. Soc. **151**, G772 (2004).

[6] A. J. Nozik, Physica E **14**, 115 (2002).

[7] L. L. Beercroft, and C. K. Ober, Chem. Mater. **9**, 1302 (1997).

[8] L. Armelao, D. Barreca, G. Bottaro, A. Gasparotto, S. Gross, C. Maragno, and E. Tondello, Coord. Chem. Rev. **250**, 1294 (2006).

[9] W. Skorupa, L. Rebohle, and T. Gebel, Appl. Phys. A **76**, 1049 (2003).

[10] R. Lopez, T. E. Haynes, L. A. Boatner, L. C. Feldman, and R. F. Haglund Jr. Phys. Rev. B **65**, 224113 (2002).

[11] G. S. Nolas and H. J. Goldsmid, *Thermal Conductivity: Theory, Properties, and Applications*, T. M. Tritt, Ed., Kluwer Academic/Plenum, New York, 2004, p.106.

[12] G. D. Mahan and J. O. Sofo, Proc. Natl. Acad. Sci. U.S.A. **93**,7436 (1996).

[13] M. S. Dresselhaus, G. Chen, M. Y. Tang, R. Yang, H. Lee, D. Wang, Z. Ren, J.-P. Fleurial, and P. Gogna, Adv. Mater. **19**, 1043 (2007).

[14] L. D. Hicks and M. S. Dresselhaus, Phys. Rev. B **47**, 12727 (1993).

[15] L. D. Hicks and M. S. Dresselhaus, Phys. Rev. B **47**, 16631 (1993).

[16] T. C. Harman, P. J. Taylor, M. P. Walsh, and B. E. LaForge, Science **297**, 2229 (2002).

[17] K. F. Hsu, S. Loo, F. Guo, W. Chen, J. S. Dyck, C. Uher, T. Hogan, E. K. Polychroniadis, and M. G. Kanatzidis, Science **303**, 818 (2004).

[18] R. Venkatasubramanian, E. Siivola, T. Colpitts, and B. O'Quinn, Nature **413**, 597 (2001).

[19] J. P. Heremans, V. Jovovic, E. S. Toberer, A. Saramat, K. Kurosaki, A. Charoenphakdee, S. Yamanaka, and G. J. Snyder, Science **321**, 554 (2008).

[20] L. Bellaiche, S.-H. Wei, and A. Zunger, Phys. Rev. B. **54**, 17568 (1996).

[21] W. G. Bi and C. W. Tu, Appl. Phys. Lett. **70**, 1608 (1997).

[22] Y. Zhao, F. Deng, S. S. Lau, and C. W. Tu, J. Vac. Sci. Technol. B **16**, 1297 (1998).

[23] K. Uesugi, N. Morooka, and I. Suemune, Appl. Phys. Lett. **74**, 1254 (1999).

[24] I. A. Buyanova, W. M. Chen, and B. Monemar, MRS Internet J. Nitride Semicond. Res. **6**, 1 (2001).

[25] M. Kondow, T. Kitatani, S. Nakatsuka, M. C. Larson, K. Nakahara, Y. Yazawa, M. Okai, and K. Uomi, IEEE J. Sel. Areas. Commun. **3**, 719 (1997).

[26] J. Neugebauer and C. Van de Walle, Phys. Rev. B **51,** 10568 (1995).

[27] I. Ho and G. B. Stringfellow, J. Cryst. Growth **178,** 1 (1997).)

[28] Y. Zhao, G. Chen, S. Wang, and S. F. Yoon, Thin Solid Films **450**, 352 (2004).

[29] M. Weyers and M. Sato, Appl. Phys. Lett. **62**, 1396 (1993).

[30] Y. Qiu, S. A. Nikishin, H. Temkin, N. N. Fleev, and Y. A. Kudriavtsev, Appl. Phys. Lett. **70**, 3242 (1997).

[31] Y. Xin, P. D. Brown, R. E. Dunin-Brokowski, C. J. Humphreys, T. S. Cheng, and C. T. Foxon, J. Cryst. Growth **171**, 321 (1997).

[32] K. M. Yu, S. V. Novikov, R. Broesler, I. N. Demchenko, J. D. Denlinger, Z. Liliental-Weber, F. Luckert, R. W. Martin, W. Walukiewicz, and C. T. Foxon, J. Appl. Phys. **106**, 103709 (2009).

[33] T. Shima, S. Kimura, T. Iida, A. Obara, Y. Makita, K. Kudo, and K. Tanaka, Nucl. Instrum. Methods Phys. Res. B **118**, 743 (1996).

[34] W. Shan, K. M. Yu, W. Walukiewicz, J. W. Ager III, E. E. Haller, and M. C. Ridgway, Appl. Phys. Lett. **75**, 1410 (1999).

[35] K. M. Yu, W. Walukiewicz, J. Wu, J. W. Beeman, J. W. Ager III, E. E. Haller, W. Shan, H. P. Xin, C. W. Tu, and M. C. Ridgway, J. Appl. Phys. **90**, 2227 (2001).

[36] S. Amine, G. Ben Assayag, C. Bonafos, B. de Mauduit, H. Hidriss, A. Claverie, Mater. Sci. Eng. B **93**, 10 (2002).

[37] X. W. Lin, M. Behar, R. Maltez, W. Swider, Z. Liliental-Weber, and J. Washburn, Appl. Phys. Lett. **67**, 2699 (1995).

[38] K. Kuriyama, T. Tsunoda, N. Hayashi, and Y. Takahashi, Nucl. Instrum. Methods Phys. Res. B **148**, 432 (1999).

[39] Y. Matsumoto and T. Takagahara, *Semiconductor Quantum Dots: Physics, Spectroscopy, and Applications* (Springer-Verlag, Heidelberg, 2002), Chapter 2.

[40] P. Ramvall, S. Tanaka, S. Nomura, P. Riblet, and Y. Aoyagi, Appl. Phys. Lett. **73**, 1104 (1998).

[41] J. Zhang, L. D. Zhang, X. F. Wang, C. H. Liang, X. S. Peng, and Y. W. Wang, J. Chem. Phys. **115**, 5714 (2001).

[42] J.-W. Yoon, S. H. Shim, K. B. Shim, N. Koshizaki, and Y.-S. Kwon, Jpn. J. Appl. Phys. **44**, 788 (2005).

[43] X.-Q. Shen, S. Tanaka, S. Iwai, and Y. Aoyagi, Appl. Phys. Lett. **72**, 344 (1998).

[44] C. Adelmann, J. Simon, G. Feuillet, N. T. Pelekanos, B. Daudin, and G. Fishman, Appl. Phys. Lett. **76**, 1570 (2000).

[45] F. Widmann, J. Simon, B. Daudin, G. Feuillet, J. L. Rouvière, N. T. Pelekanos, and G. Fishman, Phys. Rev. B **58**, 15989 (1998).

[46] J. Tersoff, Phys. Rev. Lett. **81**, 3183 (1998).

[47] J. Tersoff and F. K. LeGoues, Phys. Rev. Lett. **72**, 3570 (1994).

[48] S. Naritsuka, T. Kondo, H. Otsubo, K. Saitoh, Y. Yamamoto, and T. Maruyama, J. Cryst. Growth **300**, 118 (2007).

[49] T. Kondo, K. Saitoh, Y. Yamamoto, T. Maruyama, and S. Naritsuka, Phys. Stat. Sol. A **203**, 1700 (2006).

[50] A. S. Özcan, Y. Wang, G. Ozaydin, K. F. Ludwig, A. Bhattacharyya, T. D. Moustakas, and D. P. Siddons, J. Appl. Phys. **100**, 084307 (2006).

[51] T. Maruyama, H. Otsubo, T. Kondo, Y. Yamamoto, and S. Naritsuka, J. Cryst. Growth **301-302**, 486 (2007).

[52] X. Weng, S. J. Clarke, W. Ye, S. Kumar, R. S. Goldman, A. Daniel, R. Clarke, J. Holt, J. Sipowska, A. Francis, and V. Rotberg, J. Appl. Phys. **92**, 4012 (2002).

[53] X. Weng, W. Ye, S. J. Clarke, R. S. Goldman, V. Rotberg, A. Daniel, and R. Clarke, J. Appl. Phys. **97**, 064301 (2005).

[54] X. Weng, W. Ye, R.S. Goldman, and J.C. Mabon, J. Vac. Sci. Technol. B **22**, 989 (2004).

[55] W. Primak and J. Luthra, J. Appl. Phys. **37**, 2287 (1966).

[56] M. Zhang, L. Wang, Z. Zhou, Z. Lin, and C. Lin, Phys. Stat. Sol. A **165**, 361 (1988).

[57] C. Qian and B. Terreault, J. Appl. Phys. **90**, 5152 (2001).

[58] S. Frabboni, G. C. Gazzadi, L. Felisari, R. Tonini, F. Corni, and G. Ottaviani, Appl. Phys. Lett. **85**, 1683 (2004).

[59] D. M. Follstaedt, S. M. Meyers, J. C. Barbour, G. A. Petersen, J. L. Reno, L. R. Dawson, and S. R. Lee, Nucl. Instrum. Methods Phys. Res. B **160**, 476 (2000).

[60] L. Di Cioccio, E. Jalaguier, and F. Letertre, Phys. Stat. Sol. A **202**, 509 (2005).

[61] A. Giguère, N. Desrosiers, and B. Terreault, Nucl. Instrum. Methods Phys. Res. B **242**, 620 (2006).

[62] S. K. Estreicher, Acta Phys. Pol. A **102**, 513 (2002).

[63] J. Wong-Leung, C. E. Ascheron, M. Petravic, R. G. Elliman, and J. S. Williams, Appl. Phys. Lett. **66**, 1231 (1995).

[64] V. Raineri, P. G. Fallica, G. Percolla, A. Battaglia, M. Barbagallo, and S. U. Campisano, J. Appl. Phys. **78**, 3727 (1995).

[65] V. Raineri, M. Saggio, and E. Rimini, J. Mater. Res. **15**, 1449 (2000).

[66] V. Raineri and S. U. Campisano, Appl. Phys. Lett. **69**, 1783 (1996).

[67] H. Assaf, E. Ntsoenzok, M.-F. Barthe, M.-O. Rualt, T. Sauvage, and S. Ashok, Nucl. Instrum. Methods Phys. Res. B **253**, 222 (2006).

[68] H. Assaf, E. Ntsoenzok, E. Leoni, M. F. Barthe, M. O. Rualt, O. Kaitasov, and S. Ashok, Electrochem. Solid-State Lett. **10**, G72 (2007).

[69] E. A. Fitzgerald, J. Vac. Sci. Technol. B **7,** 782 (1989).

[70] H. L. Tsai and Y. C. Kao, J. Appl. Phys. **67**, 2862 (1990).

[71] P. J. Taylor, W. A. Jesser, J. D. Benson, M. Martinks, J. H. Dinan, J. Bradshaw, M. Lara-Taysing, R. P. Leavitt, G. Simonis, W. Chang, W. W. Clark, and K. A. Bertness, J. Appl. Phys. **89**, 4365 (2001).

[72] R. D. Bringans, D. K. Biegelsen, L.-E. Swartz, F. A. Ponce, and J. C. Tramontana, Appl. Phys. Lett. **61**, 195 (1992).

[73] Y. H. Lo, Appl. Phys. Lett. **59**, 2331 (1991).

[74] D. Teng and Y. H. Lo, Appl. Phys. Lett. **62**, 43 (1993).

[75] G. Kästner, U. Gösele, and T. Y. Tan, Appl. Phys. A **66**, 13 (1998).

[76] M. Levy, R. M. Osgood, Jr., R. Liu, L. E. Cross, G. S. Cargill III, A. Kumar, and H. Bakhru, Appl. Phys. Lett. **73**, 2293 (1998).

[77] D. W. Ward, E. R. Statz, K. A. Nelson, R. M. Roth, and R. M. Osgood, Appl. Phys. Lett. **86**, 022908 (2005).

[78] M. Levy, R. M. Osgood Jr., A. S. Bhalla, R. Guo, L. E. Cross, A. Kumar, S. Sankaran, and H. Bakhru, Appl. Phys. Lett. **77**, 2124 (2000).

[79] E. Yablonovitch, T. Gmitter, J. P. Harbison, and R. Bhat, Appl. Phys. Lett. **51**, 2222 (1987)

[80] T. Soga, T. Jimbo, J. Arokiaraj, and M. Umeno, Appl. Phys. Lett. **77**, 3947 (2000).

[81] C. Camperiginestet, Y. W. Kim, N. M. Jokerst, M. G. Allen, and M. A. Brooke, IEEE Photon. Technol. Lett. **4**, 1003 (1992).

[82] F. Omnes, J.-C. Guillaume, G. Nataf, D. Jager-Waldau, P. Vennegues, and P. Gibart, IEEE Trans. Electron. Dev. **43**, 1806 (1996).

[83] R. Adam, M. Mikulicks, X. Zheng, M. Marso, I. Camara, F. Siebe, R. Güsten, A. Förster, P. Kordŏs, and R. Sobolewski, Proc. SPIE **5352**, 321 (2004).

[84] L. Tsakalakos and T. Sands, Appl. Phys. Lett. **76**, 227 (2000).

[85] M. K. Kelly, O. Ambacher, R. Dimitrov, R. Handschuh, and M. Stutzmann, Phys. Stat. Sol. A **159**, R3 (1996).

[86] W. S. Song, T. Sands, and N. W. Cheung, Appl. Phys. Lett. **72**, 599 (1998).

[87] P. R. Tavernier and D. R. Clarke, J. Appl. Phys. **89**, 1527 (2001).

[88] M. Bruel, Electron. Lett. **31**, 1201 (1995).

[89] M. Bruel, Nucl. Instrum. Methods Phys. Res. B **108**, 313 (1996).

[90] M. Bruel, B. Aspar, and A.-J. Auberton-Hervé, Jpn. J. Appl. Phys. **36**, 1636 (1997).

[91] B. Aspar, M. Bruel, H. Moriceau, C. Maleville, T. Poumeyrol, A. M. Papon, A. Claverie, G. Benassayag, A. J. Auberton-Hervé, and T. Barge, Microelectron. Eng. **36**, 233 (1997).

[92] V. P. Popov, I. V. Antonova, V. F. Stas, L. V. Mironova, A. K. Gutakovskii, E. V. Spesivtsev, A. S. Mardegzhov, A. A. Franznusov, and G. N. Feofanov, Mater. Sci. Eng. B **73**, 82 (2000).

[93] H. J. Woo, H. W. Choi, J. K. Kim, G. D. Kim, W. Hong, W. B. Choi, and Y. H. Bae, Nucl. Instrum. Methods Phys. Res. B **241**, 531 (2005).

[94] X. Lu, S. K. Iyer, J. Min, Z. Fan, J. B. Liu, P. K. Chu, C. Hu, and N. W. Chueng, IEEE International SOI Conference, Sanibel Island, Florida, 48, (1996).

[95] N. Desrosiers and B. Terreault, Appl. Phys. Lett. **89**, 151922 (2006).

[96] A. Agarwal, T. E. Haynes, V. C. Venezia, O. W. Holland, and D. J. Eaglesham, Appl. Phys. Lett. **72**, 1086 (1998).

[97] P. Nguyen, I. Cayrefourcq, K. K. Bourdelle, A. Boussagol, E. Guiot, N. Ben Mohamed, N. Sousbie, and T. Akatsu, J. Appl. Phys. **97**, 083527 (2005).

[98] W. Chen, A. Zhang, P. Chen, J. E. Pulsifer, T. L. Alford, T. F. Kuech, and S. S. Lau, Appl. Phys. Express **2**, 022201 (2009).

[99] L. J. Huang, J. O. Chu, D. F. Canaperi, C. P. D’Emic, R. M. Anderson, S. J. Koester, and H.-S. P. Wong, Appl. Phys. Lett. **78**, 1267 (2001).

[100] H. Moriceau, F. Fournel, B., B. Bataillou, A. Beaumont, C. Morales, A. M. Cartier, S. Pocas, C. Lagahe, E. Jalaguier, A. Soubie, B. Biasse, N. Sousbie, S. Sartori, J. F. Michaud, F. Letertre, O. Rayssac, I. Cayrefourcq, C. Richtarch, N. Daval, C. Aulnette, T. Akatsu, B. Osternaud, B. Ghyselen, and C. Mazuré, J. Electron. Mater. **32**, 829 (2003).

[101] L. Di Cioccio, F. Letertre, Y. Le Tiec, A. M. Papon, C. Jaussard, and M. Bruel, Mater. Sci. Eng. B **46**, 349 (1997).

[102] Q.-Y. Tong, T.-H. Lee, L.-J. Huang, Y.-L. Chao, and U. Gösele, Electron. Lett. **34**, 407 (1998).

[103] K. D. Hobart and F. J. Kub, Electron. Lett. **35**, 675 (1999).

[104] Y. Zheng, P. D. Moran, Z. F. Guan, S. S. Lau, D. M. Hansen, T. F. Kuech, T. E. Haynes, T. Hoechbauer, and M. Nastasi, J. Electron. Mater. **29**, 916 (2000).

[105] J. M. Zahler, C.- G. Ahn, S. Zaghi, H. A. Atwater, C. Chu, and P. Iles, Thin Solid Films **403-404**, 558 (2002).

[106] T. Izuhara, M. Levy, and R. M. Osgood, Jr. Appl. Phys. Lett. **76**, 1261 (2000).

[107] F. J. Kub, K. D. Hobart, J. M. Pond, and S. W. Kirchoefer, Electron. Lett. **35**, 477 (1999).

[108] B. Aspar, H. Moriceau, E. Jalaguier, C. Lagahe, A. Soubie, B. Biasse, A. M. Papon, A. Claverie, J. Grisolia, G. Benassayag, F. Letertre, O. Rayssac, T. Barge, C. Maleville, and B. Ghyselen, J. Electron. Mater. **30**, 834 (2001).

[109] G. Gawlik, J. Jagielski, and B. Piatkowski, Vacuum **70**, 103 (2003).

[110] M. Webb, C. Jeynes, R. M. Gwilliam, Z. Tabatabaian, A. Royle, and B. J. Sealy, Nucl. Instrum. MethodsPhys. Res. B **237**, 193 (2005).

[111] M. Webb, C. Jeynes, R. Gwilliam, P. Too, A. Kozanecki, J. Domagala, A. Royle, and B. Sealy, Nucl. Instrum. Methods Phys. Res. B **240**, 142 (2005).

[112] A. Giguère, N. Desrosiers, and B. Terreault, Appl. Phys. Lett. **87**, 211911 (2005).

[113] I. Radu, I. Szafraniak, R. Scholz, M. Alexe, and U. Gösele, J. Appl. Phys. **94**, 7820 (2003).

[114] W. G. En, I. J. Malik, M. A. Bryan, S. Farrens, F. J. Henley, N. W. Cheung, and C. Chan, Proc. IEEE International SOI Conference, Stuart, FL, p.163 (1998).

[115] B. Ghyselen *et al.*, Solid State Electron. **48**, 1285 (2004).

[116] J. Du, W. H. Ko, and D. J. Young, Sensor. Actuat. A **112**, 116 (2004).

[117] M. Cai, D. Qiao, L. S. Yu, S. S. Lau, C. P. Li, L. S. Hung, T. E. Haynes, K. Henttinen, I. Suni, V. M. C. Poon, T. Marek, and J. W. Mayer, J. Appl. Phys. **92**, 3388 (2002).

[118] F. Lu, D. Qiao, M. Cai, P. K. L. Yu, S. S. Lau, R. K. Y. Fu, L. S. Huang, C. P. Li, P. K. Chu, H. C. Chien, and Y. Liou, J. Vac. Sci. Technol. **B**, 2109, (2003).

[119] X. Weng and R. S. Goldman, U.S. Patent No. 7,056,815 (6 June 2006).

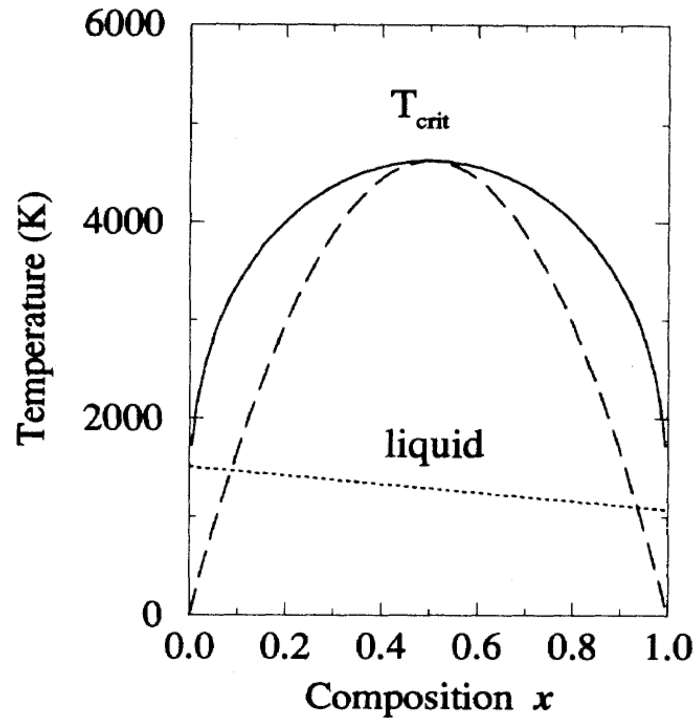

Fig. 1.1 Predicted pseudo-binary phase diagram for the GaAs-GaN system, exhibiting a miscibility gap. In this diagram, x = 0 corresponds to GaAs and x = 1 corresponds to GaN, with the single-phase region corresponding to the alloy $GaAs_{1-x}N_x$. This alloy will tend to undergo spinodal decomposition, with the bimodal and spinodal lines indicated by the solid and dashed line, respectively. Reprinted figure with permission from J. Neugebauer and C. Van de Walle, Phys. Rev. B Vol. 51, 10568 (1995). Copyright 1995 by the American Physical Society.

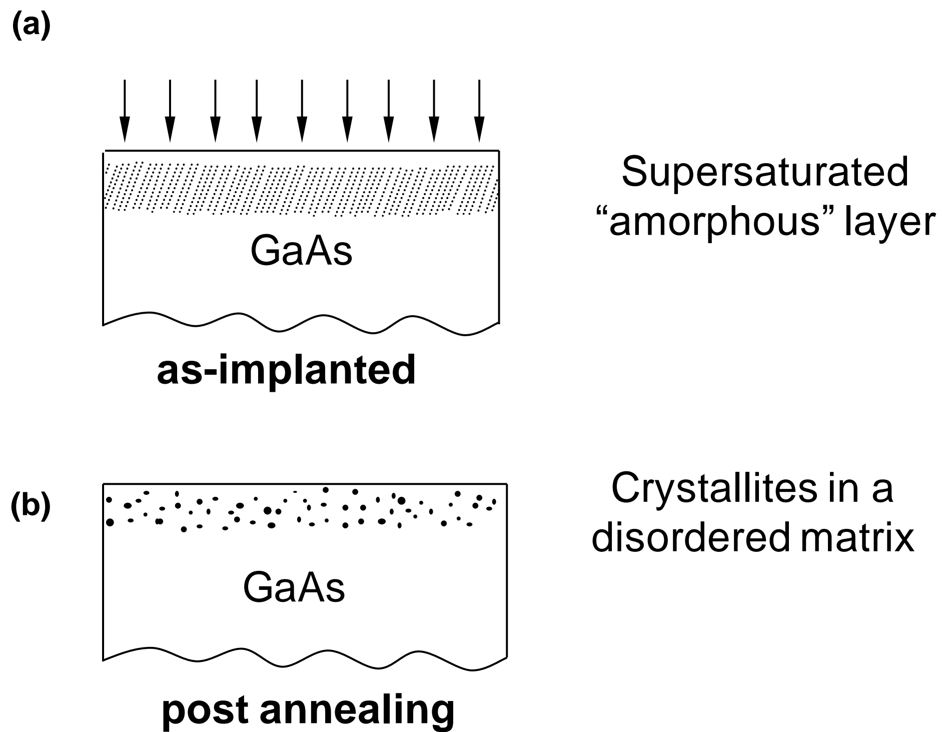

Fig. 1.2 Ion beam synthesis of nitride nanostructures. In (a), a high dose of nitrogen ions (5.0 x 10^{17} cm^{-2} at 100 keV) is implanted into an epitaxial GaAs film to produce a supersaturated “amorphous” layer. In (b), after thermal annealing, nano-scale crystallites form within the disordered matrix.

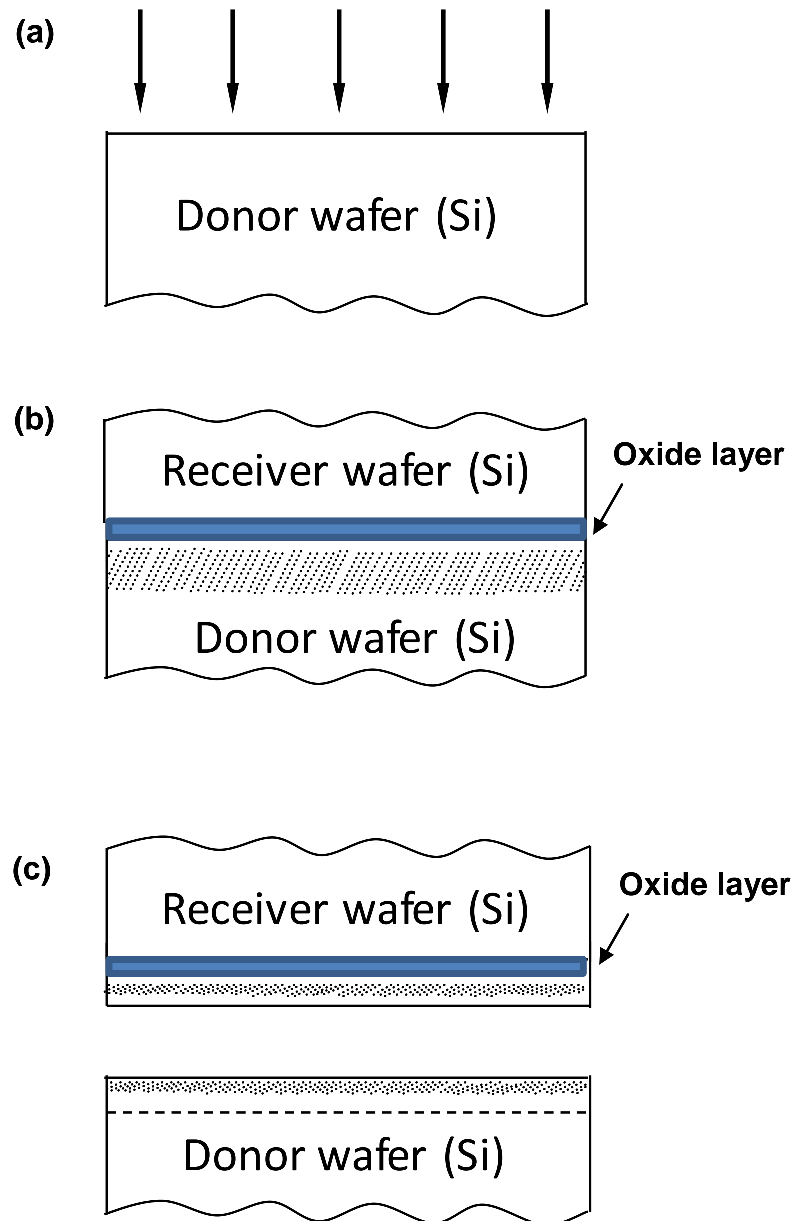

Fig. 1.3 Schematic of the ion-cut process for silicon-on-insulator materials integration. In (a), light ions are implanted into a donor Si wafer, which is subsequently bonded to a receiver Si wafer with an oxide intermediate layer. In (c), thermal annealing leads to the splitting of the donor wafer and transfer to the receiver wafer.

CHAPTER 2

EXPERIMENTAL PROCEDURES

2.1 Overview

This chapter describes the experimental procedures used for the synthesis, bonding, layer transfer, and characterization of the GaAs:N layers studied in this thesis. All GaAs:N layers were synthesized by N-ion implantation into epitaxial GaAs layers. The majority of the epitaxial samples were grown in the Goldman group molecular beam epitaxy (MBE) system and consist of either undoped, Si-doped, or Te-doped GaAs layers on semi-insulating GaAs substrates. For surface-blistering studies, the N-implanted GaAs layers subsequently underwent rapid-thermal-annealing (RTA). The surface morphology was studied via optical microscopy, scanning electron microscopy (SEM), and atomic-force microscopy (AFM). In addition, ion- and damage-depth profiles were obtained by nuclear reaction analysis (NRA) and Rutherford backscattering spectrometry (RBS), respectively. The electrical and thermal properties were studied with resistivity, Hall, and Seebeck coefficient measurements.

For layer transfer, the N-implanted GaAs samples were bonded to a 'receiver' substrate prior to annealing. In all cases, wafer bonding was performed at room temperature with spin-on glass (SOG) films used as an intermediate bonding layer. The structure of both the blistered layers and the transferred layers were studied via transmission electron microscopy (TEM). All procedures were performed by the author except where noted.

2.2 Ion Implantation and Rapid Thermal Annealing

Ion implantation experiments were carried out at the Michigan Ion Beam Laboratory (MIBL) using either a Varian CF3000 200 kV ion implanter or a National Electrostatics Corporation 400 kV ion implanter. In addition, some implantations were performed at Los Alamos National Laboratory by Dr. Yongqiang Wang. The main components of an ion implantation system[1] are shown in Fig. 2.1 and consist of the ion source, an accelerating column, a mass separation system, and a scanning system. The ion source consists of the source material to be implanted and an ionization system. In the case of nitrogen, a plasma is created with high-purity nitrogen gas which is ionized by electrons thermally emitted from tungsten filaments. In the accelerating column, the ions are accelerated by extraction electrodes and formed into a beam. A mass separation magnet creates a magnetostatic field which induces mass- and charge-dependent Lorentz force,[2] steering only the selected ion species toward the target chamber. The beam is then raster scanned using a varying electric

field. Faraday cups placed at the perimeter of the target area, within the scanning path of the ion beam, are used to measure the fluence by creating a current proportional to the number of positive ions delivered.

For all samples discussed in this thesis, implantation was performed into ~1 μm thick GaAs films (undoped, Si-doped, or Te-doped) grown by molecular-beam epitaxy on (001) GaAs. These films were implanted with 100 keV nitrogen ions at a fluence of 5×10^{17} cm^{-2}. To minimize ion channeling, a ~7° ion beam angle of incidence with respect to the sample surface normal was utilized. During implantation, the substrate temperature was maintained at -196 °C or 300 °C, as determined by a J-type thermocouple attached to the back of the sample holder.

Some of the implanted samples were subsequently heated by RTA to induce blister formation or layer transfer. RTA was carried out with a JetFirst 150 halogen lamp rapid thermal processer in the Lurie Nanofabrication facility, in the Electrical Engineering and Computer Science department at UM. Samples were heated on silicon substrates supported by quartz pins, with temperature controlled via feedback with a thermocouple contact to the back of the support wafer, shown schematically in Fig 2.2. Samples were annealed in flowing nitrogen or argon gas at 800, 850, or 900°C for 30 s with measured overshoots of less than 20 °C.

2.3 Scanning Electron Microscopy

Scanning electron microscopy (SEM) was used to examine the surface morphology of unbonded, implanted and/or annealed surfaces. In this imaging mode, a beam of electrons with energy between 5 and 30 keV are scanned across the sample surface. The interaction of an impinging electron with a sample surface can cause several interactions, including elastically-scattered (backscattered) electrons, secondary electrons, Auger electrons, X-ray emission, phonon generation (heat), and Bremsstrahlung radiation.

For this thesis work, all images presented are secondary-electron (SE) images collected in either a FEI Nova Nanolab or FEI Quanta 200 3D scanning electron microscope. SE emission occurs when an incident electron ejects a weakly-bound electron in an atom of the specimen. This ejected electron may eventually escape, with relatively low energy (typically[3] < 50 eV). Thus, this imaging mode is surface-sensitive, as only electrons generated near the surface have sufficient energy to escape. The SE signal is characteristic of the surface topology,[4] as shown schematically in Fig. 2.3. Electrons emitted from surface peaks are more likely to escape than those from surface depressions, giving rise to topological contrast. For all cases of high-vacuum SEM imaging in this thesis, the SE signal was collected by an Everhart-Thornley[5] detector. This detector consists of a scintillator material that produces light, which is collected by a

photomultiplier. This detection scheme results in an amplified electron signal with high gain.[6]

2.3.1 Environmental Scanning Electron Microscopy

Imaging of layer-transfer samples, including SOG-coated and bare ceramic surfaces, was achieved through environmental scanning electron microscopy (ESEM) in low-vacuum mode, using a Quanta 200 3D Dual-beam SEM. For insulating samples, this technique is preferable to imaging in high-vacuum mode, which typically requires the application of a conductive layer to avoid surface charging effects. In this imaging mode, surface charging effects are reduced by introducing water vapor into the sample chamber, as shown in Fig. 2.4. The presence of water vapor increases the chamber pressure (in our case, to ~0.8 Torr) but also acts as a charge-compensating mechanism. The incident electron beam will tend to create a negative charge build-up on an electrically insulating surface. However, these electrons will also ionize the ambient gas. The resulting positive charge will be attracted to the sample surface, canceling the effect of surface charging.[7] The imaging electrons also undergo collision cascades with ionized water vapor, as shown in Fig. 2.4, acting to amplify the secondary-electron signal.

2.3.2 X-Ray Energy Dispersive Spectroscopy

The surface chemical composition of blistered samples was examined qualitatively by X-Ray Energy Dispersive Spectroscopy (XEDS), in a FEI Quanta 200 3D dual-beam SEM. During electron beam irradiation, incident electrons may eject inner-shell electrons from the sample. An outer-shell electron may subsequently relax to the lower-energy state and emit an X-ray with energy equal to this difference in electronic energy levels. Thus, the emitted X-ray is characteristic of the unique atomic structure of excited atom, and the number of X-rays emitted in a given scan time related to the concentration of that element in the sample. In this case, a Si(Li) diode under reverse bias was used to detect the energies of emitted X-rays.

2.4 Atomic Force Micrsocopy

Atomic force microscopy was used to obtain quantitative information about the morphology of the GaAs:N surfaces. All experiments were performed with a Digital Instruments Nanoscope IIIA atomic force microscope, with the aid of Brian Dick and Natalie Estrada. In this technique, images are created by scanning a sharp tip across the sample surface, and the z-motion (height) of the tip is correlated with the height profile of the sample. For this thesis work, tapping-

mode[8] AFM was employed, as shown schematically in Fig. 2.5. In tapping mode, the tip is oscillated in z so that only intermittent contact is made. This reduces the effect of friction and lateral forces and mitigates tip-induced damage to the surface that may occur in contact mode. A laser is directed at the back of the cantilever and its reflected signal is collected by a photodiode. This signal is used to monitor the sample position in conjunction with a computerized feedback system, which controls piezoelectric actuators that drive the tip. The cantilever is excited with a constant force, near its resonance frequency. The amplitude of the oscillation decreases as the tip interacts with surface features. This feedback is used to adjust the tip's position in z to keep the oscillation amplitude constant, thus giving height information as a function of position.

2.5 Ion Beam Analysis

The role of N-implantation damage and N diffusivity on the blister formation process in GaAs:N were examined using ion beam analysis techniques. Rutherford backscattering spectrometry was used to determine lattice damage depth profiles, and nuclear reaction analysis was used to determine the retained N dose and qualitative N depth profiles in GaAs:N films. All experiments were performed at the Michigan Ion Beam Laboratory (MIBL) with the aid of Dr. Fabian Naab, using a General Ionex 1.7 MV Tandetron accelerator.

2.5.1 Channeling-Rutherford Backscattering Spectrometry

Channeling-Rutherford backscattering spectrometry (RBS) was utilized to determine the depth-dependence of lattice disorder in implanted samples before and after annealing. In this technique, a collimated beam of charged particles (in our case, 2 MeV He^{++}, i.e. α-particles) is directed at the sample surface. Backscattered particles were detected by a solid-state particle detector subtending a solid angle $\Omega \approx 5$ mili-steradians, as shown in Fig. 2.6. The total number of detected ions, or yield, was measured by a charge integrator connected to a 300 μm-thick B-implanted silicon charged-particle detector (ULTRA series, Ortec[9]). A Faraday cup was used near the sample to generate an electric field, preventing spurious charge counts from sputtered electrons at the sample surface.

In the channeling condition, the sample is aligned so that the incident beam is parallel to a channel in the crystal, as shown in Fig. 2.7(a). The particle is steered through a row of atoms in a crystalline lattice by undergoing only small-angle scattering within the channel. Rutherford scattering occurs when the incident positively-charged particle undergoes large-angle scattering from Coulomb repulsion from atomic nuclei of the sample atoms. Thus, some fraction of the particles will be dechanneled due to lattice defects, impurities, strain fields, and thermal vibrations.[10] An example of a particle/lattice-defect interaction that results in dechanneling[11] is shown schematically in Fig. 2.7(b) for point defects.

The energy of the backscattered particle is characteristic of the target atom that it collides with. Assuming an elastic collision, the ratio of incoming and outgoing projectile energies is dependent only on the masses of the particle and target atom and the angle of collision. This ratio is defined as the kinematic factor *K*:

$$K = \frac{E_1}{E_0} = \left[\frac{\left(M_2^2 - M_1^2 (\sin\theta)^2\right)^{1/2} + M_1 \cos\theta}{M_1 + M_2}\right] \quad (2.1)$$

where M_1 and M_2 are the projectile and target atom masses, E_1 and E_0 are outgoing and incoming projectile energies, and θ is the scattering angle. Since the atomic weights of Ga and As are similar (Z = 31 and 33, respectively), the energy difference of α-particles backscattered by Ga versus As will be small. Thus, the profile represents an average damage depth profile from backscattering from either Ga or As. Similarly, RBS does not provide information on N concentration or depth profile due to its relatively small mass; instead, nuclear reaction analysis is utilized for those purposes, as described below.

2.5.2 Nuclear Reaction Analysis

The total retained N dose and depth-dependent N concentration were determined with nuclear reaction analysis (NRA). In this technique, an energetic beam of particles is directed at the sample surface. If the particles have

sufficient energy to penetrate the Coulomb barrier of the target atom, a nuclear reaction may occur, resulting in an excited compound nucleus as shown schematically in Fig. 2.8. Upon decaying, the compound nucleus will produce a product nucleus and reaction product (for example, γ-rays, protons, or α-particles) with energy *E*. The following reaction:

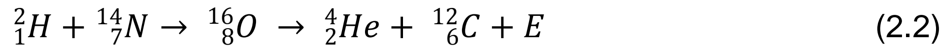

$$^{2}_{1}H + ^{14}_{7}N \rightarrow ^{16}_{8}O \rightarrow ^{4}_{2}He + ^{12}_{6}C + E \quad (2.2)$$

was utilized to examine N concentration profiles. In this case, a deuteron ($^{2}_{1}H$ or d) collides with a nitrogen atom ($^{14}_{7}N$) to create an excited oxygen nucleus ($^{16}_{8}O$), which then decays into carbon ($^{12}_{6}C$) and an energetic alpha particle ($^{4}_{2}He$ or α). This reaction may be denoted in shorthand as $^{14}N(d,\alpha)^{12}C$. In particular, the $^{14}N(d,\alpha_1)^{12}C$ and $^{14}N(d,\alpha_0)^{12}C$ reactions are convenient because their by-product energies are relatively free of background and isolated from other reaction signals, as shown in the NRA spectrum of an N-implanted GaAs sample in Fig. 2.9.

The observed yield from the $^{14}N(d,\alpha_1)^{12}C$ or $^{14}N(d,\alpha_0)^{12}C$ reaction signal can be correlated to the retained N concentration using the following relationship:[12]

$$Y = N_s \sigma(\theta) Q \Omega \quad (2.3)$$

where *Y* is the integrated counts under the α-particle peak, *Q* is the number of incident particles measured by a charge integrator, Ω is the solid angle of the detector, and σ(θ) is the scattering cross section for a given detection angle θ.

This cross-section is a measure of the probability of the scattering event, and has been measured at at 150º by several groups,[13,14,15] most recently by Pellegrino *et al.*[16] Figure 2.10 presents the result from Pellegrino *et al.* for this particular nuclear reaction; their results are used for all data analysis in this thesis. As shown in Fig. 2.10, σ(E) is relatively constant between ~1 and ~1.4 MeV, making this reaction attractive for depth profiling, as the reaction spectrum will be directly proportional to the target atom concentration, within the energy interval of detection.[17]

The experimental setup for NRA of GaAs:N films is shown in Fig. 2.11. In our case, a collimated beam of 1.2 MeV deuterons was directed at the sample surface, and the α-particle products measured by a particle detector using the same charge integration scheme described in the previous Section 2.5.1. The geometry of the setup may be described by two angles: the incidence angle α between the sample normal and beam line, and the scattering angle θ between the beam and detector. The differences in experimental setup for retained N dose determination versus N depth profiling are as follows. To determine the total retained dose, the angle α was set near the channeling condition to maximize the penetration depth, and a ~20 μm thick Mylar foil was placed in front of the detector to filter out low-energy signals. This scheme reduces signal pile-up, which occurs when two separate low-energy signals are collected in a short time interval and counted as one signal. This spurious signal has an apparent energy equal to the sum of two low-energy signals. However, the presence of a

foil in front of the detector will also lead to energy losses in the incident particles ("energy straggling"), which is a concern for depth profiling, as described below.

For depth profiling, the sample was tilted to $\alpha \approx 50°$ to increase the path length of outgoing particles. This angle was observed to give the largest energy interval for a given reaction signal, thus maximizing the depth resolution. In this case, no foil is placed in front of the detector in order to reduce energy straggling. In all cases, the scattering angle was set to $\theta = 150^{o}$ as described above. To minimize geometrical straggling, a 2 mm aperture was placed in front of the detector and the sample-detector distance set at 8.5 cm.

2.6 Wafer Bonding

GaAs(:N) samples were bonded to various semiconductor, ceramic, and glass substrates either as a first step in the layer transfer process, or to measure the adhesion properties of the bonding layer using a "blade test," as described in Section 5.3. In all cases, a spin-on glass (SOG) was used as an intermediate layer. These materials consist of SiO_2, polymer(s), and/or dopants suspended in solvent. The solution is deposited and spin-coated to achieve a planar layer with a well-defined thickness, and subsequently cured to drive off the solvent. Typically, SOGs are deposited as dielectric or passivating layers in devices, including metal-oxide-semiconductor[18] (MOS) or double heterojunction bipolar transistor[19] (DHBT) structures.

More recently, SOGs have also been utilized as a bonding agent for materials integration. Examples of SOG-bonded structures include GaInAs-based vertical-cavity surface-emitting lasers on silicon substrates[20] and layer transfer of GaAs to Si by ion-cut.[21,22] However, unlike these examples for which processing temperatures are relatively low (< 400 °C), ion-cut-synthesis requires RTA at > 750 °C. The relatively high temperature requirement creates challenges for the integration of dissimilar materials due to thermal-expansion mismatch stresses. For this reason, several SOG chemistries, as shown in Fig. 2.12, were explored for high-temperature-stable bonding, including two siloxane-based SOGs supplied by Filmtronics:[23] methylsiloxane (Filmtronics 500F), and methylsilsesquioxane (Filmtronics FG65), as well as a methyltrimethoxysilane - 1,2-bis(triethoxysilyl)ethane (MTMS-BTSE) co-polymer-based SOG provided by Hyun-Wook Ro and Chris Soles at NIST.

Fig. 2.13 shows the typical process steps in a bonding experiment. In all cases the first step was a solvent clean of the wafer surfaces, followed by deposition of ~1 mL of SOG by a dropper to the surface of one wafer. Next, spin-coating was performed in a Laurell[24] WS-400-6NPP-LITE spin processor. The two wafers were subsequently joined at room temperature to create the initial bond, followed by thermal annealing. In most cases, bonding pressure was applied using tweezers for several seconds. If the resulting bonded structure was annealed to induce both nanostructure formation and splitting, then the final step was instead RTA (using the procedure described in Section 2.2). The

details of the processing parameters for all experiments are included in Appendix B.

2.7 Transmission Electron Microscopy

To determine the structure of blistered and transferred layers, transmission electron microscopy (TEM) was carried out in a JEOL 3011 transmission electron microscope operating at 300 kV. All TEM imaging was performed by the author with the assistance of Adam Wood. In all cases, images were collected with a CCD camera controlled with Gatan Digital Micrograph image capture software. In some cases, a two-beam condition was used to image the sample, as shown schematically in Fig. 2.14. In this condition, an objective aperture is used to select only the transmitted (000) beam for bright-field imaging, or diffracted beam(s) for dark-field imaging.[25] Cross-sectional TEM (XTEM) samples were prepared either by conventional mechanical polishing techniques (for blistered layers), or by a FIB lift-out technique (for transferred layers); the latter is described in Appendix C. In all cases, due to the relatively high damage incurred by FIB, the {111} diffracted signal is used for dark-field TEM imaging of transferred layers.

For the blistered samples prepared by mechanical polishing, ~2x3 mm GaAs:N pieces were cleaved and bonded face-to-face with either GaAs or Si using a silver epoxy (Epoxy Technology H22). The bonded samples were placed

on a hotplate and cured at ~120 °C for 20 minutes. The bonded pair was then mechanically polished using a tripod polisher to create a “wedge-shaped” sample with the thinner part of the wedge (~10 μm thick) further ion-milled for TEM imaging. To minimize polishing-induced damage, a sequence of decreasing particle sizes were used, starting with SiC-particle paper (in a sequence of 600, 800, 1000, and 1200 grit papers, corresponding to 16, 12, 10, and 8 μm particle sizes) followed by diamond polishing papers (1500 and 60,000 grit, or 3.0 and 0.5 μm particle sizes). One side was polished, then glued to a molybdenum TEM slot grid with silver epoxy, and the remaining side was polished at a ~5° angle with the same polishing grit sequence. Final polishing was performed by Ar ion milling at 77 K, with a Gatan PIPS-691 at low angles (2-4º) and currents (<10 μA), until perforation at the interface.

2.8 Nanoindentation

Nanoindentation was used to probe the mechanical properties of as-implanted and implanted-plus-annealed GaAs:N layers. All experiments were performed with a Nanoinstruments Nanoindenter, using a Berkovitch diamond indenter tip.[26] Experiments were performed in constant-displacement mode, with maximum tip displacements of 20 nm. This indentation depth, which is less than 10% of the implanted film thickness, was chosen in order to ensure the characterization of the film properties without influence of the substrate

properties.[27] Due to the limits in spatial resolution and lateral positioning of the sample stage, it was not possible to collect indentation data corresponding to individual surface blisters.

2.9 Characterization of Electrical and Thermal Properties

Hall, resitivity, and Seebeck measurements were performed to investigate the electrical and thermal transport properties of as-grown, as-implanted, and implanted-plus-annealed films.

2.9.1 Hall and Resistivity Measurements

The electrical transport properties of GaAs:N films were determined by Hall and resistivity measurements. The sample geometry (Van der Pauw configuration) is shown schematically in Fig. 2.15; typically, a symmetric sample ~5 mm square was used, with ~0.5 mm diameter contacts. The contacts were fabricated by depositing In at the edges of the square sample, followed by RTA at ~400 ^{0}C for 2 min. Au wires 25 μm in diameter were bonded to the In contacts and connected to a component carrier. I-V measurements were performed with a Hewlett Packard 4156B semiconductor parameter analyzer in order to determine the Ohmic nature of each contact. Typical contact resistances

measured were $O(10\ \Omega)$ for as-grown samples, $O(10\ \mathrm{M}\Omega)$ for N-implanted samples, and $O(1\ \mathrm{k}\Omega)$ for N-implanted-plus-annealed samples. For Hall and resistivity measurements, a Keithley 224 current source was used to send a DC current ranging from 10 nA to 1 mA between two contacts. In the absence of an applied magnetic field, the voltage difference is measured parallel to the direction of current flow. Next, Hall measurements were performed with an electrical current flowing in the presence of a magnetic field of ~0.1 Tesla. In this case, carriers are subjected to the Lorentz force and will drift in a direction perpendicular to both the direction of the current flow and the magnetic field, resulting in a potential difference in this third direction, termed the "Hall voltage." From these measurements, the resistivity and free carrier concentration were determined using the procedures in ASTM standard F76.[28] The resistivity values reported in this thesis represent an average over the full thickness of the n-doped MBE-grown layers (1 μm) and are corrected for depletion widths at the free surface and at the interface between the MBE-grown film and the semi-insulating substrate, following the procedures in Ref. 29.

2.9.2 Seebeck Measurements

The thermopower or Seebeck coefficient, *S,* of GaAs:N films was measured using a micro-thermocouple station in the Pipe Lab in Mechanical Engineering. This setup is shown schematically in Fig. 2.16. The Seebeck

coefficient is a measure of the voltage difference which develops in response to an applied temperature gradient. Thermal drift causes charge carriers to migrate from the hot to the cold side, and this charge separation, in turn, results in an electric field. The current density *J* (for electrons as the dominant charge carrier) due to both a thermal gradient, *dT/dx,* and a potential gradient, *dΦ/dx,* may be described as:[30]

$$J = L_{11}\left(-\frac{d\Phi}{dx}\right) + L_{12}\left(-\frac{dT}{dx}\right) \tag{2.4}$$

where L_{11} is the electrical conductivity:

$$L_{11} = -\frac{e^2}{3}\int v^2 \tau \frac{\partial f_0}{\partial E} D(E)dE \tag{2.5}$$

and L_{12} is a coupling coefficient between the temperature gradient and electrical current given by:

$$L_{12} = -\frac{e}{3T}\int v^2 \tau\left(E - E_f\right)\frac{\partial f_0}{\partial E} D(E)dE \tag{2.6}$$

where *e* is the elementary charge, v is the carrier drift velocity, τ is the carrier relaxation time, f_0 is the equilibrium distribution of carriers, *D(E)* is the density of states, and $E_{(f)}$ is the (Fermi) energy. At equilibrium, open-circuit conditions, equation 2.4 leads to:

$$\left(\frac{d\Phi}{dx}\right) = -\frac{L_{12}}{L_{11}}\left(\frac{dT}{dx}\right) = -S\left(\frac{dT}{dx}\right) \tag{2.7}$$

and thus the Seebeck coefficient is defined as the ratio of L_{12} to L_{11}. All of the material in this study is doped n-type (Si-doped or Te-doped). Since the majority

charge carriers are electrons for the material studied in this thesis, the sign of the resultant electric field will be opposite to that of the temperature gradient, resulting in a negative Seebeck coefficient.

2.10 Wafer Curvature Measurements and Estimation of Implantation-induced Stress

To determine the implantation-induced stresses in N-implanted GaAs, wafer curvature measurements were performed with a Dektak3 profilometer in the Michigan Ion Beam Lab in the Nuclear Engineering and Radiological Sciences Department at UM. For these measurements, a diamond-tipped stylus was moved across the sample surface, and the height *y* measured as a function of lateral distance *x*. To determine the radius of curvature, this profile is fit to a fifth-order polynomial according to the method of least-squares.[31] The differential is then used to determine the radius of curvature *R*:

$$R(x) = \frac{(1+y'^2)^{3/2}}{y''} \tag{2.8}$$

where ‘ denotes differentiation with respect to *x*. In all cases, the curvature was estimated before and after implantation in order to determine the stress in the as-implanted film. These curvature measurements are provided in Section 4.5.

2.11 References

[1] M. Nastasi, J. W. Mayer, and J. K. Hirvonen, eds. *Ion-solid Interactions: Fundamentals and Applications* (Cambridge University Press, Cambridge, UK, 1996), Chapter 2.

[2] E. Rimini, *Ion Implantation: Basics to Device Fabrication* (Springer-Verlag, New York, 1995), Chapter 2.

[3] D. Stokes, *Principles and Practice of Variable Pressure/Environmental Scanning Electron Microscopy* (Wiley, West Sussex, 2008), p. 41.

[4] W. Zhou, R. P. Apkarian, Z. L. Wang, and D. Joy, in *Scanning Microscopy for Nanotechnology: Techniques and Applications* (Springer, New York, 2006), p. 6.

[5] T. E. Everhart and R. F. M. Thornley, J. Sci. Instrum. **37**, 246 (1960).

[6] J. Goldstein, D. Newbury, D. Joy, C. Lyman, P. Echlin, E. Lifshin, L. Sawyer, and J. Michael, *Scanning Electron Microscopy and X-Ray Microanalysis,* 3rd. Ed. (Springer, New York, 2003), p. 129.

[7] A. M. Donald, Nat. Mater. **2**, 511 (2003).

[8] A. Schirmeisen, B. Anczykowski, and H. Fuchs, in *Nanotribology and Nanomechanics: An Introduction* (Springer-Verlag, Berlin, 2008), p. 247.

[9] AMETEK Advanced Measurement Technology, Oak Ridge, TN; http://www.ortec-online.com

[10] D. S. Gemmell, Rev. Mod. Phys. **46**, 129 (1974).

[11] J. R. Tesmer and M. Nastasi, *Handbook of Modern Ion Beam Materials Analysis* (Materials Research Society, Pittsburgh, 1995).

[12] T. L. Alford, L. C. Feldman, and J. W. Mayer, *Fundamentals of Nanoscale Film Analysis* (Springer, New York, 2007), p.17.

[13] G. Amsel, J.P. Nadai, E. d'Artemar, D. David, E. Girard, and J. Moulin, Nucl. Instrum. Methods **92**, 481 (1971).

[14] J. A. Davies, T. E. Jackman, H. Plattner, and I. Bubb, Nucl. Instrum. Methods **218**, 141(1983).

[15] S. R. Walker, J. A. Davies, P. Mascher, S. G. Wallace, W. N. Lennard, G. R. Massoumi, R. G. Elliman, T. R. Ophel, H. Timmers, Nucl. Instrum. Methods Phys. Res. B **170**, 461 (2000).

[16] S. Pellegrino, L. Beck, and P. Trouslard, Nucl. Instum. Methods Phys. Res. B **219-220**, 140 (2004).

[17] H. Bubert and H. Jenett, *Surface and Thin Film Analysis: Principles, Instrumentation, and Applications* (Wiley, Weinheim, 2002).

[18] S. Ito, Y. Homma, E. Sasaki, S. Uchimura, and H. Morishima, J. Electrochem. Soc. **137**, 1212 (1990).

[19] R. F. Kopf, R. A. Hamm, R. W. Ryan, J. Burm, A. Tate, Y.-K. Chen, G. Georgiou, D. V. Lang, and F. Ren, J. Electron. Mater. **27**, 954 (1998).

[20] H. C. Lin, K. L. Chang, G. W. Pickrell, K. C. Hsieh, and K. Y. Cheng, J. Vac. Sci. Technol B **20**, 752 (2002).

[21] E. Jalaguier, B. Aspar, S. Pocas, J. F. Michaud, M. Zussy, A. M. Papon, and M. Bruel, Electron. Lett. **34**, 408 (1998).

[22] I. Radu, I. Szafraniak, R. Scholz, M. Alexe, and U. Gösele, Appl. Phys. Lett. **82**, 2413 (2003).

[23] Filmtronics Corp., http://www.filmtronics.com

[24] Laurell Technologies Corporation, North Wales, PA; http://www.laurell.com

[25] D. B. Williams and C. B. Carter, *Transmission Electron Microscopy* (Plenum, New York, 1996), Chapter 2.

[26] G. Stachowiak and A. W. Batchelor, *Experimental Methods in Tribology*, (Elsevier, Amsterdam, 2004), p. 138.

[27] T. Y. Tsui and G. M. Pharr, J. Mater. Res. **14**, 292 (1999).

[28] ASTM Standard F76, "Standard Test Methods for Measuring Resistivity and Hall Coefficient and Determining Hall Mobility in Single-Crystal Semiconductors," ASTM International, West Conshohocken, PA, DOI: 10.1520/F0076-08.

[29] A. Chandra, C. E. C. Wood, D. W. Woodard, and L. F. Eastman, Solid-State Electron. **22**, 645 (1979).

[30] G. Chen, *Nanoscale Energy Transport and Conversion,* (Oxford University Press, New York, 2005), p. 254.

[31] M. Zecchino and T. Cunningham, Veeco Application Note: “Thin Film Stress Measurements Using Dektak Stylus Profilers,” 2004, http://www.veeco.com/pdfs/appnotes/AN516_Dektak_Stress_Measure_261.pdf

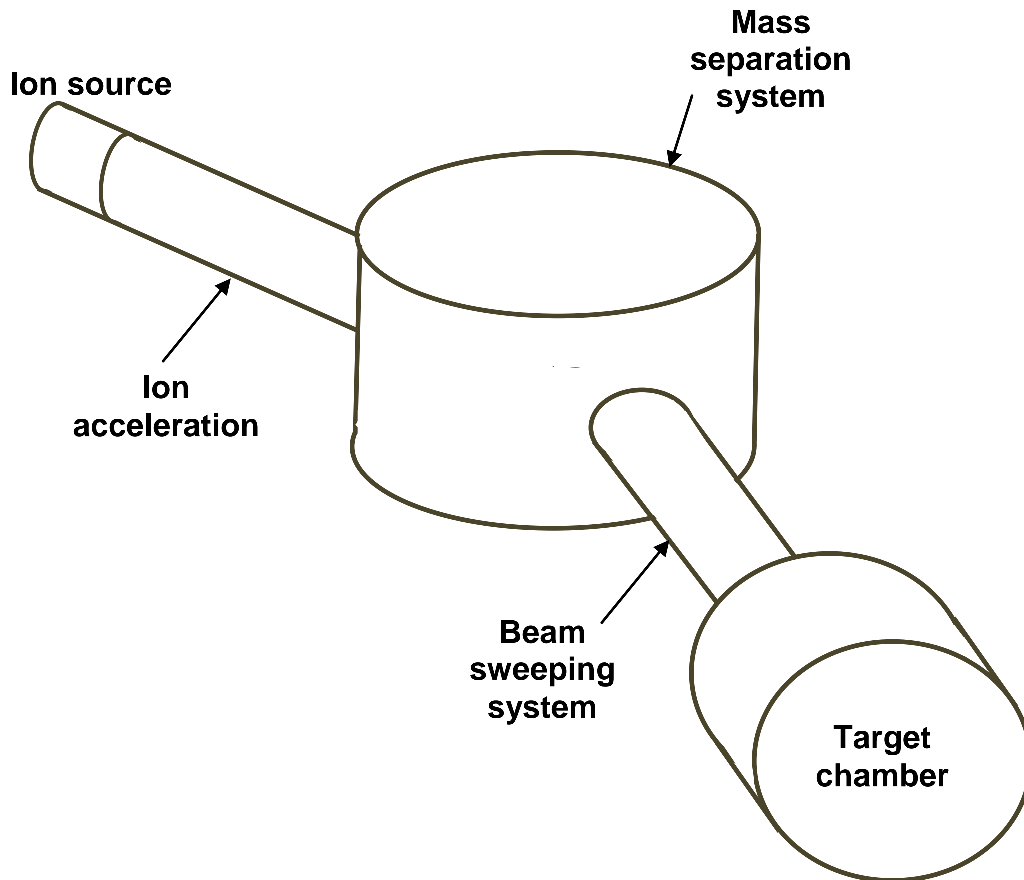

Fig. 2.1 Schematic of an ion implanter, adapted from Ref. 1. The system consists of an ion source, and accelerating column containing extraction electrodes. A magnetic mass separation system is used to separate the ion to be implanted from other charged particles and contaminants. Finally, electrostatic lenses are used to focus and direct the beam towards the target chamber.

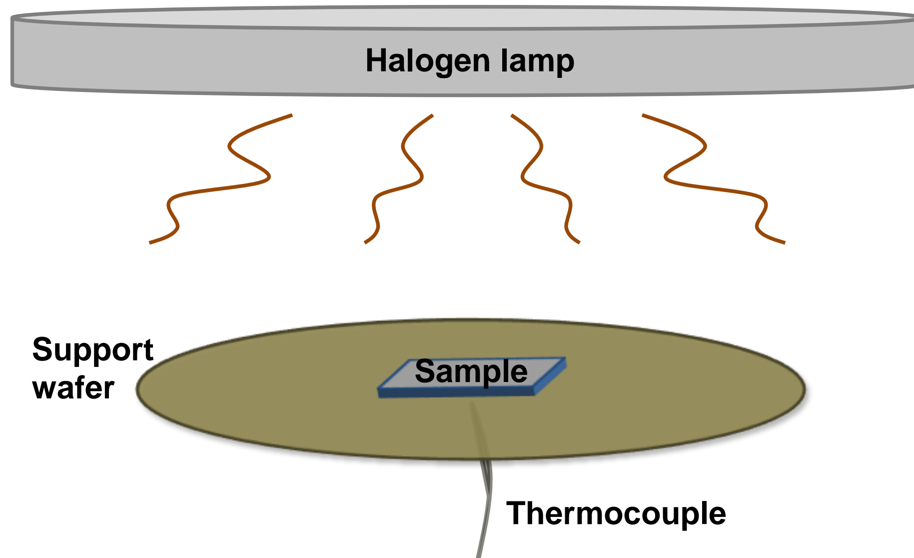

Fig. 2.2 Diagram of the rapid thermal annealing setup. The sample sits on a silicon wafer with a thermocouple contact on the underside. The chamber is purged with flowing nitrogen or argon gas and the sample is heated by a halogen lamp housed inside a quartz window.

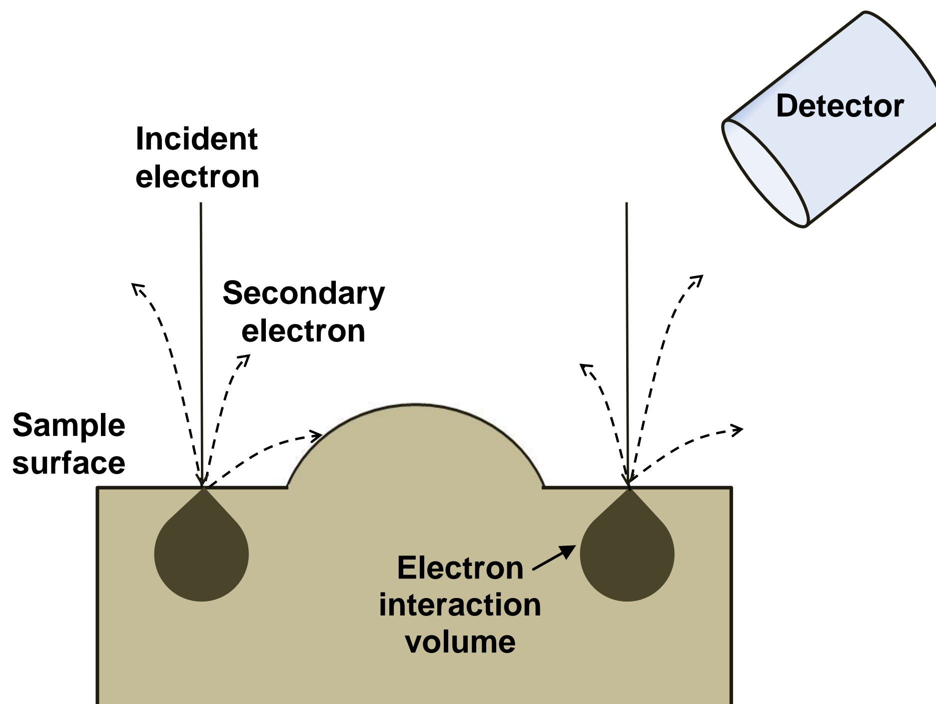

Fig. 2.3 Schematic of electron emission near a sample surface feature, illustrating the origin of image contrast due to surface topography. The incident (scanning) electron paths are represented by solid lines and the emitted electrons by dashed lines. Electrons that are emitted in depressions in the sample surface may be blocked by higher surface features, creating a shadowing effect. Adapted from Ref. 4.

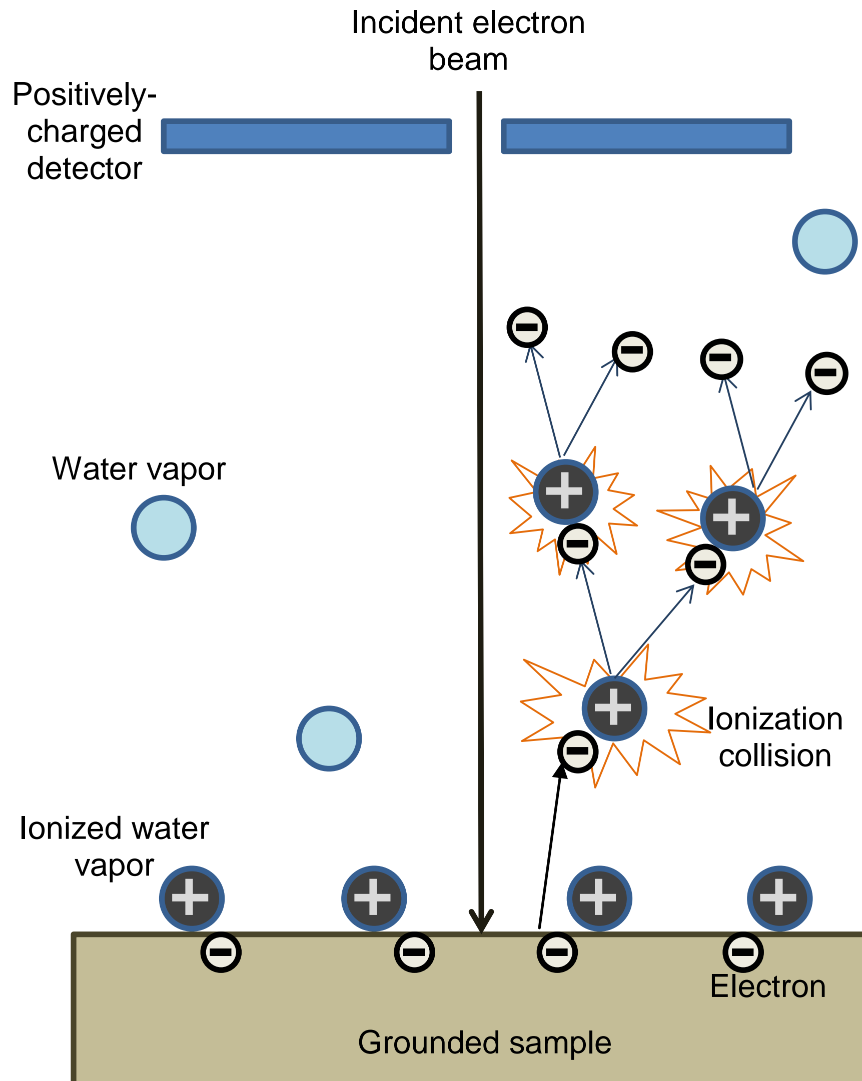

Fig. 2.4 Schematic of electron-beam imaging of an electrically insulating sample in low-vacuum SEM. The imaging electrons collide with gaseous atoms (e.g., water vapor) introduced into the chamber, to generate additional electrons through ionization cascades. The electrons resulting from these cascades are collected by the positively biased detector. The corresponding positive ions drift to the sample, counteracting the negative charge build-up on the insulating surface. Adapted from Ref. 7.

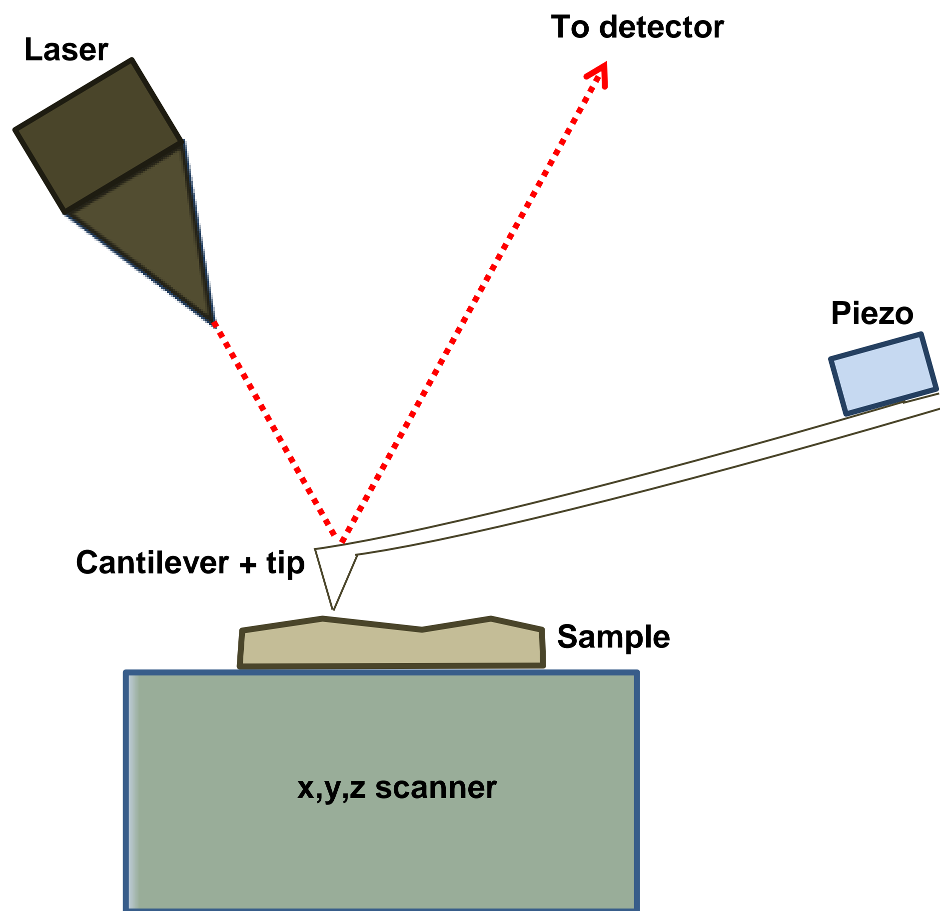

Fig. 2.5 Components of an atomic-force microscope operating in tapping mode. Adapted from Ref. 8.

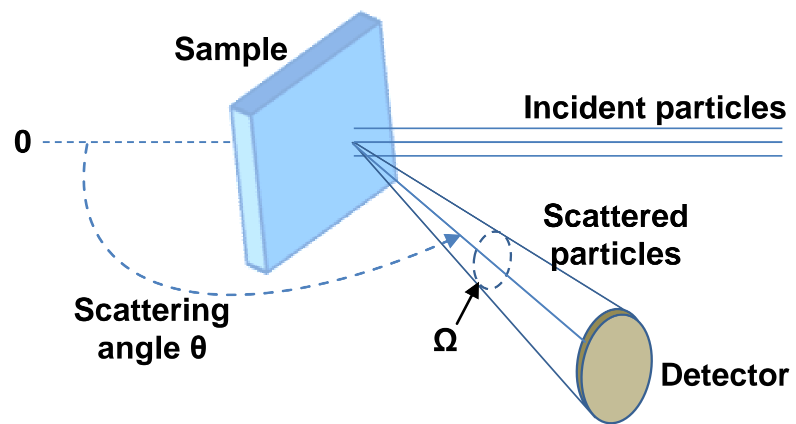

Fig. 2.6 Geometry of a backscattering experiment, illustrating the collection of backscattered particles in a solid angle Ω. Adapted from Ref.12.

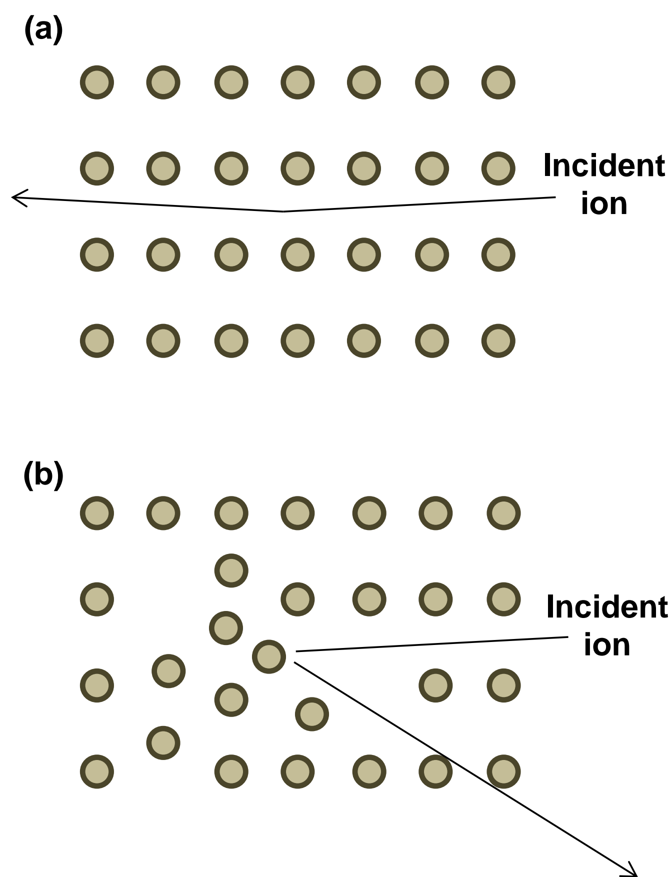

Fig. 2.7 Channeling in (a) a perfect crystal, for which the incident ion undergoes only small-angle scattering within the channel. Dechanneling may occur when the incident ion interacts with lattice defects, as shown in (b). Adapted from Ref.11.

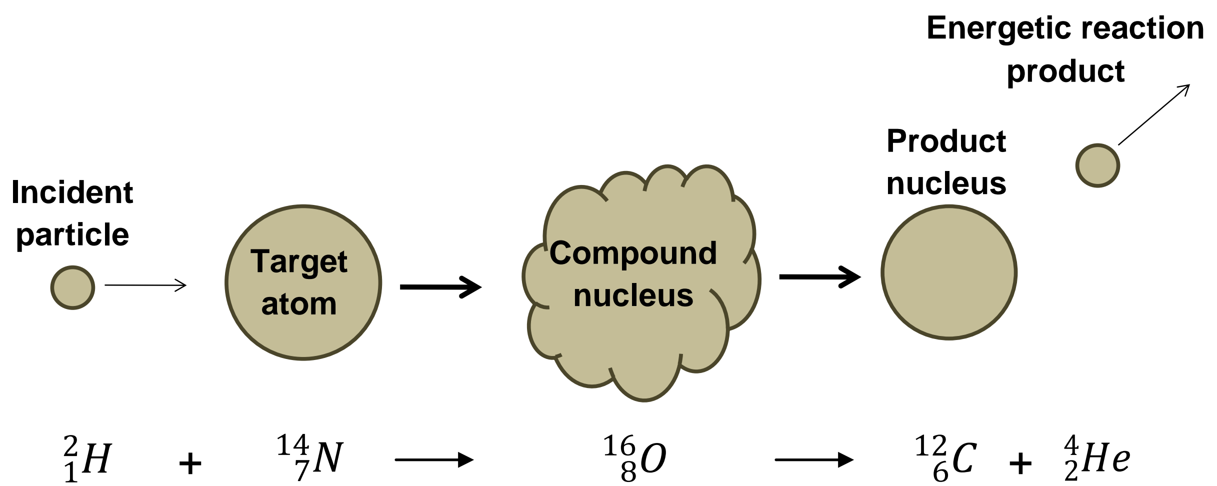

Fig. 2.8 Example of a nuclear reaction, illustrating the formation of a compound nucleus, which decays into a product nucleus and reaction product. The particles corresponding to the $^{14}N(d,\alpha)^{12}C$ reaction are labeled.

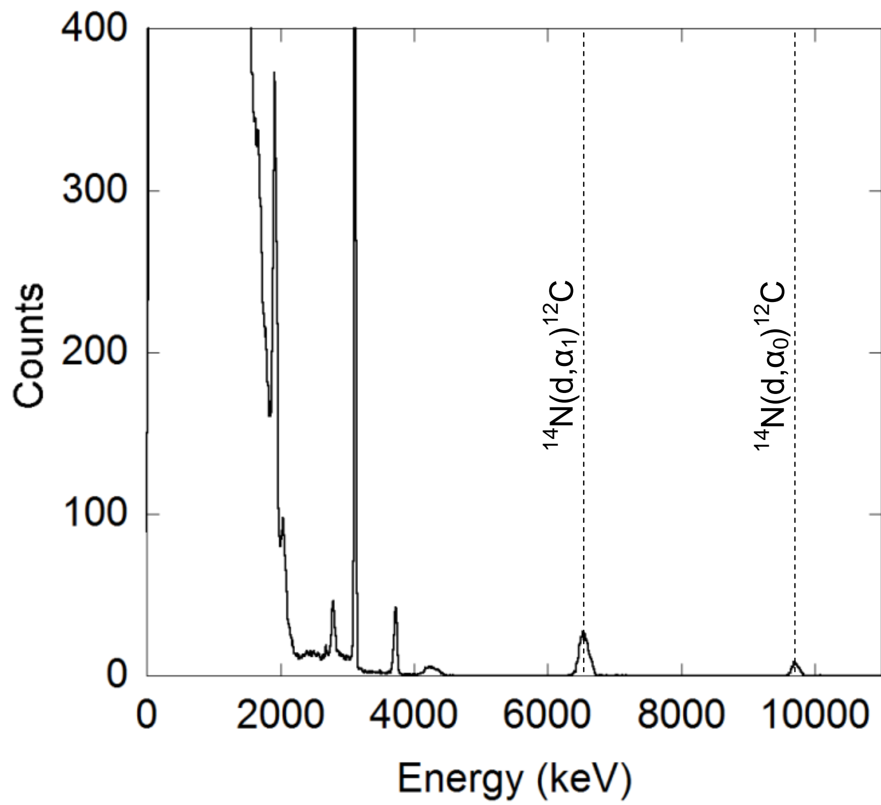

Fig. 2.9 NRA spectrum from N-implanted GaAs. The energies of the α_1 and α_0 reaction products are highlighted by dashed lines.

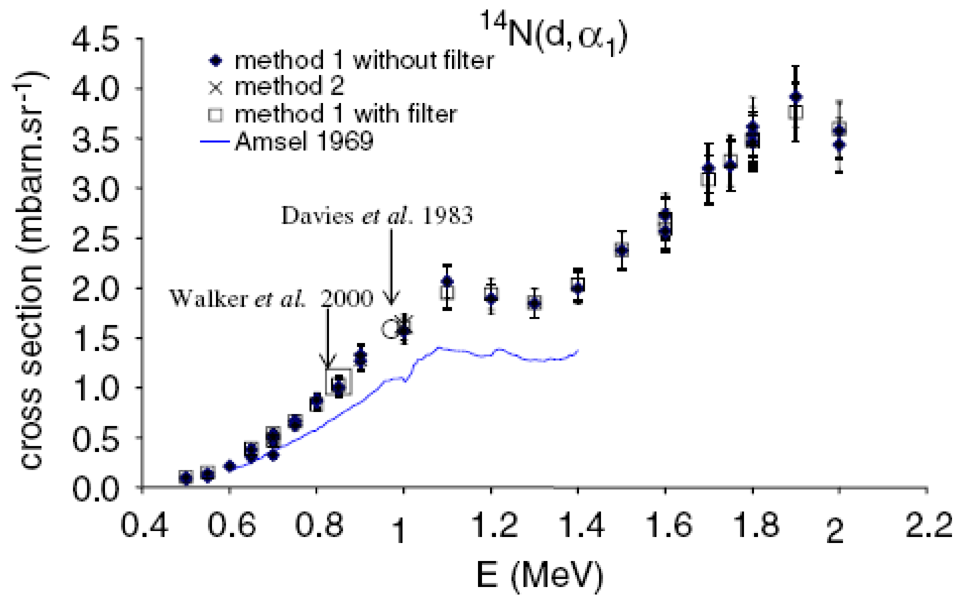

Fig. 2.10 $^{14}N(d,\alpha_1)^{12}C$ reaction cross-section as a function of energy. The relatively constant cross-section of the reaction between ~1.0 and ~1.3 MeV makes it convenient for depth-profiling measurements. Reprinted from Nuclear Instruments and Methods in Physics Research B, Vol. 219-220, S. Pellegrino, L. Beck, and Ph. Trouslard, "Differential cross-sections for nuclear reactions $^{14}N(d,p_5)^{15}N$, $^{14}N(d,p_0)^{15}N$, $^{14}N(d,\alpha_0)^{12}C$ and $^{14}N(d,\alpha_1)^{12}C$," pp. 140-144, Copyright 2004, with permission from Elsevier.

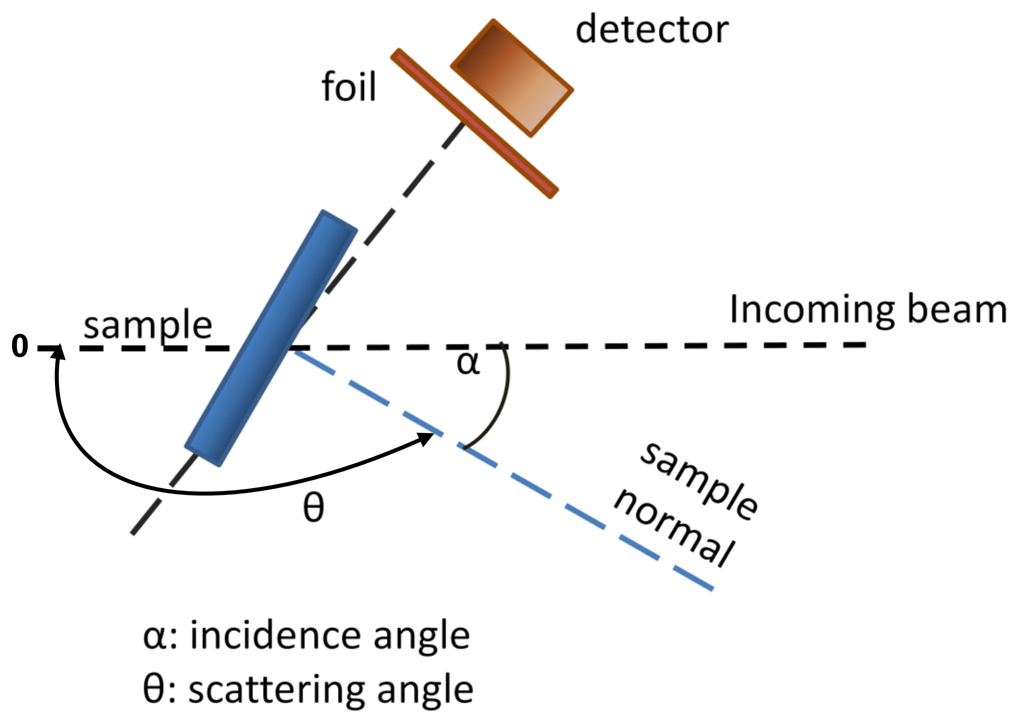

Fig.2.11 Experimental setup for NRA. For retained dose measurements, a foil is placed in front of the detector and the sample tilted to a low incidence angle (channeling condition) to maximize penetration depth. For depth profiling, the sample is tilted to a non-channeling condition and no foil is used, to minimize energy straggling.

siloxane

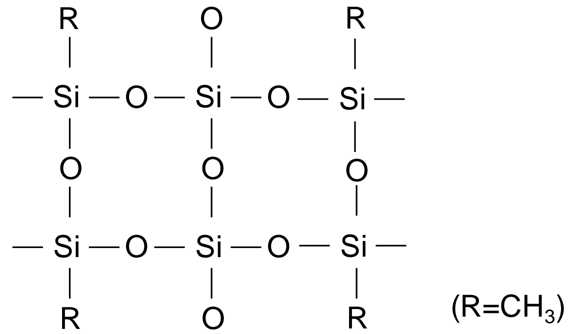

methylsilsesquioxane

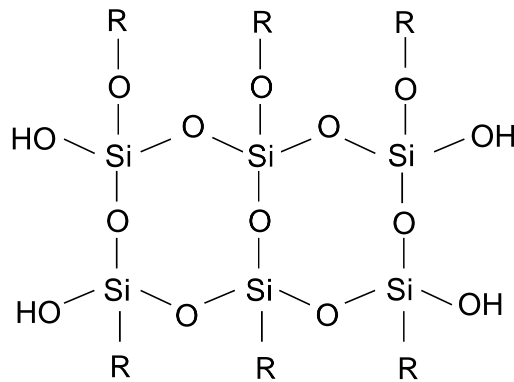

MTMS-BTSE copolymer (methyltrichlorisilane or methyltrimethoxysilane) and (1,2-bis(triethoxysilyl)ethane)

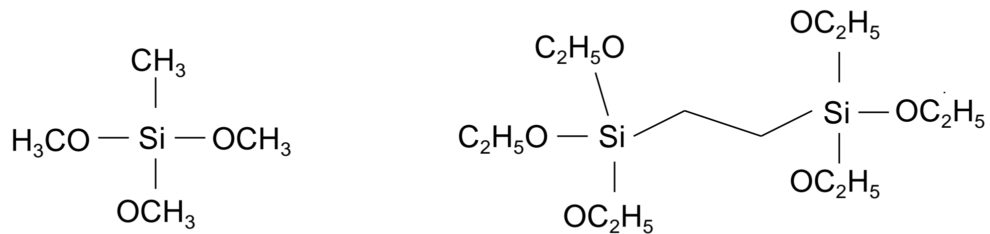

Fig. 2.12 Spin-on glass (SOG) chemistries used in GaAs bonding.

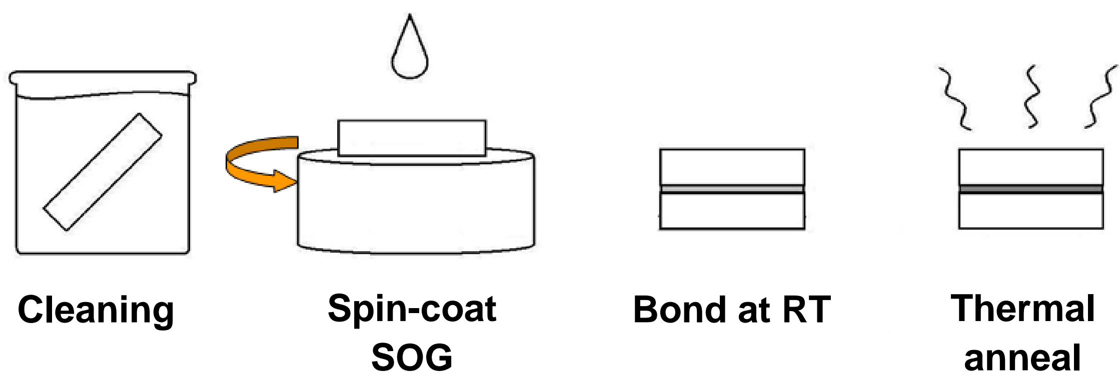

Fig. 2.13 SOG-mediated bonding procedure for GaAs(:N) materials integration.

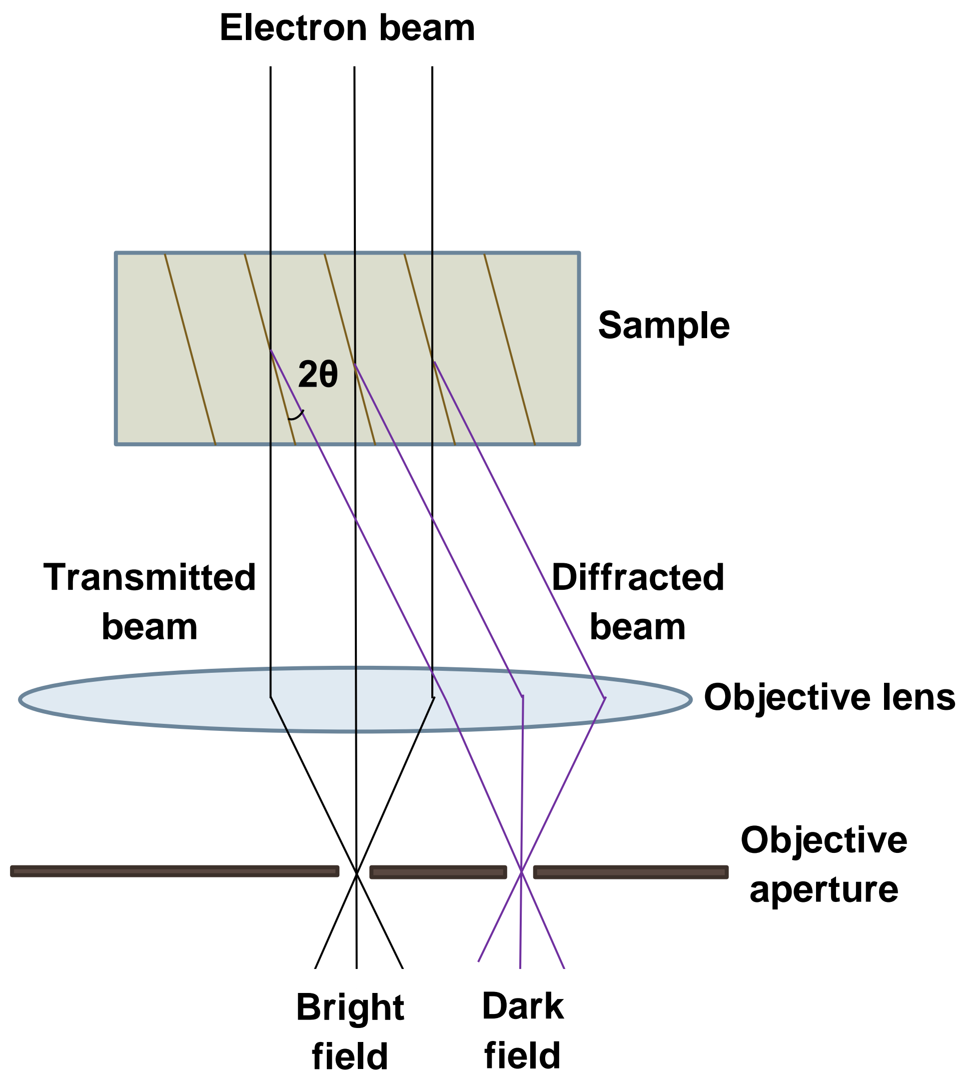

Fig. 2.14 Schematic of the two-beam imaging condition in TEM. An incident electron beam may be transmitted or diffracted at the Bragg condition. An objective aperture is used to select either the transmitted beam for bright-field imaging or a diffracted beam for dark-field imaging.

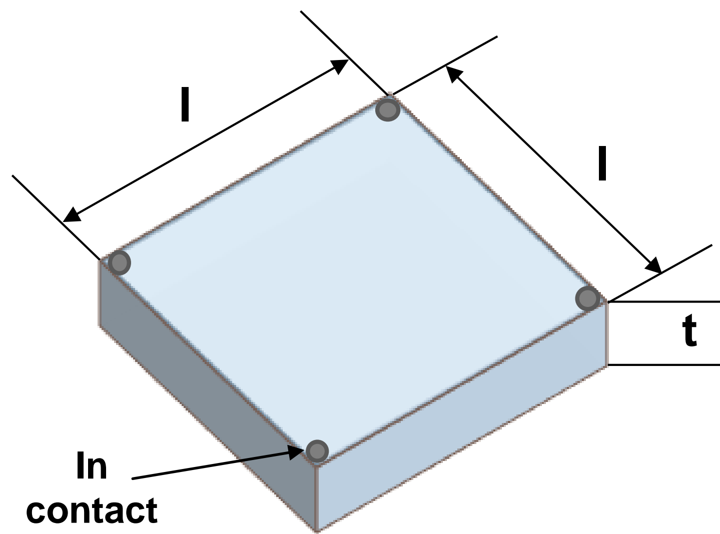

Fig. 2.15 Van der Pauw sample geometry used for resistivity and Hall measurements. Typically, l = 5 mm and t = 600 μm. ~0.5 mm In contacts are deposited at the corners of the sample.

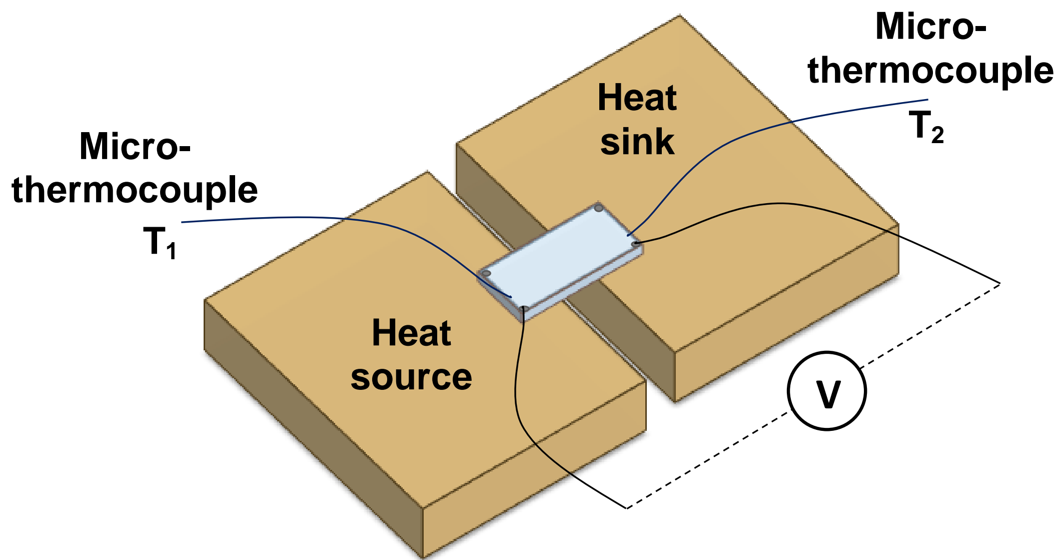

Fig. 2.16 Schematic of micro-thermocouple setup used to measure the Seebeck coefficient of GaAs:N samples. The sample is placed between a heat source (thermistor) and a heat sink; the temperature gradient at the sample surface (T_1-T_2) is measured by micro-thermocouple contacts. The resulting voltage difference due to the Seebeck effect is measured at indium contacts at the edges of the sample.

CHAPTER 3

BLISTER FORMATION IN ION-IMPLANTED GaAs: ROLE OF DIFFUSIVITY

3.1 Overview

This chapter describes our investigations of the influence of substrate temperature during implantation ("implantation temperature") on blister formation in GaAs:N layers produced by N ion implantation followed by rapid thermal annealing. In this chapter, the implantation temperature-insensitivity of blister formation behavior in GaAs:N is discussed and compared with contrasting behavior in light ion systems such as GaAs:H and Si:H. The apparent implantation temperature-insensitivity of blister formation in GaAs:N is likely due to the lower diffusivity of N in GaAs in comparison to that of H in GaAs and Si.

This chapter begins with background information on studies of blister formation, both as a detrimental side effect of irradiation processes as well as a useful tool for materials modification. Next, the experiments and simulations used to characterize blister formation behavior are described. The majority of this chapter focuses on the effect of implantation temperature on surface morphology, retained ion concentrations, and lattice damage in GaAs:N. The

chapter ends with a discussion of the role of ion-matrix diffusivity on blister formation in semiconductor materials.

3.2 Background

Localized surface deformation caused by the internal gas pressure of subsurface flaws or by residual stresses within near-surface layers is often termed "surface blistering," and has been observed following processes which involve ion-solid interactions.[1,2] These processes range from H^+ and D^+ irradiation-induced erosion of reactors to layer transfer by ion-cut following H^+ implantation into semiconductors.[3] In the case of ion-beam-assisted deposition (IBAD)[4] and depth profiling by secondary ion mass spectroscopy (SIMS),[5] surface blistering leads to defective IBAD films and compromises the SIMS depth resolution. Blister formation has also been studied as a by-product of radiation bombardment of spacecraft. For example, H irradiation-induced blistering increases the solar absorptance of Au films on Al substrates for thermal barrier coatings.[6]

On the other hand, ion-implantation-induced bubble and blister formation has been utilized to extract information about the mechanical properties of a system, or to modify material properties. For example, energy release rates deduced from blister geometry and gas pressure have been used to quantify the adhesion of metallic and ceramic coatings on metal substrates.[7] Noble-gas ion implantation has been used to introduce gas-bubble-induced pores in SiO_2 films,

thereby decreasing the dielectric constant.[8] He-implantation-induced cavities in Si have also been observed to getter metallic impurities.[9,10] Implantation-induced gas bubbles have been revealed by transmission electron micrographs (TEM) of voids[11] and by gas emission (revealed, for example, by thermal desorption spectroscopy) associated with bursting of surface blisters.[12,13]

In semiconductors, studies of implantation-induced blistering have focused on light ions (H or He) in Si and GaAs. Surface blistering of GaAs has been observed following ion implantation of H (Refs. 14-16) D (Ref. 17), and co-implantation of H and He (Ref. 18). In H-ion-implanted GaAs, blister formation has been reported within an implantation temperature window ranging from ~120 to ~300 °C.[19,20] Interestingly, in GaAs:H, the extent and depth-dependence of ion-implantation-induced lattice disorder increases with implantation temperature[19,20] up to ~300 °C. Above ~300 °C, the accumulation of gas required for bubble formation is presumably prevented by H out-diffusion.[19] For several semiconductors implanted with light ions, including Si:H, GaAs:H, and InP:H, bubble and blister formation are also dependent on the implantation temperature, and occur only within a temperature window that is specific to the particular ion-matrix system.[21,22] For the systems studied to date, it has been suggested that the lower-temperature bound is determined by lattice damage, while the upper-temperature bound is limited by the ion-matrix diffusivity.[21]

In this chapter, the key role of diffusion on the implantation temperature-dependence of blister formation is demonstrated. The focus is on GaAs:N, which exhibits low diffusivity for both highly-damaged[23] and crystalline[24] systems.

Thus, in comparing and contrasting the blister formation behavior of GaAs:N with lighter-ion systems, we have not only characterized the behavior of a "novel" system in terms of ion-matrix combination, but also illuminated the role of ion-matrix diffusivity on the origins of blister formation.

3.3 Experiments and Simulations

For this study, undoped or Si-doped GaAs films were implanted with 100 keV nitrogen ions at a fluence of 5 x 10^{17} cm^{-2}, as described in Section 2.2. During implantation, the substrate temperature was maintained at -196 °C or 300 °C, as determined by a J-type thermocouple attached to the back of the sample holder. The corresponding samples are referred to as "low-*T*-implanted" and "high-*T*-implanted," respectively. Some of these samples were subsequently rapid thermal annealed (RTA) in nitrogen or argon gas for 30 sec at 800 °C. Tapping-mode atomic force microscopy (AFM) was performed in a Digital Instruments NanoScope IIIA, using etched Si tips, as described in Section 2.4. To enable collection of both scanning electron (SEM) and atomic force (AFM) micrographs of the same areas, surface markers were fabricated using focused-ion-beam (FIB) milling of trenches.

The retained N dose and the depth-dependence of the N concentration, [N], were determined with nuclear reaction analysis (NRA) using the $^{14}N(d,\alpha_1)^{12}C$ reaction, as described in Section 2.5.2. A 300 μm thick particle detector was

placed at 150º where the cross-section is known.[25] Details of the dose calculation are provided in Appendix A.1.

To compare the lattice damage induced by low- and high-temperature implantations, the depth-dependence of lattice disorder was determined by channeling-Rutherford backscattering spectrometry (RBS) with a 2 MeV He^{++} beam. The uncertainty of the energy resolution at the detector was estimated at ~20 keV. The size of the beam on the sample was ~1 mm in diameter. SIMNRA[26] software was used to simulate backscattered spectra for channel-to-energy conversions to compare data from different irradiation sessions. This software was also used to determine energy-to-depth conversions according to calculated energy losses of He^{++} in the GaAs matrix, as described in Appendix A.2.

3.4 Surface Morphology and Retained N Fluence

To examine the origins of blister formation, scanning electron micrographs (SEM) of the surfaces of (a) as-grown, (b) as-grown-plus-annealed, (c) high-*T*-implanted, and (d) high-*T*-implanted-plus-annealed GaAs layers were compared.[27] As shown in Figs. 3.1(a) and 3.1(c), the surfaces of the as-grown and as-implanted layers appear featureless. Interestingly, surface features are apparent on the annealed GaAs surface, as shown in Fig. 3.1(b).

The stoichiometries of GaAs surfaces before and after implantation and/or annealing were compared by energy dispersive X-ray spectroscopy, as shown in

Fig. 3.2. The as-grown and as-implanted spectra (shown in Fig. 3.2(a) and 3.2(c), respectively) reveal features associated with $L_{\alpha 1}$ (K_{α}) x-ray emission from Ga and As (O and C). However, the As features are essentially absent from the as-annealed and implanted-plus-annealed spectra (shown in Fig. 3.2(b) and 3.2(d), respectively). Thus, the surface roughness observed in the as-annealed surface is likely due to near-surface As loss[28] during RTA. However, surface blisters and craters (popped blisters) are observed in the implanted-plus-annealed case as revealed by the SEM image in Fig. 3.1(d).

The normalized NRA yields versus ion energy for low-*T*-implanted and high-*T*-implanted layers are shown in Fig. 3.3. The similar ion-energy-dependence of the yields suggests similar N depth profiles in both cases. The estimated retained fluences of low-*T*-implanted and high-*T*-implanted layers are (4.9±0.3) and (4.8±0.3) x 10^{17} cm^{-2}, respectively. The retained fluences were estimated from the integrated counts under the alpha-particle peaks, as described in Appendix A.1. The similarity of the estimated retained fluences to that of the target fluence (5.0×10^{17} cm^{-2}) indicates near-complete N retention in GaAs:N, even for the 300 °C-implanted sample. This is in contrast to GaAs:H, for which the retained H fluence in a 300 °C implant was 32% lower than that for a -90 °C implant,[19] presumably due to H out-diffusion.

Postannealing surface morphology and local variations in crater depths were examined using SEM images of low-*T*-implanted-plus-annealed and high-*T*-implanted-plus-annealed layers, as shown in Figs. 3.4(a) and 3.4(c). AFM images of the corresponding areas are shown in Figs. 3.4(b) and 3.4(d). In both

cases, SEM images reveal blistered surfaces with similar feature sizes and densities. Examples of ~2 μm diameter blisters and craters are highlighted in Figs. 3.4(a) and 3.4(c) by solid and dashed circles, respectively. Line-cuts from the AFM images in Figs. 3.4(b) and 3.4(d) reveal ~200 nm crater depths for both the low- and high-*T*-implanted-plus-annealed layers. These crater depths agree with the depth of maximum N concentration predicted by SRIM simulations,[29] as shown in Fig. 3.5, suggesting that bubbles form near the projected ion range.

The origin of the blisters and craters are further illustrated by cross-sectional SEM as shown in Fig. 3.6. In this case, a trench was fabricated using a Ga^+ FIB and the resulting cross section imaged in SEM, as shown in Fig. 3.6(a). The composite SEM image presented in Fig. 3.6(b) shows that the depth of subsurface voids associated with intact blisters essentially coincides with the depth of exfoliated craters. This suggests that both blisters and craters occur due to gas bubble formation ~200 nm beneath the surface, again confirming bubble formation near the projected ion range. The similarity of the predicted depth of maximum N concentration to that of the crater formation observed by SEM and AFM, as well as the nearly complete retention of implanted N revealed by NRA, suggest insignificant diffusion of N during the annealing step.

3.5 Lattice Damage Profiles

To compare the implantation-temperature-dependence of the damage depth distributions in N-implanted and/or annealed GaAs, (001) channeling-RBS

measurements were performed. Figure 3.7 presents the normalized yield versus energy and depth for low-*T* and high-*T* (a) implanted and (b) implanted-plus-annealed GaAs layers. For comparison, random and (001) channeling yields from as-grown GaAs are included on the plots. The ratio of the channeling-RBS yield to the random yield (χ) is a measure of the fraction of ions which were de-channeled, presumably due to lattice disorder. In this case, the minimum channeling ratio (χ_{min}) for the as-grown layers was found to be ~4%, similar to previous measurements[30-32] of MBE-grown GaAs. This χ_{min} is also similar to the predicted[33,34] χ_{min} for defect-free GaAs (~3%), indicating high crystalline quality and good alignment of the incident beam with (001) planes.

For both the low-*T* and high-*T*-implanted layers, similar depth-dependencies of the normalized yield are apparent in Fig. 3.7(a), suggesting similar damage depth profiles for both cases. The low-*T*-implanted sample exhibits a slightly wider depth profile (at ~300 nm) compared to that of the high-*T*-implanted sample. Although the minor differences between the spectra are at the level of the detector energy resolution (±20 keV), similar shifts in damage recovery with increasing implantation temperature have been reported in GaAs:N.[35] It is possible that this slightly narrower damage depth profile for the high-*T*- versus the low-*T*-implanted sample is due to a greater extent of thermally-activated point-defect recombination in the high-*T*-implanted sample. For example, TEM images of platelets (extended lattice defects) formed in H-implanted Si show reduced image contrast in the vicinity of platelets with increasing annealing temperature.[36] The reduced image contrast is attributed to

a temperature-dependent reduction in lattice strain with temperature, presumably due to the thermally-activated recombination of implantation-induced Frenkel (vacancy-interstitial) defects.

However, this similarity of the backscattered yield in low-*T*- and high-*T*-implanted GaAs:N is in contrast to the temperature-dependent behavior observed in GaAs:H. In GaAs:H it was observed that both the magnitude and depth distribution of the normalized yield varied for -90 to 320 °C implantation temperatures.[19,20] In our case, little redistribution of lattice damage is apparent for -196 ^{o}C and 300 ^{o}C implantations.

The energy-dependence of the normalized RBS yield for implanted layers following annealing is presented in Fig. 3.7(b). The annealed layers (without implanted N) exhibit a near-surface maximum at ~1580 keV, most likely due to As loss from the top ~50 nm of the layer. In addition, the implanted-plus-annealed layers exhibit a local maximum in the normalized RBS yield at ~1480 keV, which corresponds to a depth of ~200 nm beneath the surface. The value of this local maximum in yield is similar to that of the random GaAs case, and its depth corresponds to that of the observed bubble formation, as well as to the crater depth formation and predicted depth of maximum [N] shown in Figs. 3.4 and 3.5. Thus, it is likely that this local maximum in yield is due to dechanneling of He^{++} at the Ga or As atoms displaced by N bubble-induced internal surfaces and strain fields,[37] confirming the implantation-temperature-insensitivity of bubble-formation depths.

3.6 Diffusivity-driven Blister Formation

The implantation-temperature-insensitivity of crater depths, average damage depth profiles, and ion depth profiles for GaAs:N can be explained in the context of diffusivity-driven blister formation. In GaAs, implantation-temperature-dependent blistering has been observed for implantation of H[19,20] and/or He[38] ions, both of which exhibit substantially higher diffusivities (D) than that of N in GaAs at the implantation temperature ranges associated with blister formation, as shown in Table 3.1. Where possible, the diffusivities are extrapolated to 300 ºC, which is an implantation temperature for which blister formation is not observed for GaAs:H[19] but is observed in our case for GaAs:N. Using the extrapolated diffusivites and assuming a typical implantation time of 10 hours, an estimate of the diffusion distance,[39] $x = (Dt)^{1/2}$, for H versus N in GaAs gives $x_H \approx 1.9$ cm, several orders of magnitude larger than $x_N \approx 600$ nm. Thus, the absence of surface blistering on GaAs:H for implantation temperatures > 300 °C is likely related to significant H redistribution and out-diffusion, which has also been observed experimentally, for implantation temperatures > 200 °C.[40] In this section, the blister formation behavior of GaAs:N is discussed in comparison to that of GaAs:H and the contrasting behavior is explained in terms of a model of blister formation incorporating ion-matrix diffusivity.

To date, models of blister formation incorporate both extended lattice defects as well as diffusion of implanted ions as necessary components for both bubble and blister formation.[44,46] Various crystal defects have been observed to

act as precursors for bubble formation. For example, implantation damage is thought to lead to extended lattice defects (platelets)[11] that evolve into internal surfaces that act as bubble nucleation sites. In metals, the presence of alloying elements is observed to affect the size and density of He bubbles,[41] and grain boundaries appear to act as preferential nucleation sites.[42,43] In addition to the requirement for existing crystal defects, the implanted species must be mobile enough to diffuse into these defects and form gas bubbles. Figure 3.8 presents an illustration of this model as applied to the Si:H system,[44] in which it is proposed that hydrogen diffuses into extended lattice defects to form bubbles. Thus, we will refer to this model as the "defect/diffusion model." Although in the case of Si:H this model includes chemistry-specific details (for example, H interaction with Si to form compounds[45] or H passivation of internal Si surfaces[46]), the general features of the model appear to hold for other, less chemically-active, ions. For example, He implantation in Si also creates extended defects,[36,47] which lead to bubble formation following thermally-activated diffusion and coalescence[48] of He into the defects.

The defect/diffusion model has been used to explain the implantation-temperature-dependence of blister formation in several light-ion implanted semiconductor and oxide systems.[21] The lower temperature bound is attributed to a minimum defect mobility for extended defects such as platelets to form. The upper temperature bound, in turn, is associated with out-diffusion of the implanted species, preventing gas accumulation inside platelets. It is likely that the apparent temperature-insensitivity and wider temperature window for blister

formation in GaAs:N is due to the intrinsically lower diffusivity of N in GaAs as compared to H or He in GaAs or Si.

Table 3.1: Comparison of reported diffusion parameters for various ions in GaAs and Si. In each case, the ion implantation or film growth details are listed along with the temperature *T* associated with diffusion parameters given by the Arrhenius expression $D = D_o\exp(-Q/RT)$, where *D* is the diffusivity or diffusion coefficient, D_0 is the diffusion coefficient pre-factor, *Q* is the activation energy for diffusion, and *R* is the gas constant (8.314 J-mol^{-1}K^{-1}). For comparison at a typical blister formation temperature, *D* is extrapolated to 300 °C where applicable. The estimated *D*(300 °C) of GaAs:N is orders of magnitude lower than that of other light ions in GaAs and Si (see references in table).

System	Technique	*T*(°C)	*Q* (eV)	D_o (cm^{2}s^{-1})	*D* (cm^{2}s^{-1})	*D*(300 °C) (cm^{2}s^{-1})
GaAs:N[23]	Ion implantation (50 keV, 7.5x10^{15} cm^{-2})	830	1.1	n/a	4.5x10^{-12}	~ 10^{-17}
GaAs:N[24]	MBE growth: solid-source MBE (GaAs) and rf-plasma excitation of N_2 (GaAsN)	800-1200	n/a	n/a	3.5x10^{-12}	n/a
GaAs:H[49]	Ion implantation (60 keV, 1x10^{16} cm^{-2})	196-496	2.16	2x10^5	n/a	~ 10^{-14}
GaAs:He[38]	Ion implantation (105 keV, 5x10^{16} cm^{-2})	325	0.41	1x10^{-9}	n/a	~ 10^{-13}
Si:H[51]	Plasma hydrogenation (500eV – 2keV)	100-300	0.58	1x10^{-4}	n/a	~ 10^{-10}

The implantation-temperature-insensitivity of blister formation in GaAs:N may also be explained in terms of the distinct diffusion mechanism of N in GaAs versus H in GaAs or Si. Indeed, H diffusion in both Si[51] and GaAs[49] has been reported to depend on lattice damage, presumably due to the reported dominance of hydrogen-vacancy-pair diffusion in those systems. For example, in Si:H, an upper-bound implantation temperature for blister formation of ~450 °C is reported,[21] and for high dose, room temperature-implanted Si:H,[50] blister formation was not observed. This is presumably due to enhanced diffusivity of H in that case, due to hydrogen-vacancy complex diffusion. For example, Sopori *et al.*[51] find that H diffusivity increases in Si with increased vacancy concentration (attributed to carbon impurities). In contrast, the observed damage-insensitivity of blister formation in GaAs:N is likely related to an interstitial kick-out diffusion mechanism, reported for N in GaAs[24] and shown schematically in Fig. 3.9(a-d), which would not be influenced by vacancies. As shown in Table 3.1, low diffusivities have been observed in GaAs:N, apparently independent of the level of implantation-induced damage.

However, one caveat that should be addressed in discussing the reported low diffusivity of N in GaAs is the possibility of radiation-enhanced diffusion (RED). In RED, Frenkel defects created by radiation damage may accelerate vacancy or interstitial-driven diffusion processes during irradiation.[52] However, the diffusivity value reported in Ref. 23 in Table 3.1 for N-implanted GaAs is based on measured N profiles for annealing experiments post-implantation. Thus, this diffusivity value does not take into account the possibility of RED

during implantation in GaAs:N, and we cannot rule out the possibility that RED may enhance the diffusivity of GaAs:N during implantation. Finally, it is also worth noting that the predicted solubility of N in GaAs (< 10^{14} cm^{-3} at ~700 ºC)[53,54] is much less than the estimated solubility[55] of H in GaAs ($O(10^{20})$ cm^{-3} at ~500 ºC), indicating that precipitation of N in GaAs is more likely than precipitation of H in GaAs.

The role of diffusivity in bubble formation is further supported by comparison of the exfoliation depths in GaAs:N and Si:H. In Si:H, with increasing implantation temperature, the exfoliation depth varies from the depth of maximum ion concentration to that of maximum lattice damage,[56] where presumably a higher concentration of extended lattice defects acts as bubble nucleation sites. Indeed, in many ion-implanted structures, the depth of maximum damage is often less than that of the ion range.[44,57] On the other hand, in GaAs:N, the exfoliation depth remains at the depth of maximum ion concentration, even for high-*T*-implantation and annealing.

3.7 Conclusions

In summary, we have examined the influence of implantation temperature on blister formation in GaAs:N. Local crater depths, average damage depth profiles, and retained N doses were similar for both low-*T* and high-*T* implantations. This is in contrast to the implantation temperature-dependence of these parameters observed in light ion, high-diffusivity systems such as GaAs:H

and Si:H. Thus, the low ion-matrix diffusivity of GaAs:N, which is independent of the extent of lattice damage, leads to implantation temperature-insensitive exfoliation depths and damage depth profiles. The low ion-matrix diffusivity of GaAs:N may be beneficial for the stable precipitation of bubbles across a wide range of processing temperatures.

These results also illuminate the role of ion-matrix diffusivity on the presence of temperature windows for blister formation in ion-implanted semiconductors. In GaAs:N, we observe blister formation at implantation temperatures outside the windows observed for GaAs:H and Si:H. For example, in our case, blister formation is observed at 300 ^{o}C, higher than the upper temperature bound observed for GaAs:H and Si:H. It is likely that the low ion-matrix diffusivity of GaAs:N prevents significant redistribution or out-diffusion that would otherwise prevent bubble formation at high temperatures. Similarly, we observe blister formation at -196 ^{o}C, much lower than the lower-bound temperatures observed in GaAs:H and Si:H. In our case, the high N-implantation-induced damage (observed by channeling-RBS) may preclude the need for defect diffusion in nucleating bubble precursors. These results suggest that ion-matrix diffusivity influences the temperature-dependence of blister formation.

3.8 References

[1] B. M. U. Scherzer, in *Topics in Applied Physics: Sputtering by particle bombardment II*, edited by R. Behrisch (Springer, Berlin, 1983), Vol. **52**, Chap. 7, p. 271-355.

[2] S. K. Das and M. Kaminsky, J. Nucl. Mat. **53**, 115 (1974).

[3] M. Bruel, Electron. Lett. **31**, 1201 (1995).

[4] C. H. Liu, Y.-J. He, W.-Z. Li, and H.-D. Li, Nucl. Instrum. Methods Phys. Res. B **122**, 229 (1997).

[5] K. J. Kim, D. W. Moon, K.-H. Jung, and I. C. Jeon, J. Vac. Sci. Technol. A **16**, 2919 (1998).

[6] D. L. Anderson and R. G. Dahms, Proceedings AIAA-ASME Structures and Materials Conference (New York, 1966) 216.

[7] R. E. Galindo, A. van Veen, J. H. Evans, H. Schut, and J.Th.M. de Hosson, Thin Solid Films **471**, 170 (2005).

[8] E. Ntsoenzok, H. Assaf, and M. O. Ruault, Mater. Res. Soc. Symp. Proc. **864**, 327 (2005).

[9] V. Rainieri, P. G. Fallica, G. Percolla, A. Battaglia, M. Barbagallo, and S. U. Campisano, J. Appl. Phys. **78**, 3727 (1995).

[10] S. M. Meyers, G. A. Petersen, and C. H. Seager, J. Appl. Phys. **80**, 3717 (1996).

[11] M. K. Weldon, V. E. Marisco, Y. J. Chabal, A. Agarwal, D. J. Eaglesham, J. Sapjeta, W. L. Brown, D. C. Jacobson, Y. Caudano, S. B. Christman, and E. E. Chaban, J. Vac. Sci. Technol. B **15,** 1065 (1997).

[12] B. Terreault, G. Ross, R. G. St.-Jacques, and G. Veilleux, J. Appl. Phys. **51**, 1491 (1980).

[13] W. M. Shu, Appl. Phys. Lett. **92**, 211904 (2008).

[14] G. Gawlik, J. Jagielski, and B. Piatkowski, Vacuum **70**, 103 (2003).

[15] M. Webb, C. Jeynes, R. M. Gwilliam, Z. Tabatabaian, A. Royle, and B. J. Sealy, Nucl. Instrum. Methods Phys. Res. B **237**, 193 (2005).

[16] M. Webb, C. Jeynes, R. Gwilliam, P. Too, A. Kozanecki, J. Domagala, A. Royle, and B. Sealy, Nucl. Instrum. Methods Phys. Res. B **240**, 142 (2005).

[17] A. Giguère, N. Desrosiers, and B. Terreault, Appl. Phys. Lett. **87**, 211911 (2005).

[18] I. Radu, I. Szafraniak, R. Scholz, M. Alexe, and U. Gösele, J. Appl. Phys. **94**, 7820 (2003).

[19] M. Webb, C. Jeynes, R. Gwilliam, P. Too, A. Kozanecki, J. Domagala, A. Royle, and B. Sealy, Nucl. Instrum. Methods Phys. Res. B **240**, 142 (2005).

[20] G. Gawlik, R. Ratajczak, A. Turos, J. Jagielski, S. Bedell, and W. L. Lanford, Vacuum **63**, 697 (2001).

[21] Q.-Y. Tong, L.-J. Huang, and U. M. Gösele, J. Electron. Mater. **29**, 928 (2000).

[22] P. Chen, Z. Di, M. Nastasi, E. Bruno, M. G. Grimaldi, N. D. Theodore, and S. S. Lau, Appl. Phys. Lett. **92**, 202107 (2008).

[23] S. Amine, G. Ben Assayag, C. Bonafos, B. de Mauduit, H. Hidriss, and A. Claverie, Mater. Sci. Eng. B **93**, 10 (2002).

[24] G. Bösker, N. A. Stolwijk, J. V. Thordson, U. Södervall, and T. G. Andersson, Phys. Rev. Lett. **81**, 3443 (1998).

[25] S. Pellegrino, L. Beck, and P. Trouslard, Nucl. Instrum. Methods Phys. Res. B **219-220**, 140 (2004).

[26] M. Mayer, SIMNRA Users Guide, Report IPP 9/113 (Max-Plank-Institut für Plasmaphysik, Garching, Germany, 1997).

[27] R. R. Collino, B. B. Dick, F. Naab, Y. Q. Wang, M. D. Thouless, and R. S. Goldman, Appl. Phys. Lett. **95**, 111912 (2009).

[28] G. Gagnon, A. Houdayer, J. F. Currie, and A. Azelmad, J. Appl. Phys. **70**, 1036 (1991).

[29] J.F. Ziegler, J.P. Biersack, and U. Littmark, The Stopping and Range of Ions in Matter (Pergamon, New York, 1985).

[30] M. Reason, PhD Thesis, University of Michigan, Ann Arbor, MI, 2006.

[31] T. Ahlgren, E. Vainonen-Ahlgren, J. Likonen, W. Li and M. Pessa, Appl. Phys. Lett. **80**, 2314 (2002).

[32] G.E. Höfler and K.C. Hsieh, Appl. Phys. Lett. **61**, 327 (1992).

[33] B.J. Wilkens, J.A. Martinez, S. Mounier and C.J. Palmstrom, J. Appl. Phys. **70**, 4890 (1991).

[34] K. Gärtner, Nucl. Instrum. Methods Phys. Res. B **132**, 147 (1997).

[35] A. Turos, A. Stonert, B. Breeger, E. Wendler, W. Wesch, and R. Fromknecht, Nucl. Instrum. Methods Phys. Res. B **148**, 401 (1999).

[36] R. Tonini, F. Corni, S. Frabboni, G. Ottaviani, G. F. Cerofolini, J. Appl. Phys. **84**, 4802 (1998).

[37] M. B. H. Breese, L. C. Alves, T. Hoechbauer, and M. Nastasi, Appl. Phys. Lett. **77**, 268 (2000).

[38] I. Radu, PhD Thesis, Max Planck Institute of Microstructure Physics, Halle, Germany, 2003.

[39] P. Shewmon, *Diffusion in Solids*, (TMS, Warrendale, 1989).

[40] J. M. Zavada and R. G. Wilson, Mat. Sci. Forum **148-149**, 189 (1994).

[41] B. A. Kalin, I. I. Chernov, A. N. Kalashnikov, S. Yu. Binyukova, A. A. Timofeev, and A. I. Dedyurin, At. Energy **92**, 50 (2002).

[42] F. Carsughi, H. Ullmaier, H. Trinkaus, W. Kesternich, and V. Zell, J. Nucl. Mater. **212-215**, 336 (1994).

[43] P. A. Thorsen, J. B. Bilde-Sørensen, and B. N. Singh, Mat. Sci. Forum **207-209**, 445 (1996).

[44] T. Höchbauer, A. Misra, M. Nastasi, and J. W. Mayer, J. Appl. Phys. **92**, 2335 (2002).

[45] G. F. Cerofolini, R. Balboni, D. Bisero, F. Corni, S. Frabboni, G. Ottaviani, R. Tonini, R. S. Brusa, A. Zecca, M. Ceschini, G. Giebel, and L. Pavesi, Phys. Stat. Sol. A **150**, 539 (1995).

[46] B. Terreault, Phys. Stat. Sol. A **204**, 2129 (2007).

[47] S. Frabboni, F. Corni, C. Nobili, R. Tonini, and G. Ottaviani, Phys. Rev. B **69**, 165209 (2004).

[48] V. M. Vishnyakov, S. E. Donnelly, G. Carter, R. C. Birtcher, and L. Haworh, Solid State Phenom. **82-84**, 267 (2002).

[49] J. Räisänen, J. Keinonen, V. Karttunen, and I. Koponen, J. Appl. Phys. **64**, 2334 (1988).

[50] V. P. Popov, I. E. Tyschenko, L. N. Safronov, O. V. Naumova, I. V. Antonova, A. K. Gutakovsky, and A. B. Talochkin, Thin Solid Films **403-404**, 500 (2002).

[51] B. L. Sopori, X. Deng, J. P. Benner, A. Rohatgi, P. Sana, S. K. Estreicher, Y. K. Park, and M. A. Roberson, Sol. Energy Mater. Sol. Cells **41-42**, 159 (1996).

[52] M. Nastasi, J. W. Mayer, and J. K. Hirvonen, *Ion-solid Interactions: Fundamentals and Applications,* (Cambridge University Press, Cambridge UK , 1996), p. 205.

[53] I. Ho and G. B. Stringfellow, J. Cryst. Growth **178**, 1 (1997).

[54] S. B. Zhang and A. Zunger, Appl. Phys. Lett. **71**, 677 (1997).

[55] J. H. Neethling, Physica B **170**, 285 (1991).

[56] J. K. Lee, M. Nastasi, N. D. Theodore, A. Smalley, T. L. Alford, J. W. Mayer, M. Cai, and S. S. Lau, J. Appl. Phys. **96**, 280 (2004).

[57] J. Mayer, L. Eriksson, and J. Davis, *Ion Implantation in Semiconductors* (Academic, New York, 1970).

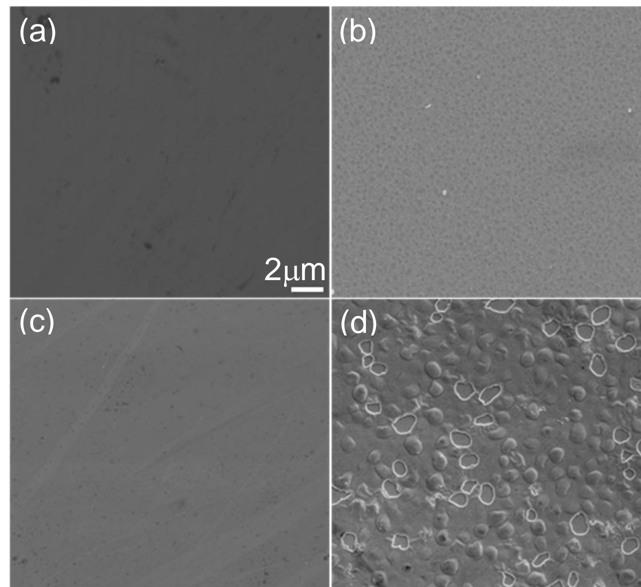

Fig. 3.1 SEM images of (a) as-grown (b) annealed (c) high-*T*-implanted and (d) high-*T*-implanted-plus-annealed GaAs. Surface features are not apparent in both (a) as-grown and (c) high-*T*-implanted samples. For the (b) annealed and (d) high-*T*-implanted-plus-annealed films, surface pitting and blistering are apparent, respectively. Reprinted with permission from R. R. Collino *et al.*, Appl. Phys. Lett. **95**, 111912 (2009). Copyright 2009, American Institute of Physics.

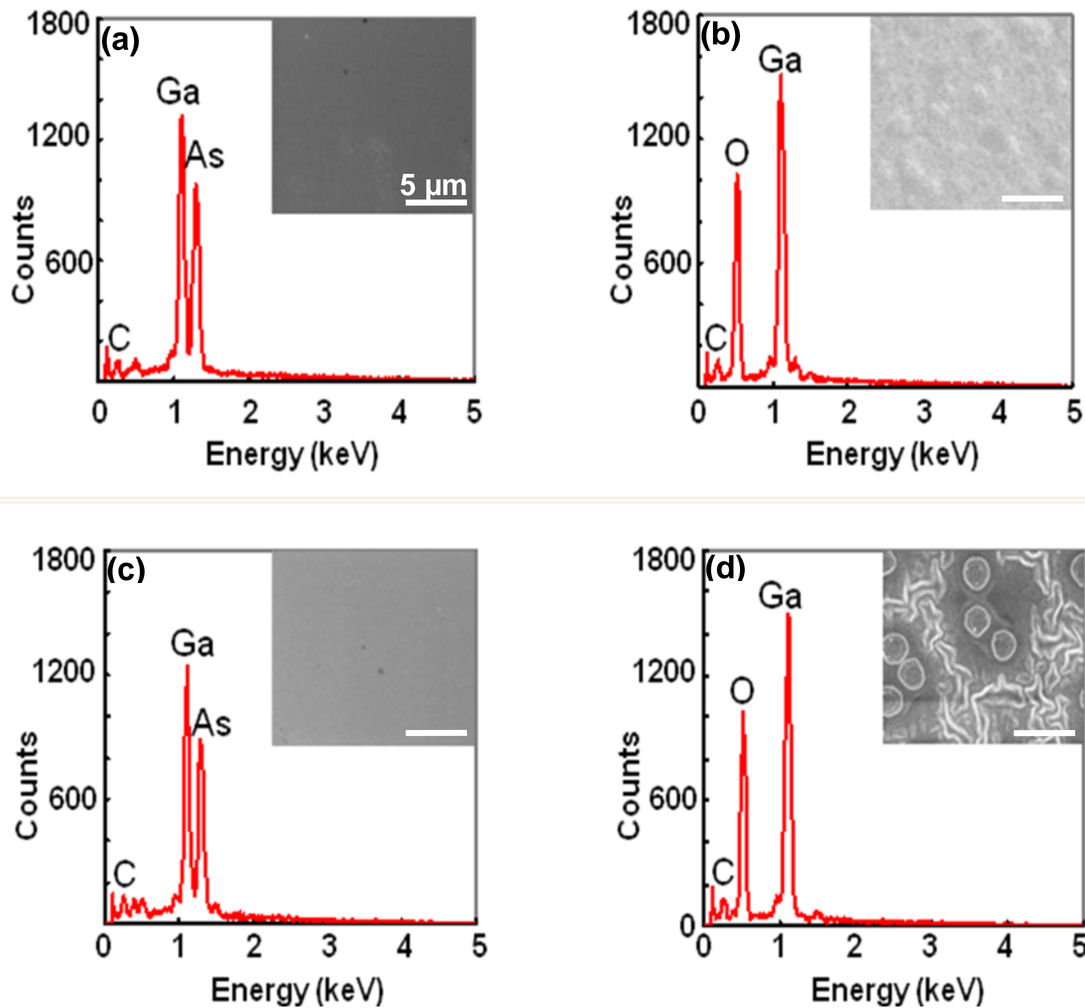

Fig. 3.2 X-ray energy dispersive spectra of (a) as-grown (b) rapid-thermal annealed (850 °C in N_2) (c) as-implanted and (d) implanted-plus-annealed GaAs layers, with features corresponding to $L_{\alpha 1}$ (K_{α}) x-ray emission from Ga and As (O and C). The corresponding SEM images are shown as insets and represent the entire sampled area (~200 µm^2). The annealed surfaces exhibit apparent loss of As. In the case of the implanted + annealed layers, spot scans (not shown) revealed similar surface stoichiometries for elongated features and craters. All of the spectra shown were collected with incident electron energy of 5.0 keV, for a duration of 240 s.

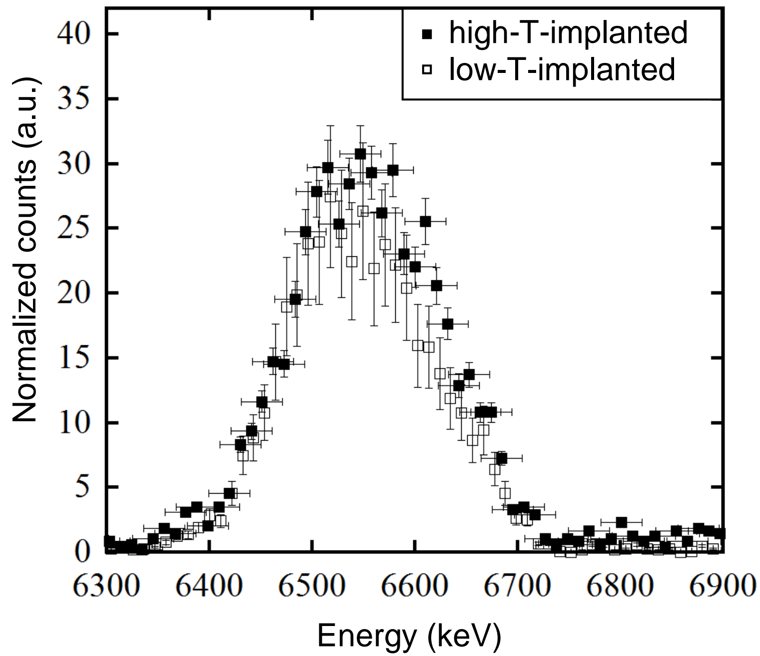

Fig. 3.3 NRA spectra of α_1 particle yield vs. energy in low-*T* and high-*T*-implanted GaAs. The similarity of counts vs. energy between the two samples indicates that the retained fluence (estimated from integrated peak areas) and [N] depth profile are similar for both. Reprinted with permission from R. R. Collino *et al.*, Appl. Phys. Lett. **95**, 111912 (2009). Copyright 2009, American Institute of Physics.

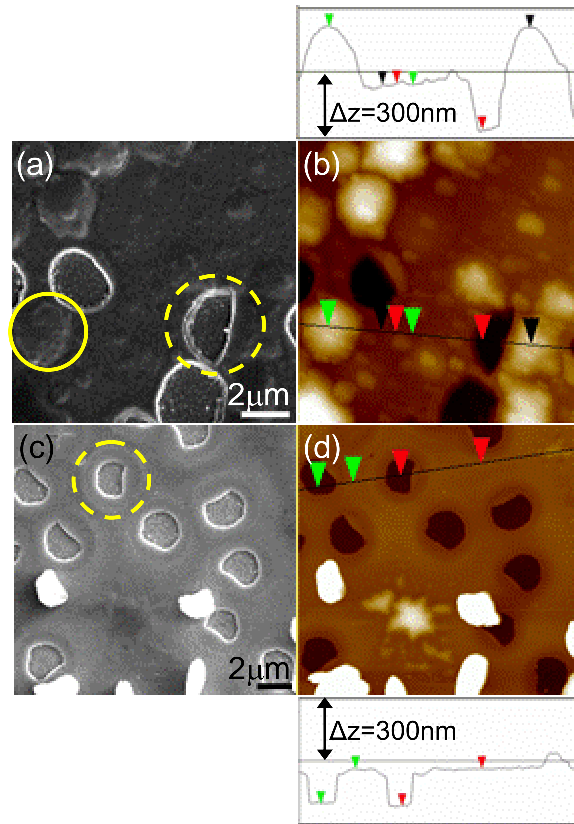

Fig. 3.4 SEM (AFM) images of (a, (b)) low-*T*-implanted and (c, (d)) high-*T*-implanted-plus-annealed samples. SEM images in (a) and (c) reveal circular blisters and craters ~2 μm in diameter (highlighted with solid and dashed circles, respectively in (a)) for both low- and high-temperature implantations. AFM images of the same areas are shown in (b) and (d). The cross-sectional profiles reveal crater depths of ~200 nm in both cases. Reprinted with permission from R. R. Collino *et al.*, Appl. Phys. Lett. **95**, 111912 (2009). Copyright 2009, American Institute of Physics.

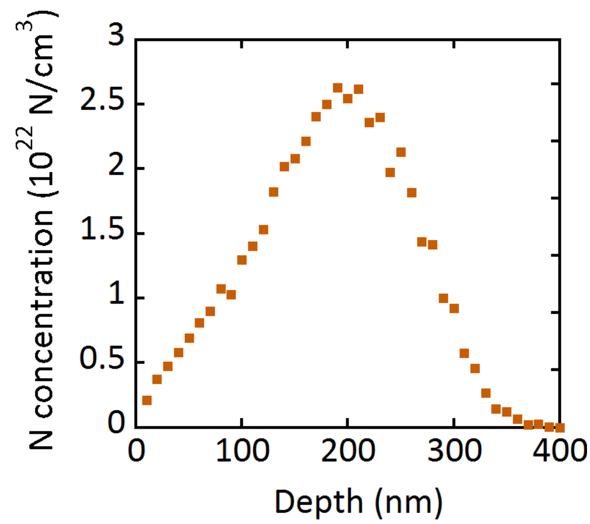

Fig. 3.5 Depth profile predicted by Monte Carlo simulations (SRIM Code) for 100 keV N^+ ions implanted at $5x10^{17}$ cm^{-2}. Inputs to the calculation included a 7° angle of incidence and 100,000 ions.

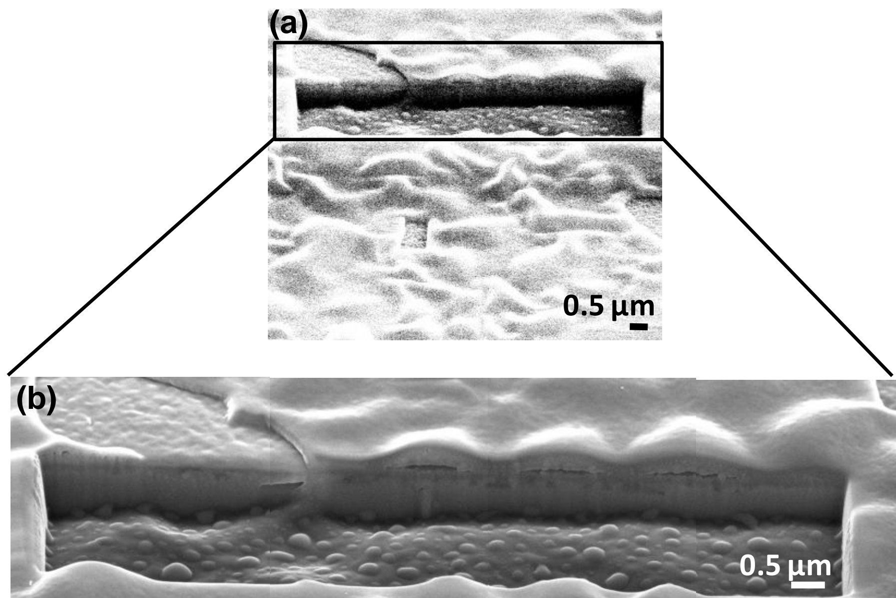

Fig. 3.6 (a) SEM image (52° sample tilt) of a blistered surface with both circular blisters and craters. A FIB trench (shown in the box) was fabricated to view near-surface layers in cross-section. (b) Detail of cross section, cut through both intact blisters as well as crater, showing that the apparent crater 'floor' coincides with the depth of blister formation, suggesting that the craters are remnants of popped blisters.

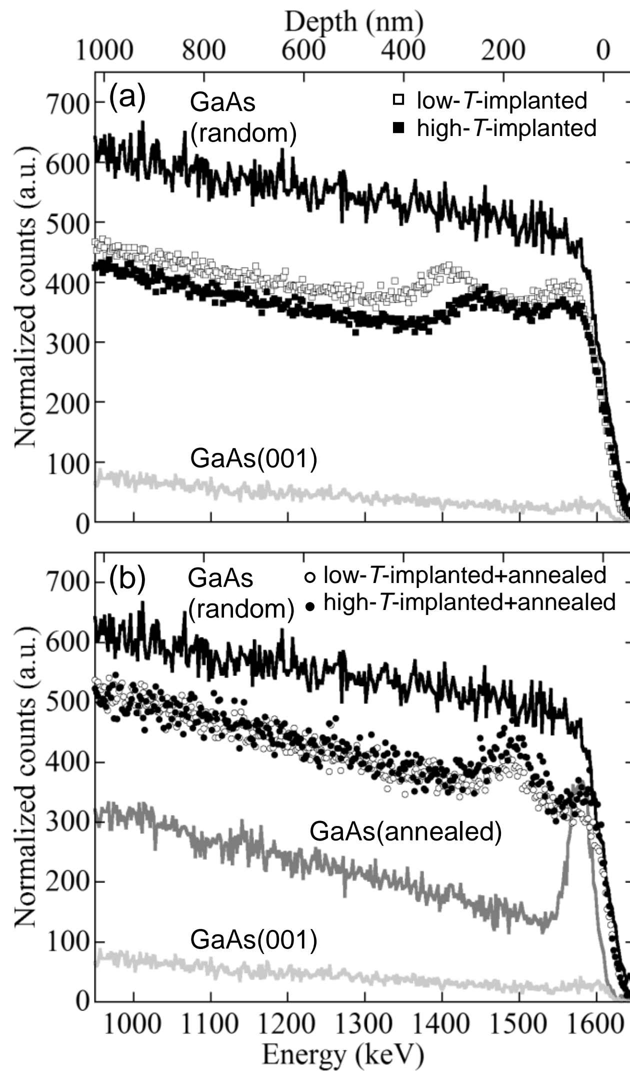

Fig. 3.7 Channeling-RBS spectra as a function of backscattered energy of GaAs layers (a) before and (b) after annealing, comparing low-*T*- (open symbols) and high-*T*- (closed symbols) implanted samples with GaAs in the random and (001) aligned configurations. In both cases, the normalized yield is similar for the low-*T* and high-*T* samples, suggesting similar lattice damage. The implanted-plus-annealed spectra in (b) exhibit local maxima at ~1480 keV (corresponding to ~200 nm), attributed to dechanneling by bubbles. Reprinted with permission from R. R. Collino *et al.*, Appl. Phys. Lett. **95**, 111912 (2009). Copyright 2009, American Institute of Physics.

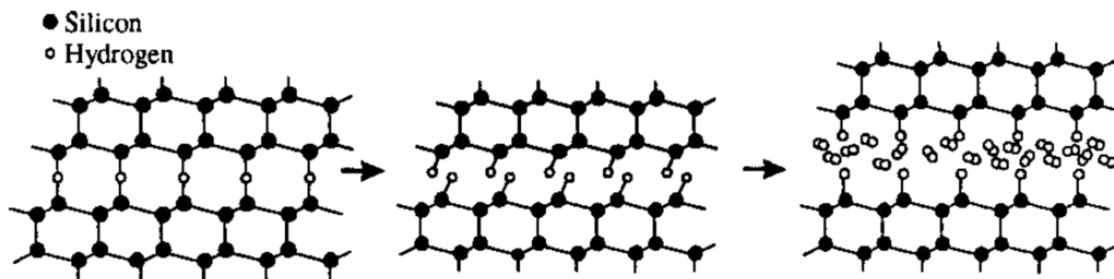

Fig. 3.8 Model of platelet and bubble formation in H-implanted Si. In the first step, implanted H is thought to occupy bond-centered sites in the silicon lattice. In the second step, themal annealing results in silicon hydride that aids in the formation of {100} platelets by passivating internal surfaces. In the third step, further annealing leads to the coalescence of H_2 gas bubbles, resulting in blister formation or splitting. Reprinted with permission from T. Höchbauer, A. Misra, M. Nastasi, and J. W. Mayer, J. Appl. Phys. **92**, 2335 (2002). Copyright 2002, American Institute of Physics.

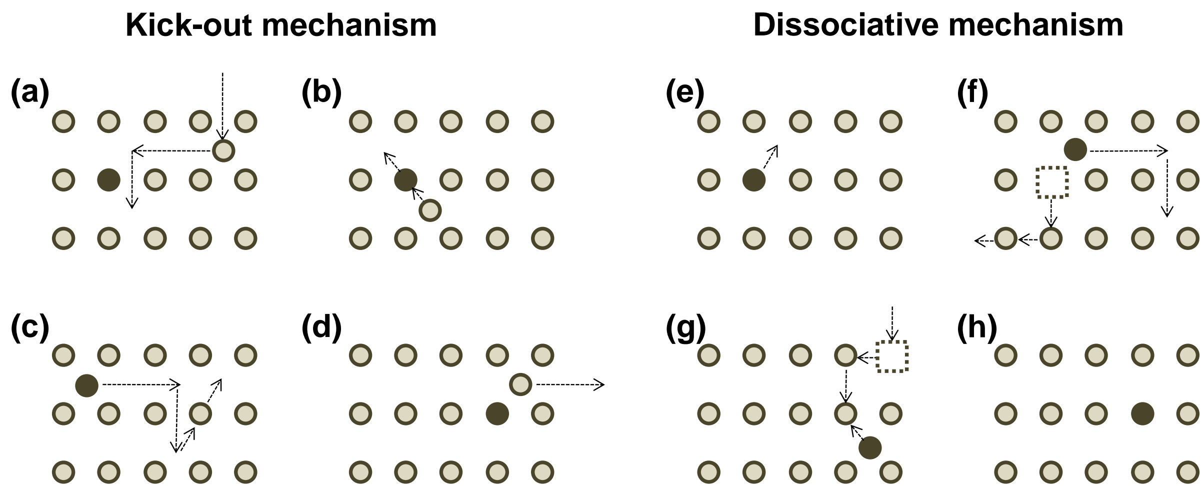

Fig. 3.9 Schematic models of diffusion by (a-d) the kick-out mechanism and (e-h) the dissociative mechanism (vacancy-assisted). In the kick-out mechanism, an atom diffuses interstitially (a) until it "kicks out" the shaded atom on a lattice site (b). The process repeats itself in (c) and (d). In the dissociative mechanism, the shaded atom initially on a lattice site (e) diffuses interstitially, creating a mobile vacancy (f). Eventually the atom will recombine with a vacancy (g) and settle on another lattice site (h). Adapted from N. A. Stolwijk, Defect Diffus. Forum **95**-**98,** 895 (1993).

CHAPTER 4

MORPHOLOGY, ELECTRICAL, AND THERMAL PROPERTIES OF GaAs:N LAYERS

4.1 Overview

This chapter describes investigations of the surface morphology, electrical, and thermal properties of as-grown, N-implanted, and N-implanted-plus-annealed GaAs layers for annealing temperatures of 800-900 ^{o}C. We begin with background information regarding buckling-driven delamination as well as ion-beam-synthesized nanocomposites and their application to novel electronics and energy conversion devices. Next, the details of the experimental procedures are described. The bulk of the chapter deals with investigations of the surface morphology of low- and high-temperature annealed GaAs:N surfaces. With increasing annealing temperature, the surface morphology transitions from circular to elongated features, presumably due to two distinct delamination behaviors. For low annealing temperatures, circular features are observed, and are presumably associated with the formation of subsurface gas bubbles, as discussed in Section 3.4. At high annealing temperatures, elongated features are also apparent. The elongated features are associated with buckling at the interface between the surface polycrystalline and nanocomposite layers. Finally,

measurements of the free carrier concentration, resistivity, and Seebeck coefficient of GaAs:N films for low- and high-temperature annealing are presented and discussed. Electrical measurements of GaAs(:N) suggest that the resistivity follows an log-log (power law) dependence on carrier concentration, in good agreement with literature reports of n-doped, MBE-grown GaAs films. Implantation and rapid-thermal annealing (RTA) decrease the carrier concentration and increase the resistivity, with a more significant effect for GaAsN:Te versus GaAsN:Si. Finally, we show that implantation plus RTA leads to an enhancement of the Seebeck coefficient with respect to that of GaAs.

4.2 Background

In this section, we describe the literature reports of importance for Chapter 4. First, we will address previous observations of buckling delamination in semiconductor materials. Then, we will discuss studies of III-V-material-based nanocomposites and their unique electrical and thermal properties.

4.2.1 Surface Buckle Formation

Thin-film surface buckling, i.e., periodic, out-of-plane displacement of a film,[1] is typically due to the relaxation of compressive stresses,[2] and has often been identified as a failure mechanism in surface coatings.[3,4] Film delamination via surface buckling, often termed "buckling-driven delamination," usually

requires the presence of a “weak” or low-toughness interface, such as that between a coating and substrate.[5] In terms of semiconductor materials, this ‘weak’ interface is often introduced artificially as a means to subsequently induce deformation. For example, in Si[6] and GaAs,[6,7] the chemical etching and transfer of crystalline films to pre-strained PDMS substrates led to the buckling delamination of the semiconductor films upon release of the pre-strain. In a similar fashion, wrinkled InGaAs membranes for nanochannels[8] were fabricated using a weak interface introduced by an etching layer between compressively-strained InGaAs layers and a GaAs substrate. For these and other device-driven applications, the mechanics of buckling have largely not been addressed.

4.2.2 Electrical and Thermal Properties of III-V-material-based Nanocomposites

In this section, we will discuss the unique electrical and thermal properties of materials with nano-scale inclusions (“nanocomposites”), with a focus on thermoelectric applications. For example, GaAsN nanocomposites have been fabricated by N ion implantation into GaAs followed by RTA.[9-11,34] For these materials, the focus has been largely on optical properties. For example, photoluminescence (PL)[11,12,34] and photomodulated reflectance (PR)[13,14] studies have shown an N-incorporation-induced reduction of the bandgap of GaAs. In addition, ballistic electron emission microscopy studies of GaAsN nanostructures[15] fabricated by implantation, pulsed-laser melting, and rapid-thermal annealing revealed a spatially-resolved decrease in Schottky barrier

height with increasing N, attributed to a decrease in the bandgap of the GaAsN alloy.[16] In another study, electrochemical capacitance voltage (ECV) measurements of S and N co-implanted GaAs revealed decreased donor activation efficiency in the vicinity of implantation-induced, nanoscale voids.[17] A related type of nanocomposite has been fabricated using MBE growth of ErAs/InGaAs nanoparticle superlattices. This nanocomposite was shown to exhibit enhanced Seebeck coefficient[18] and a factor-of-2 decrease in thermal conductivity[19] with respect to an InGaAs alloy.

For high-efficiency quantum-dot-based thermoelectrics, remaining challenges include maintaining electrical conductivity in tandem with low thermal conductivity[20] to maximize the thermoelectric figure-of-merit, *ZT* (Eq. 1.1). Particle-size effects are expected to influence both the electrical conductivity and thermal conductivity. For example, high densities of “ideal quantum dots” (particle sizes <10 nm) are expected to be optimal in terms of electrical transport, with the possibility of hopping conduction or tunneling between them. In terms of thermal transport, the sizes of nitride nanoparticles (~5 nm) possible using the ion-beam synthesis techniques demonstrated in this chapter are significantly smaller than the estimated phonon mean free path in GaAs (~100 nm).[21] Thus, nanocomposites with ultra-small particles are promising for thermoelectric devices with enhanced *ZT*.

4.3 Experimental Details

For this study, undoped, Si-doped, or Te-doped MBE-grown GaAs films were implanted with N^+ and subsequently subjected to RTA, as described in Section 2.2. The substrate temperature during implantation was -196 ^{o}C unless otherwise specified. Following implantation, some of the samples were subjected to RTA at 800, 850, or 900 ^{o}C for 30 seconds.

The layer surface morphologies were examined via plan-view and cross sectional scanning-electron microscopy (SEM) and atomic-force microscopy (AFM). SEM imaging was carried out in a FEI Nova Nanolab or Quanta 200 3D dual-beam FIB/SEM. Cross-sectional SEM images of the subsurface structure were obtained after focused ion beam (FIB) milling of trenches near the features of interest. Typical milling sequences consisted of the following voltage and current conditions: first, a 30 kV, ~1.2 nA “milling” step to remove ~5 μm of material, followed by a 10 kV, ~50 pA “polishing” step to minimize FIB-induced damage in the area to be imaged. AFM was performed with a Digital Instruments Nanoscope IIIA atomic force microscope in tapping mode, using etched Si tips, as described in Section 2.4. To determine the implantation-induced stresses, wafer curvature measurements were performed with a Dektak3 profilometer as described in Section 2.10.

For nano-structural investigations, transmission electron microscopy (TEM) and selected area electron diffraction (SAED) were carried out using a

JEOL 3011 high-resolution TEM operating at 300 kV. SAED patterns were obtained using a ~150 nm diameter aperture.

The electronic and thermal transport properties were examined using resistivity, Hall, and Seebeck coefficient measurements. To determine the resistivity, we assumed that carriers are contained within the n-doped, MBE-grown layer (~1 μm). Furthermore, in the analysis, we considered the carrier depletion widths at the free surface and at the interface between the MBE-grown film and the semi-insulating GaAs substrate.[22] In all cases, ~5x5 mm square samples were used for resistivity and Hall measurements and ~5x10 mm samples used for Seebeck measurements. Resistivity, Hall, and Seebeck measurements and analyses are described in detail in Section 2.9.

4.4 Surface Morphology of Annealed GaAs:N Layers

Fig. 4.1 presents plan-view SEM images of the surface morphology of N-implanted-plus-annealed GaAs layers for -196 and 300 °C implantation temperatures, and 800, 850, and 900 ºC (low, intermediate, and high temperature) RTA. For both implantation temperatures, the surface morphology after the low-temperature RTA consists of circular features, some of which appear to have exfoliated, as shown in Fig. 4.1(a,d). As the RTA temperature is increased, a transition from primarily circular features to a combination of circular and elongated features is apparent, as shown in Fig. 4.1(b,e) for intermediate-temperature RTA. Following high-temperature RTA (Fig. 4.1(c,f)), very few

circular features remain, and instead the surface primarily contains elongated features.

To elucidate the surface deformation processes, quantitative AFM measurements of as-implanted and implanted-plus-annealed GaAs:N surfaces were performed, as shown in Fig. 4.2. The as-implanted surface, shown in Fig. 4.2(a), appears featureless, exhibiting an rms roughness of ~3 nm. In contrast, following low-temperature and high-temperature RTA, micron-scale circular and elongated features are observed, as shown in Figs. 4.2(b) and 4.2(c). The circular features, which in some cases have already exfoliated, are likely associated with subsurface gas bubble formation, as described in Section 3.4. On the other hand, the appearance of elongated features suggests that a different deformation mechanism has been triggered during the high-temperature RTA.

The deformation behavior following low- and high-temperature RTA was further studied by cross-sectional SEM imaging, as shown in Figs. 4.3 and 4.4. Figure 4.3 shows SEM images of a trench-cut through both an intact and exfoliated circular surface feature following low-temperature RTA. The thickness of the intact circular feature is equal to the depth of the exfoliated circular feature, approximately 200 nm. This depth also coincides with the predicted depth of maximum nitrogen concentration as discussed in Section 3.4, suggesting that these voids have formed due to nitrogen gas accumulation. Therefore, we refer to these circular features as “blisters.”

Following high-temperature RTA, SEM images reveal elongated surface features, as shown in Fig 4.4. For the surfaces with elongated features, there appear to be two distinct depths at which voiding or delamination occurs. At ~200 nm below the surface, voids are apparent, similar to those shown in Fig. 4.3. However, an additional delamination has apparently occurred at a shallower depth, ~50 nm below the surface. The top delamination features, which we term "rumples," have a twisted shape similar to that of "telephone-cord" buckling,[23] suggesting a biaxial compressive stress state.[24-27] Interestingly, for RTA up to 900 ºC, exfoliation of the elongated features was not observed.

This shape of the rumples, shown in Figs. 4.2(c) and 4.4, indicates that this form of delamination is dominated by large residual compressive strains, possibly induced by implantation damage. The residual compressive strain, ε, is determined by comparing the apparent length of the delaminated layer (L) with the surface length of the non-delaminated subsurface layers (L_o), as shown in Fig. 4.4(c), as follows:

$$\varepsilon = (L-L_o)/L_o \tag{4.1}$$

Since the angle of observation for the SEM image is 52º, the values of L and L_0 are not exact. Nonetheless, for the rumple shown in Fig. 4.4(c), $L \approx 25$ μm and $L_0 \approx 20$ μm, leading to a strain of ~20%, much larger than the strain (< 2%) at which yield is typically observed in GaAs.[28] This large strain might be due to the relief of residual stress accumulated during ion implantation. Since the highest RTA temperature, 900 ºC, is within the temperature range for which creep has

been reported in GaAs,[29] it is likely that the implantation-induced stress is relieved via a creep-assisted mechanism.

Assuming that this system can be described by linear elasticity, we estimate the stress via Hooke's law. Using the *E* of crystalline GaAs (85.5 GPa) to approximate the value of *E* in the top polycrystalline layer, we find a residual compressive stress of 17 GPa.

To examine possible strain relaxation in the top polycrystalline layer, the Ga^+ FIB was used to remove "lines" of material from the surface, a process we refer to as "FIB line-cuts." FIB line-cuts were milled into the low-temperature-annealed and high-temperature-annealed layers, as shown in Figs. 4.5(a) and 4.5(b), respectively. The large rumple shown in Fig. 4.5(b) remains intact and does not "deflate," suggesting that these features are permanently (plastically) deformed, with a shape similar to that of a buckle. We note that this behavior is in contrast to that observed in buckled metallic films, for which the removal of compression applied via a mechanical stage[30] enabled the elastic relaxation of the surface to a from twisted buckles to straight buckles. Similarly, for diamond-like-carbon films on glass substrates, buckles appeared to elastically relax after FIB line-cuts[31] were milled across the width of the buckle.

4.5 N-implantation-induced Stress in GaAs:N

To characterize the implantation-induced stress, σ, we utilized curvature measurements in conjunction with Stoney's equation:[32]

$$\sigma = \frac{E_s}{1-\upsilon_s}\frac{h_s^2}{6h_f}\left(\frac{1}{R_f} - \frac{1}{R_i}\right) \tag{4.2}$$

where E_s and ν_s are the substrate Young's modulus and Poisson's ratio, h_s and h_f are the thicknesses of the substrate and film, and R_i and R_f are the radius of curvature of the wafer before and after implantation, respectively. Stoney's equation is considered valid for systems that exhibit linear and isotropic elasticity, with $h_f << h_s$, small strains (discussed later in this section), and a laterally uniform film stress.

Surface profilometry measurements were used to determine the wafer curvature. Specifically, the spatial dependence of the surface height was measured across 3 mm surface lengths for two samples before and after implantation. The details of these measurements as well as the analysis used to determine R are provided in Section 2.10. Example plots of height versus surface scan length for a GaAs wafer before and after N-implantation are shown in Fig. 4.6. The larger height difference across the scan length for the implanted wafer in comparison to that of the as-grown wafer indicates an implantation-induced decrease in radius of curvature, suggesting that implantation induces compressive stresses in the near-surface layers.

Table 4.1: Wafer curvature data for GaAs before and after N implantation. The radius of curvature, *R,* is determined from profilometry measurements of the spatial dependence of the surface height. The *R* values are averages (± standard deviation) of six surface scans for each sample. The significant decrease from R_i (before implantation) to R_f (after implantation) suggests a high implantation-induced residual stress.

Sample number	R_i (m)	R_f (m)
573C	21±3	1.5±0.1
725B	13±4	1.4±0.3

Using the values of R_i and R_f summarized in Table 4.1, E_s and ν_s of GaAs from Table D.1, and assuming that $h_s \approx 600$ μm and $h_f \approx 400$ nm (the predicted maximum depth of N implantation, as shown in Fig. 3.5), the implantation-induced stresses are estimated at ~11 GPa. This estimate is similar to the 17 GPa estimated from the SEM observations of surface deformation discussed in Section 4.4.

Our curvature measurements suggest an implantation-induced change in radius of curvature of approximately one order of magnitude, from ~10 m to ~1 m, as shown in Table 4.1. For such large changes in the radius of curvature, one concern is whether the small deflection requirement of linear elasticity has been violated. We demonstrate below that although the residual stress is large, the

deformation remains within the small deflection limit. Using the measured curvature, a normalized mismatch strain S may defined as:

$$S = K[1 + (1 - \upsilon_s)K^2] \qquad (4.3)$$

In this expression, K is a normalized curvature defined as $K = L^2/4Rh_s$, where L is a characteristic lateral dimension. Values of S < 0.3 are considered to be within the small deflection limit of linear elasticity.[33] In our case, for a typical sample edge length, 20 mm, a value of $S \approx 0.1$ is obtained from Eq. 4.3, well within the small deflection limit.

4.6 N-implantation-induced Stiffness Reduction in GaAs:N

The influence of implantation on the elastic response of the GaAs:N films was estimated using nanoindentation measurements, as described in Section 2.10. To limit the depth of the indentation measurements, displacement-driven positioning was used (thus leading to relatively noisy data). For similar displacements, the overall load for the implanted film was less than that of the as-grown film, indicating a reduced stiffness. This, in turn, suggests a reduction in the E of the film, following implantation.

For comparison purposes, we estimated E for the as-implanted GaAs:N layers based upon predicted elastic constants from the literature. Since prior TEM investigations revealed the essentially amorphous nature of the as-

implanted GaAs:N film,[34,35] we treat these films as amorphous GaAs. Molecular dynamics simulations predict elastic constants (c_{11} and c_{12}) of amorphous GaAs that are approximately 80% of their crystalline counterparts, as shown in Table D.3. Thus, using Eq. 4.4:

$$E = \frac{(c_{11} - c_{12})(c_{11} + 2c_{12})}{(c_{11} + c_{12})} \tag{4.4}$$

we estimate E = 69 GPa for amorphous GaAs, less than that reported for crystalline GaAs (85.5 GPa) and thus in qualitative agreement with the reduced stiffness observed by nanoindentation.

4.7 Structure of Annealed GaAs:N Layers

The subsurface structures of the low- and high-temperature-annealed layers are further explored by large-area TEM imaging, as shown in Figs. 4.8(a) and 4.8(b), respectively. In both cases, we observe three distinct layers: a top polycrystalline layer, a middle nanocomposite layer, and a crystalline GaAs near-substrate layer. In both cases, there appear to be two depths at which voiding or delamination occur, as discussed in section 4.4. At the top polycrystalline layer, ~50 nm below the surface, a delamination is apparent. In addition, at the interface between the near-substrate and nanocomposite layers, ~200 nm below the surface, voids are apparent. A comparison of Figs. 4.8(a) and 4.8(b)

suggests higher strains and therefore more significant deformation of the top polycrystalline layer for the high-temperature RTA film in comparison with the low-temperature RTA film.

The nanostructure of the high-temperature RTA film is shown in further detail in the TEM images in Figs. 4.9(a) and 4.9(b). The bright-field TEM micrograph presented in Fig. 4.9(a) reveals the top polycrystalline layer, the nanocomposite layer, and void formation between the nanocomposite and near-substrate layers. A corresponding {111} dark-field TEM micrograph of the same area as that shown in Fig. 4.9(a) is presented in Fig. 4.9(b). This image reveals bright features in both the nanocomposite and the top polycrystalline layers, presumably due to the formation of nanometer-size crystals in both layers. The top polycrystalline layer was further investigated using high-resolution TEM, as shown in Fig. 4.9(c). This region represents an area similar to that boxed in Fig. 4.9(a) and exhibits lattice fringes aligned in different directions, indicating the polycrystalline nature of this layer.

The composition of the nanocrystalline layer was elucidated by SAED from an area containing both the near-substrate layer and the nanocomposite layer, shown in Fig. 4.9(d). The SAED pattern reveals spots from the crystalline GaAs substrate as well as spotty rings associated with {101} and {110} wurtzite GaN, similar to previous investigations of 750-850 ^{o}C annealed layers.[34-36] Apparently, the larger surface deformation resulting from high-temperature RTA has not significantly influenced the nanostructure formation.

4.8 Electrical Properties of GaAs:N Films

To explore the electrical properties of GaAs(:N) layers, resistivity and Hall measurements were performed on MBE-grown ("as-grown"), N-implanted ("as-implanted"), and implanted-plus-RTA layers, for low- and high-temperature-RTA. As an approximation, we determined the resistivity values based on the total thickness of the doped layers, as described in Section 4.3. The resistivity of the as-grown samples follows a log-log (power law) dependence on carrier concentration, in good agreement with literature reports of n-doped, MBE-grown GaAs films, as shown in Fig. 4.11. Due to the relatively high resistivity of some implanted films and/or contacts, as well as the fragility of the blistered or rumpled surface layers, measurements of carrier concentration and resistivity from a nearly "complete" set consisting of all implantation and annealing conditions was only possible in a few cases. In this case, a "complete" set is defined as including as-grown, as-implanted, and implanted-plus-RTA layers for at least one RTA temperature (800 or 900 ºC), from one unique MBE-grown wafer. We will first compare nearly "complete" sets of data from Te-doped and Si-doped GaAs(:N) films and subsequently discuss the trends inferred from all data from GaAs(:N) layers.

The resistivity versus free carrier concentration of the n-doped GaAs(:N) layers is presented in Fig. 4.10(a), for those samples that comprise a nearly "complete" set. We note that for the Te-doped sample, resistivity could not be measured in the as-implanted film. Data from Yu *et al.*[37] (Jin *et al.*[38]) for MBE-

grown, Si-doped (and Te-doped) GaAs, for both as-grown and annealed layers is also plotted for comparison. For our GaAs(:N) layers, there are two sets of data: one Te-doped (denoted by filled markers) and two Si-doped (denoted by open and cross-hatched markers).

Following implantation, the carrier concentration decreases for both of the Si-doped layers, as shown by the dashed arrow from the circle to square-shaped marker in Fig. 4.10(a). This decrease in carrier concentration is likely due to carrier compensation by implantation-induced Frenkel (vacancy-interstitial) defects, as has been reported for O-, F-, and Ne-implanted GaAs.[39] We note that the corresponding resistivity of the Si-doped layers increases following implantation, from ~0.001 to ~0.004 and ~0.004 to ~0.03 Ω-cm, respectively.

Following RTA, the carrier concentration increases for all N-implanted, Si-doped GaAs:N layers. For these layers, *n* increases from ~10^{18} to ~$5x10^{18}$ cm^{-3} and ~10^{17} to ~$2x10^{17}$ cm^{-3}. For the Te-doped case, as-implanted data is not available. However, the combination of implantation *plus* RTA reduces the carrier concentration from ~$2x10^{18}$ (as-grown) to ~$3x10^{16}$ cm^{-3} (implanted-plus-800 ºC annealed). In contrast, the effect of implantation plus RTA on *n* for the Si-doped N-implanted layers is smaller, with a reduction from ~$6x10^{18}$ to ~$4x10^{18}$ cm^{-3} and $5x10^{17}$ to ~$2x10^{17}$ cm.$^{-3}$ For reference, we also compare the influence of RTA without implantation, using values from two reports in the literature. *n* for both the Si- and Te-doped layers from Jin *et al*. remain approximately constant at ~10^{18} cm^{-3}. In contrast, *n* for the Si-doped layer from Yu *et al*. decreases from ~$2x10^{19}$ to ~$6x10^{18}$ cm^{-3}. Thus, the effect of (implanted) N with annealing is to

decrease *n* for both Si- and Te-doped layers, although the decrease in *n* is much larger in the Te-doped case. Without implanted N, the effect of annealing appears to be dopant-insensitive, with similar decreases in *n* for both the Te- and Si-doped layers reported by Jin *et al.* Rather, the influence of RTA on *n* appears to depend on the magnitude of *n* before RTA. Following RTA, *n* decreases for samples with $n < 10^{19}$ cm^{-3}, whereas *n* remains constant for the most heavily-Si-doped sample reported by Yu *et al*.

We also consider the combined influence of implantation followed by RTA on the film resistivities. For the Si-doped GaAs:N layers, implantation plus RTA (circles to triangles) increases ρ of the two films from ~0.001 to ~0.01 Ω-cm and ~0.004 to ~0.04 Ω-cm. For the Te-doped GaAs:N layer, implantation plus RTA increases ρ from ~0.001 to ~0.1 Ω-cm, a much larger increase than that for the Si-doped case. In contrast, the resistivities of the MBE grown layers do not change appreciably with RTA. For Jin *et al*., ρ remains essentially constant at ~0.002 Ω-cm for both the Si-doped and Te-doped layers. Similarly, for the Si-doped layer reported by Yu *et al*., $\rho \approx 0.0006$ Ω-cm before and after RTA. Thus, the effect of implantation plus RTA is to increase ρ for both dopant types, although the increase in ρ for the Te-doped layer is significantly larger than that for Si-doping. For layers without implanted N, the influence of RTA on ρ is smaller, and nearly independent of dopant species (i.e., Si versus Te).

To examine the influence of implantation-induced lattice damage on the electrical properties, we consider literature values of ρ vs. *n* for MBE-grown GaAs:N layers in Fig. 4.10(b). It should be noted that for all layers in this plot, a

N concentration of ~1.5% is expected, whereas for the N-implanted layers in Fig. 4.10(a), the N concentration is predicted to exhibit an approximately Gaussian concentration profile, spanning a depth of ~400 nm beneath the surface, with a maximum N composition of ~50%, as estimated from Fig. 3.5. The "control" Te-doped and Si-doped GaAs films (without N) are again plotted for comparison, as well as MBE-grown GaAs:N layers, both as-grown and annealed. For the GaAs:N layers grown by Jin *et al.*, *n* increases from ~$2x10^{17}$ to ~$4x10^{17}$ cm^{-3} and ~$3x10^{17}$ to ~$4x10^{17}$ cm^{-3} for the Si-doped layers, and from ~$5x10^{17}$ to ~10^{18} cm^{-3} for the Te-doped layer, after RTA. In contrast, *n* for the GaAs:N layers grown by Yu *et al*. remains essentially constant at ~10^{19} $cm.^{-3}$ Similarly, the resistivities reported by Jin *et al*. decrease after RTA, from ~0.3 to ~0.05 Ω-cm and ~0.1 to ~0.05 Ω-cm for the Si-doped layers and from ~0.07 to ~0.02 Ω-cm for the Te-doped layer. In contrast, *ρ* values reported by Yu *et al*. remain constant at ~ 0.01 Ω-cm. Thus, the RTA-induced decrease in *n* and increase in *ρ* is significantly larger for the Te-doped, N-implanted GaAs layer than for the Si-doped GaAs:N layers (either N-implanted or MBE-grown).

Figure 4.11 presents the resistivity versus free carrier concentration for all n-doped GaAs(:N) films. Reported *ρ* versus *n* of MBE-grown, Si-doped GaAs layers from Chin *et al.*[40] are plotted for comparison, and are in good agreement with our as-grown data. Some general trends about the influence of implantation and RTA on *n* and *ρ* may be inferred from the data. For example, following RTA of the implanted layers, most of which possessed either film or contact resistances too large to measure, some of the conductivity was restored despite

the disordered crystalline structure of the nanocomposite (discussed in section 4.6). However, after implantation plus low-temperature RTA, the layers possess sufficiently low resistance to measure, and exhibit a factor of ~5 increase in ρ in comparison to the as-grown layers. To illustrate this ρ - n trend, in Fig. 4.11, dotted lines are drawn between the black diamonds and the black circles. In most cases, following high-temperature RTA, the resistivities of the layers could not be measured, similar to the case of the as-implanted layers discussed above. Their high resistivity is likely due to a combination of contact and film resistance, both of which may be influenced by the large surface deformation, as discussed in Section 4.4.

4.9 Seebeck Coefficient of GaAs:N Films

The thermal transport properties of the GaAs:N layers were investigated via measurements of the Seebeck coefficient S versus carrier concentration n, as shown in Fig. 4.12. S is defined as $\Delta V/\Delta T$ where ΔV is the measured voltage response for a temperature difference ΔT across the sample. For n-doped semiconductors, S is negative; for the following discussion, we will refer to the absolute value of S. In all cases, ΔT was ~1-5° with respect to the ambient temperature; thus, S represents the "room temperature" Seebeck coefficient. The measured Seebeck coefficients of the as-grown samples range from 100 and 500 μVK^{-1}, for n ranging from 10^{16} cm^{-3} to 10^{19} cm^{-3}. The measured values are similar to literature reports for n-doped GaAs, also shown in the plot.[41-43]

Following implantation, *S* could only be measured for the most heavily-doped implanted-plus-annealed layers, presumably due to the high resistivities for samples with carrier concentrations < 10^{18} cm^{-3}, as shown in Figs. 4.10 and 4.11. Interestingly, for the heavily-doped implanted-plus-annealed layers, the measured *S* is slightly enhanced in comparison to that of the as-grown films. The observed enhancement of *S* might be related to the predicted maxima of the power factor, $S^2\sigma$, and thermoelectric figure-of-merit, *ZT* (given in Eq. 1.1) for degenerate semiconductors with high *n* (10^{19}-10^{20} cm^{-3}).[44] Thus, the highly-doped films are promising for further studies of the thermal conductivity and resulting *ZT*, as will be discussed in Chapter 6.

4.10 Conclusions

The surface morphology and electrical and thermal properties of GaAs:N layers produced by N implantation of epitaxial GaAs with subsequent annealing at 800-900 °C were investigated. A transition in the morphology of the GaAs:N surfaces with annealing temperature was observed, independent of implantation temperature. At the lower annealing temperatures, circular blisters were predominately observed; at the higher annealing temperatures, elongated surface features associated with surface rumpling became dominant. Each surface feature was associated with its own distinct delamination depth. Following low-temperature RTA, delamination of the circular features occurred at the observed depth of cavities, suggesting that blistering was induced by

coalescence of N bubbles, as described in Section 3.4. However, following high-temperature RTA, delamination of the elongated surface rumples occurred at the interface between the near-surface polycrystalline and nanocomposite layers. The morphology of this delamination suggests that a different mechanism, buckling-driven delamination, is triggered in that case. In addition, large implantation-induced residual stresses are observed, and are apparently relieved by a combination of delamination and creep-assisted plastic deformation in the high-temperature RTA system.

The influence of implantation and RTA on the free carrier concentration, n, and resistivity, ρ, of GaAs:N(Si) and GaAs:N(Te) was examined. For GaAs(:N), ρ follows a log-log dependence on n, independent of the dopant species and RTA conditions. Following implantation plus RTA, decreased n and increased ρ were observed for both dopant types, with a more significant increase in ρ for the Te-doped GaAs:N layer. Finally, for the implanted plus RTA GaAs:N nanocomposite layers, the measured Seebeck coefficient is slightly enhanced in comparison to that of GaAs.

4.11 References

[1] H. Jiang, D.-Y. Khang, J. Song, Y. Sun, Y. Huang, and J. A. Rogers, Proc. Natl. Acad. Sci. USA **104**, 15607 (2007).

[2] M. D. Thouless, J. Vac. Sci. Technol. A **9**, 2510 (1991).

[3] H.-H. Yu and J. W. Hutchinson, Int. J. Fracture **113**, 39 (2002).

[4] P. Waters and A. A. Volinksy, Exp. Mech. **47** 163 (2007).

[5] J. W. Hutchinson, M. Y. He, and A. G. Evans, J. Mech. Phys. Solids **48**, 709 (2000).

[6] Y. Sun, W. M. Choi, H. Jiang, Y. Y. Huang, and J. A. Rogers, Nature Nanotech. **1**, 201 (2006).

[7] Y. Sun, V. Kumar, I. Adesida, and J. A. Rogers, Adv. Mater. **18**, 2857 (2006).

[8] A. Malachias, Y. Mei, R. K. Annabattula, C. Deneke, P. R. Onck, and O. G. Schmidt, ACS Nano **2**, 1715 (2008).

[9] S. Amine, G. Ben Assayag, C. Bonafos, B. de Mauduit, H. Hidriss, A. Claverie, Mater. Sci. Eng. B **93**, 10 (2002).

[10] X. W. Lin, M. Behar, R. Maltez, W. Swider, Z. Liliental-Weber, and J. Washburn, Appl. Phys. Lett. **67**, 2699 (1995).

[11] X. Weng, R. S. Goldman, V. Rotberg, N. Bataiev, and L. J. Brillson, Appl. Phys. Lett. **85**, 2774 (2004).

[12] W. Shan, K. M. Yu, W. Walukiewicz, J. W. Ager III, E. E. Haller, and M. C. Ridgway, Appl. Phys. Lett. **75**, 1410 (1999).

[13] K. M. Yu, Semicond. Sci. Technol. **17**, 785 (2002).

[14] K. M. Yu, W. Walukiewicz, M. A. Scarpulla, O. D. Dubon, J. Wu, J. Jasinski, Z. Lilliental-Weber, J. W. Beeman, M. R. Pillai, and M. J. Aziz, J. Appl. Phys. **94**, 1043 (2003).

[15] T. Kim, M. J. Aziz, and V. Narayanamurti, Appl. Phys. Lett. **93**, 102117 (2008).

[16] T. Kim, K. Alberi, O. D. Dubon, M. J. Aziz, and V. Narayanamurti, J. Appl. Phys. **104**, 113722 (2008).

[17] J. Jasinski, K. M. Yu, W. Walukiewicz, J. Washburn, and Z. Lilliental-Weber, Appl. Phys. Lett. **79**, 931 (2001).

[18] J. M. Zide, D. O. Klenov, S. Stemmer, A. C. Gossard, G. Zeng, J. E. Bowers, D. Vashaee, and A. Shakouri, Appl. Phys. Lett. **87**, 112102 (2005).

[19] W. Kim, J. Zide, A. Gossard, D. Klenov, S. Stemmer, A. Shakouri, and A. Majumdar, Phys. Rev. Lett. **96**, 045901 (2006).

[20] M. S. Dresselhaus, G. Chen, M. Y. Tang, R. Yang, H. Lee, D. Wang, Z. Ren, J.-P. Fleurial, and P. Gogna, Adv. Mater. **19**, 1043 (2007).

[21] G. Chen, *Nanoscale Energy Transport and Conversion*, (Oxford, New York, 2005), p. 290.

[22] A. Chandra, C. E. C. Wood, D. W. Woodard, and Lester F. Eastman, Solid-State Electron. **22**, 645 (1979).

[23] A. A. Volinsky, Mat. Res. Soc. Symp. Proc. **749**, W10.7.1 (2003).

[24] N. Matuda, S. Baba, and A. Kinbara, Thin Solid Films **81**, 301 (1981).

[25] M. Thouless, J. Amer. Ceram. Soc. **76**, 2936 (1993).

[26] G. Gille, and B. Rau, Thin Solid Films **120**, 109 (1984).

[27] D. He, W. Cheng, J. Qin, J. Yue, E. Xie, and G. Chen, Appl Surf. Sci. **191**, 338 (2002).

[28] S. Wang and P. Pirouz, Acta Mater. **55**, 5500 (2007).

[29] R. K. Willardson, K. T. Faber, and K.J. Malloy, *The Mechanical Properties of Semiconductors,* (Academic Press, New York, 1992), p. 193.

[30] C. Coupeau, J. F. Naud, F. Cleymand, P. Goudeau, and J. Grillhé, Thin Solid Films **353**, 194 (1999).

[31] M. W. Moon, H. M. Jensen, J. W. Hutchinson, K. H. Oh, and A. G. Evans, J. Mech. Phys. Solids **50**, 2355 (2002).

[32] G. G. Stoney, Proc. R. Soc. **9**, 172 (1909).

[33] L. B. Freund, J. Mech. Phys. Solids **48**, 1159 (2000).

[34] X. Weng, S. J. Clarke, W. Ye, S. Kumar, R. S. Goldman, A. Daniel, R. Clarke, J. Holt, J. Sipowska, A. Francis, and V. Rotberg, J. Appl. Phys. **92**, 4012 (2002).

[35] X. Weng, W. Ye, S. J. Clarke, R. S. Goldman, V. Rotberg, A. Daniel, and R. Clarke. J. Appl. Phys. **97**, 064301 (2005).

[36] X. Weng, W. Ye, R. S. Goldman, and J. C. Mabon, J. Vac. Sci. Technol. B **22**, 989 (2004).

[37] K. M. Yu, W. Walukiewicz, J. Wu, D. E. Mars, D. R. Chamberlin, M. A. Scarpulla, O. D. Dubon, and J. F. Geisz, Nat. Mater. **1**, 185 (2002).

[38] Y. Jin, Y. He, H. Cheng, R. M. Jock, T. Dannecker, M. Reason, A. M. Mintairov, C. Kurdak, J. L. Merz, and R. S. Goldman, Appl. Phys. Lett. **95**, 092109 (2009).

[39] K. T. Short and S. J. Pearton, J. Electrochem. Soc. **135**, 2835 (1988).

[40] V. W. L. Chin, T. Osotchan, M. R. Vaughan, T. L. Tansley, G. J. Griffiths, Z. Kachwalla, J. Electron. Mater. **22**, 1317 (1993).

[41] G. Homm, P. J. Klar, J. Teubert, and W. Heimbrodt, Appl. Phys. Lett. **93**, 042107 (2008).

[42] N. A. Mordovets, A. Y. Shul'man, and I. N. Kotel'nikov, Semicond. Sci. Technol. **19**, S308 (2004).

[43] S. K. Sutradhar and D. Chattopdhyay, J. Phys. C **12**, 1693 (1979).

[44] G. J. Snyder and E. S. Toberer, Nat. Mater. **7**, 105 (2008).

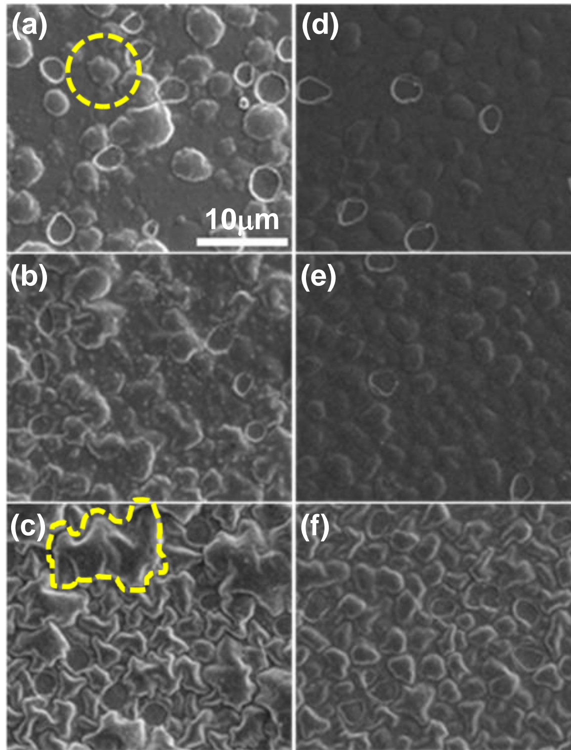

Fig. 4.1 SEM images of implanted-plus-annealed samples for implantation temperatures of -196 °C (first column) and 300 °C (second column), and annealing temperatures of (a,d) 800, (b,e) 850, and (c,f) 900 °C. For both implant temperatures, the 800 °C annealed surfaces consist of circular features: blisters and craters (popped blisters). At higher annealing temperatures, the surface features transition from circular to predominantly elongated features at 900 °C (highlighted with a dashed line).

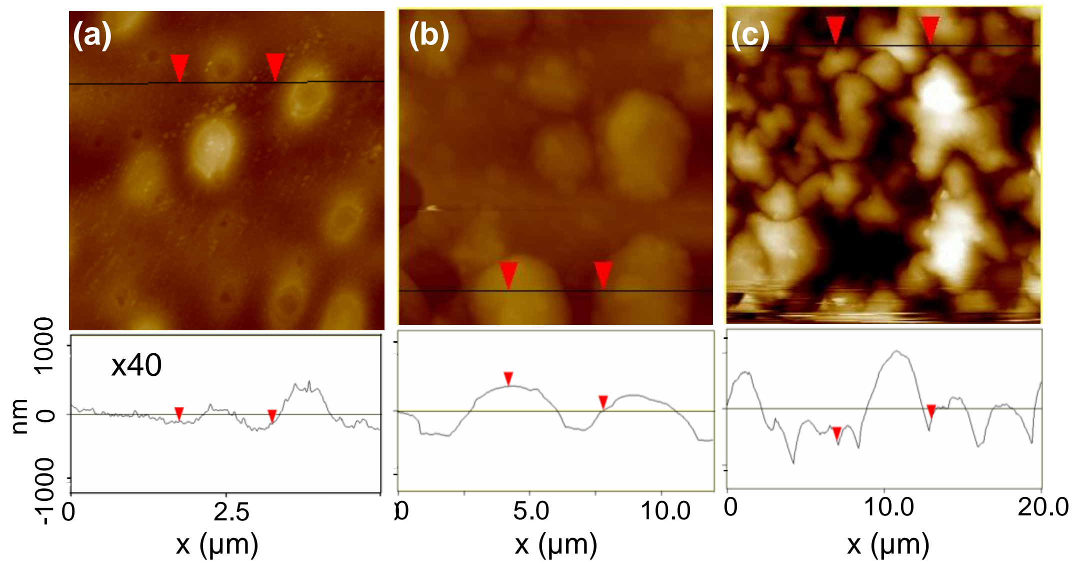

Fig. 4.2 AFM surface profiles of (a) as-implanted, (b) implanted plus 800 °C annealed, and (c) implanted plus 900 °C annealed GaAs:N surfaces. In the as-implanted case, a relatively small surface roughness is observed (x40 scale). For the 800 °C annealed surface, circular blisters are observed, and for the 900 °C annealed surface, larger surface rumples are apparent.

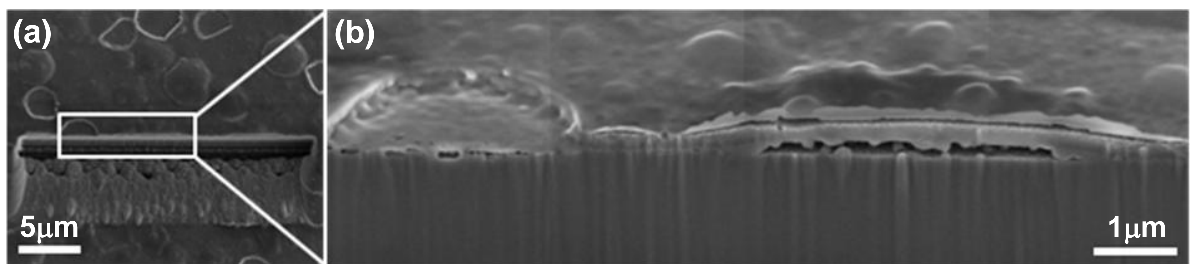

Fig. 4.3 (a) Plan view SEM image of an implanted plus 800 °C annealed film with circular features. FIB material removal was performed to image a crater and blister in cross-section in (b). Both features appear to delaminate at a depth of ~200 nm, in agreement with the simulated N ion range, suggesting that the circular features result from gas pressure-induced blistering.

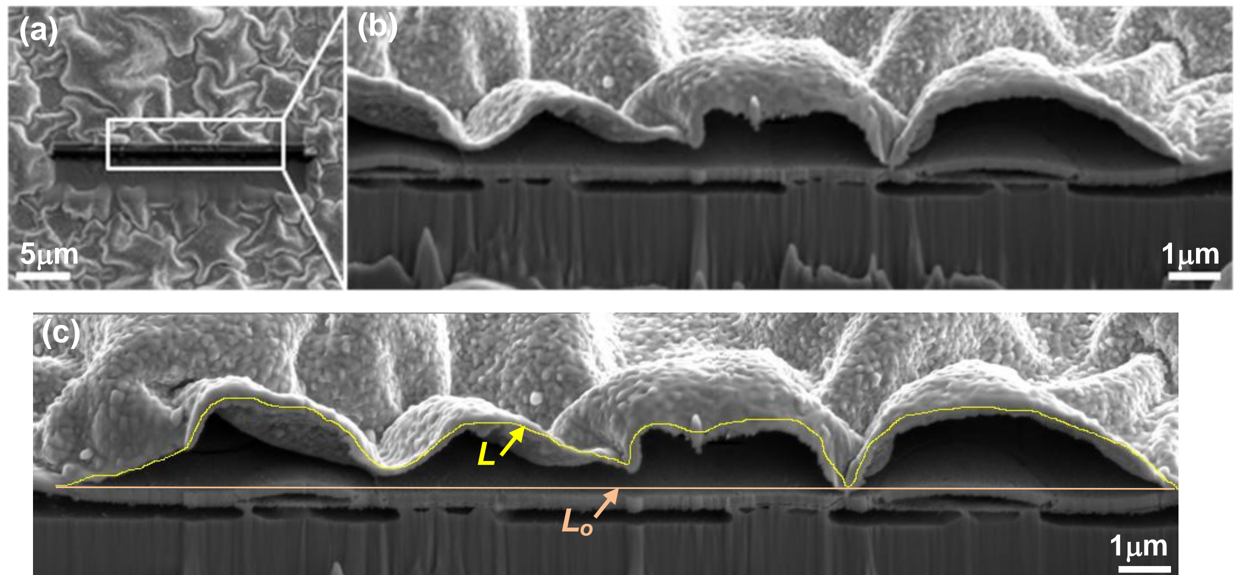

Fig. 4.4 (a) Plan view SEM image of an implanted plus 900 °C annealed film with elongated features. FIB material removal was performed to image the sub-surface structure in cross-section in (b), revealing two distinct delamination depths corresponding to the interface between the near-surface crystalline and nanocomposite layers, as well as a deeper delamination at the bubble layer. The strain in the top layer is estimated by $(L-L_o)/L_o$, where L_o is the apparent length of the deformed top layer and L is the un-deformed surface length, as estimated from line-traces shown in (c).

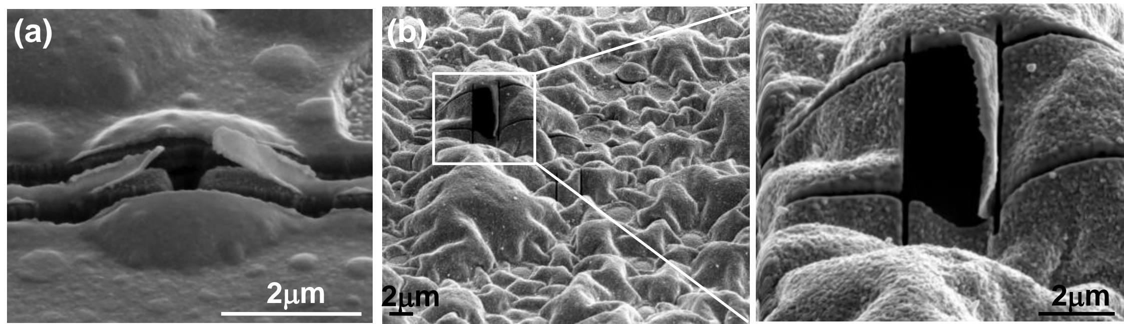

Fig. 4.5 SEM images of implanted plus (a) 800 °C and (b) 900 °C annealed samples after FIB line cuts were milled into a (a) circular and (b) elongated feature. In both cases, the top layer of the sample exhibits no apparent relaxation, suggesting permanent (plastic) deformation.

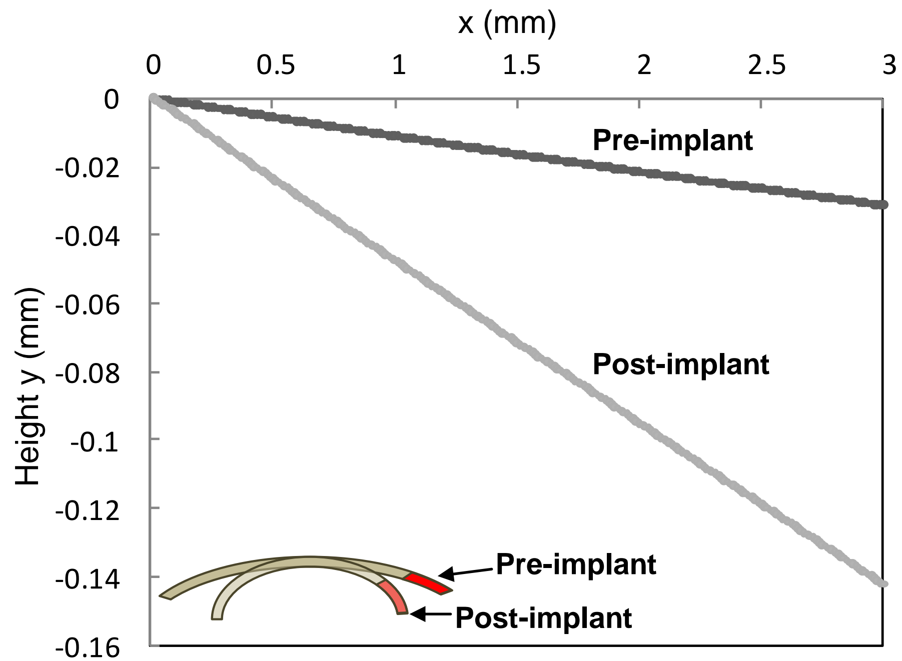

Fig. 4.6 Profilometer measurements across the surface a GaAs wafer before and after N-implantation. In both cases, a gradient in surface height is observed due to both intrinsic curvature and residual stresses, as shown schematically in the inset. The reduction in the surface height gradient (and consequently radius of curvature) is likely due to an increase in near-surface compressive stresses due to ion implantation.

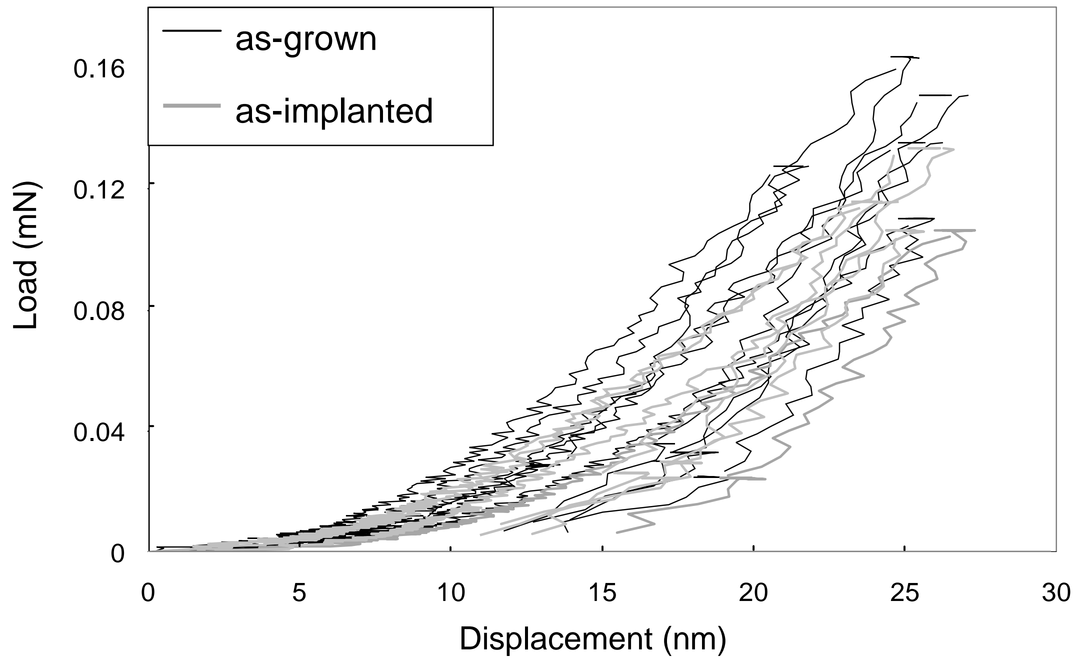

Fig. 4.7 Load versus displacement measured by nanoindentation of as-grown and N-implanted GaAs films. Larger displacements are observed for implanted films versus as-grown films for similar loads, suggesting reduced stiffness of the implanted films.

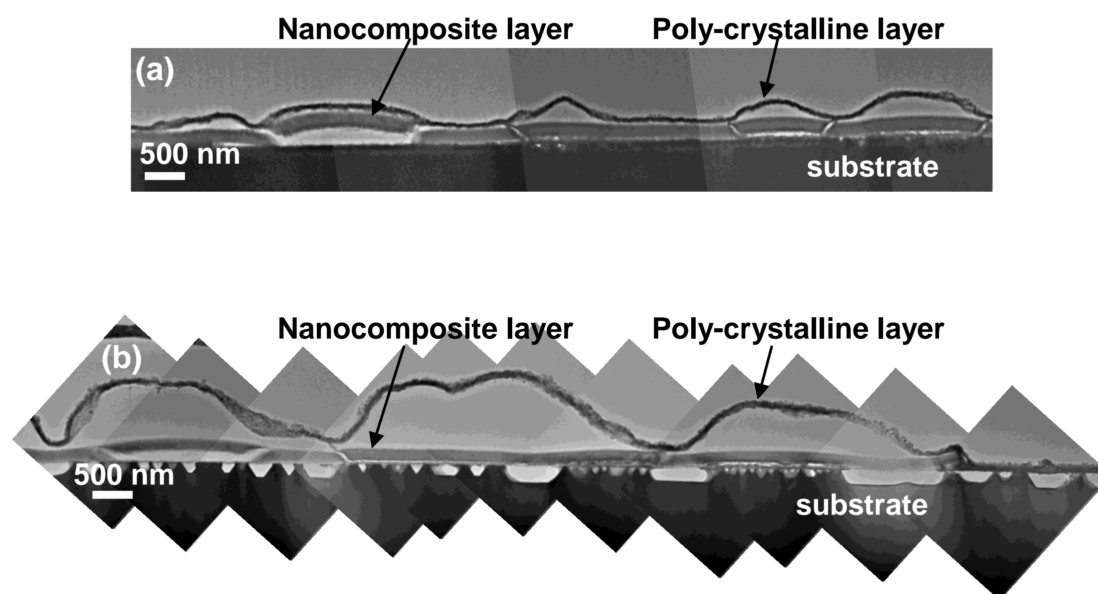

Fig. 4.8 Large-area cross-sectional TEM of an (a) implanted plus 800 °C annealed film and (b) implanted plus 900 °C annealed film, showing the relatively large deformation of the top polycrystalline layer in (b).

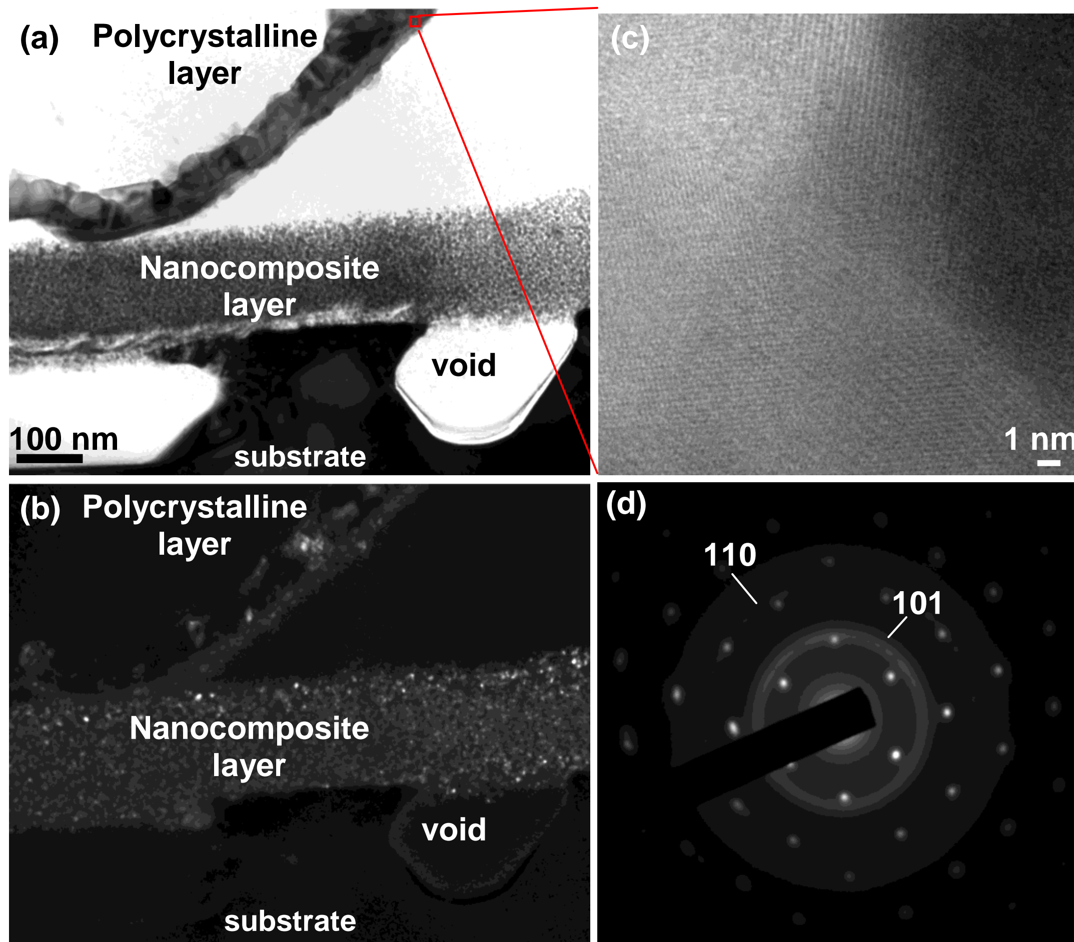

Fig. 4.9 (a) Bright-field and (b) {111} dark-field TEM images of implanted plus 900 ^{o}C annealed GaAs:N layers. In (a), three distinct layers are apparent, including the delaminating polycrystalline layer, the nanocomposite layer, and the GaAs near-substrate layers. The nanocrystalline nature of the middle layer is shown by the dark-field image in (b). In (c), HRTEM of the top layer reveals its polycrystalline structure, as observed by the varying directions of lattice fringes. SAED of an area including the nanocomposite layer and near-substrate layers is shown in (d), revealing both crystalline diffraction spots from the substrate as well as spotty rings associated with {101} and {110} wurtzite GaN, as labeled in the pattern.

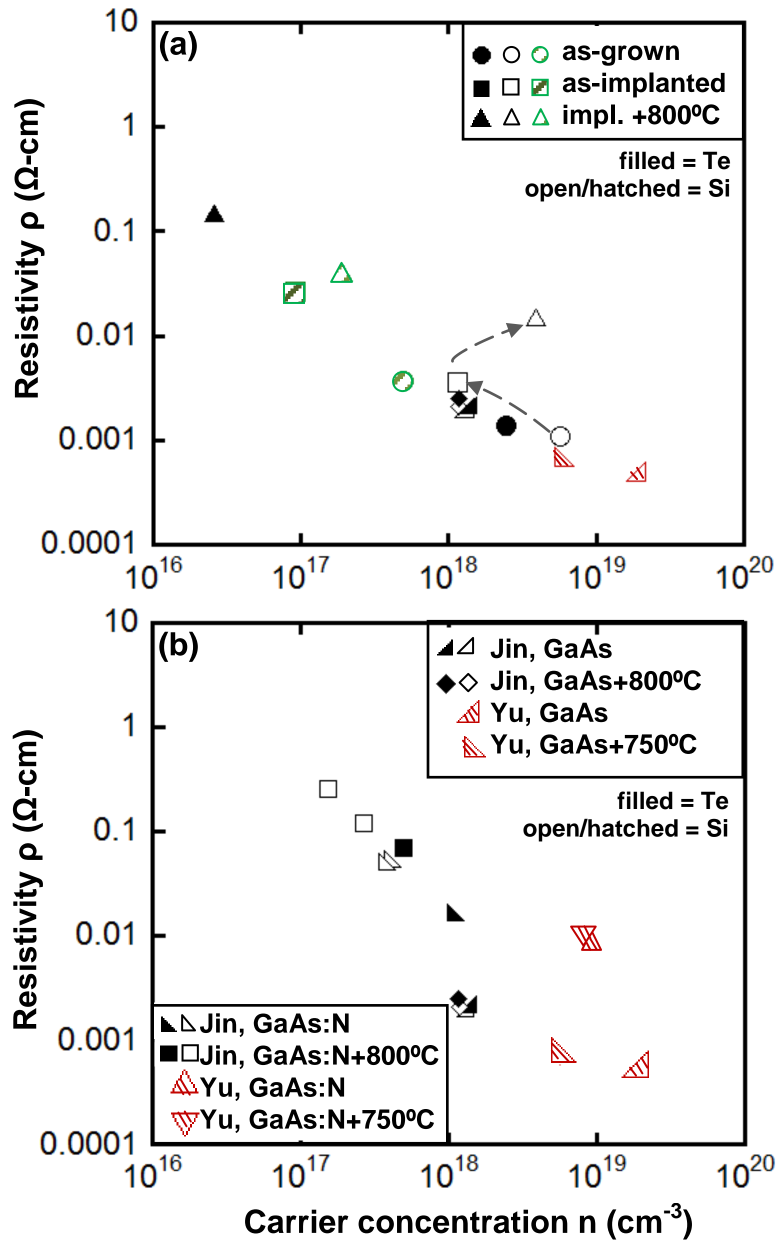

Fig. 4.10 Resistivity versus free carrier concentration of GaAs(:N) layers for (a) implanted layers and (b) MBE-grown layers from Jin *et al*. (Ref. 38) and Yu *et al*. (Ref. 37), illustrating the more pronounced effect of annealing on n and ρ of Te-doped, N-implanted GaAs layers versus MBE-grown Te-doped or Si-doped GaAs layers. As a guide to the eye, an example of the sequence of processing steps (implantation, followed by annealing) is indicated by an arrow for a Si-doped sample

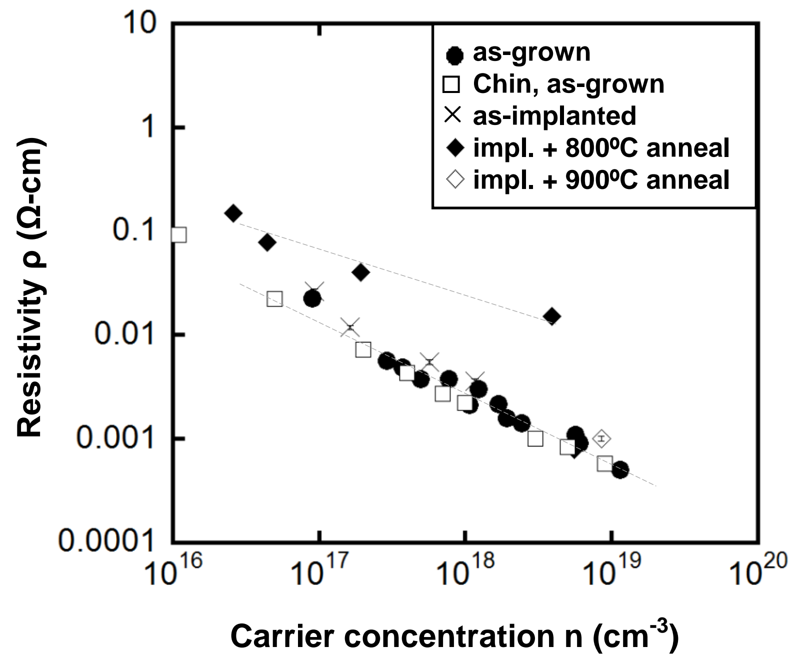

Fig. 4.11 Resistivity versus free carrier concentration for all n-doped GaAs(:N) films. Dotted lines are drawn as a guide to the eye, to illustrate the increase in resistivity for implanted-plus-800 ºC annealed layers versus as-grown layers. For comparsion, resistivities of MBE-grown layers from Chin *et al.* (Ref. 40) are shown.

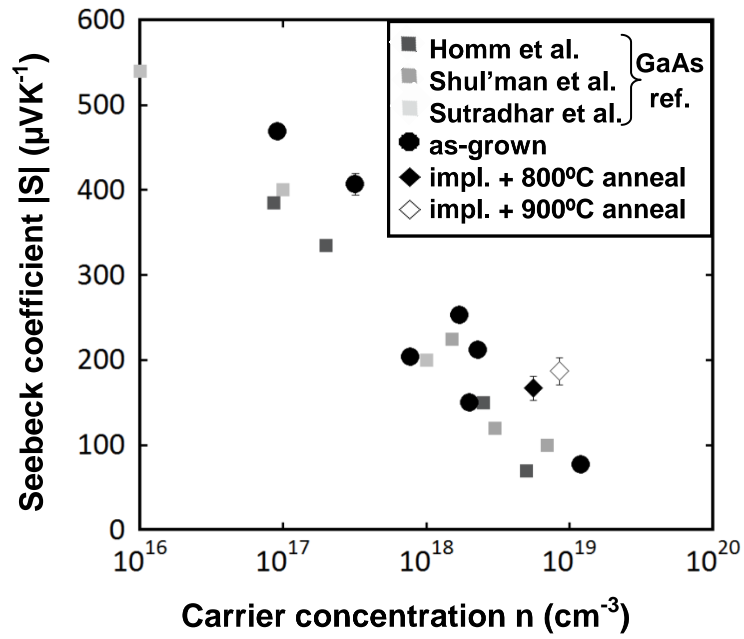

Fig. 4.12 Seebeck coefficient versus carrier concentration for as-grown, implanted plus 800 ºC annealed, and implanted plus 900 ºC annealed n-doped GaAs:N films. For comparison, values from Refs. 41-43 for n-doped GaAs are shown.

CHAPTER 5

ION-CUT-SYNTHESIS OF GaAs:N NANOCOMPOSITE LAYERS

5.1 Overview

In this chapter, we discuss the development and demonstration of a new technique for the simultaneous nanostructuring and layer transfer of a GaAs:N film, termed "ion-cut-synthesis." Ion-cut-synthesis is accomplished via N-ion implantation in GaAs, followed by wafer bonding and rapid-thermal annealing. Due to the low ion-matrix diffusivity of GaAs:N, high-temperature annealing induces the formation of both nanocrystals and gas bubbles, thereby enabling simultaneous nanostructuring and layer transfer of GaAs:N films.

The chapter begins with a review of semiconductor materials integration strategies, including the ion-cut process. In addition, efforts to date to achieve combined transfer and film patterning will be presented. Next, we describe the experimental details for our investigations. The bulk of this chapter is devoted to our work in identifying suitable alternative substrates and bonding materials for the successful demonstration of ion-cut-synthesis. In particular, the critical role of thermal expansion coefficient matching on the achievement of ion-cut-synthesis is described.

5.2 Background

In this section, we present a review of semiconductor thin-film materials integration, including approaches that involve wafer bonding. This is followed by a discussion of the ion-cut process, in which wafer bonding is coupled with light-ion-implantation and annealing to achieve the transfer of thin films. In the final part of this section, we will discuss attempts to date to achieve transfer of patterned films by ion-cut, as well as background work towards the achievement of the ion-cut-synthesis process for the simultaneous synthesis and transfer of a nanostructured film.

5.2.1 Semiconductor Thin-film Materials Integration by Wafer Bonding

For several GaAs materials integration applications, thermal, electrical, and/or fiscal requirements make it necessary to explore alternative substrates such as other semiconductors, glasses, or ceramics. In particular, ceramic substrates are attractive in terms of price, and some can provide a combination of electrical insulation and high thermal conductivity for heat dissipation in high-power/high-frequency applications. Examples of III-V/ceramic materials integration via wafer bonding include AlGaAs/GaAs-heterostructure-based heterojunction bipolar transistors on AlN and diamond substrates fabricated by a bond-and-etch-back technique.[1] Similarly, low-temperature-grown GaAs

microswitches have been transferred to single-crystal Al_2O_3 substrates via epitaxial lift-off (ELO).[2] However, in many cases, these bonding techniques require the removal of the parent GaAs substrate. Thus, in order to save material, techniques for the transfer of a thin layer that preserve the parent substrate for further processing are desirable. One such technique is the ion-cut process, for which ion-implantation-induced gas pressure is used to transfer a thin film, as discussed in the next section.

5.2.2 Ion-cut

Over the past decade, the “ion-cut” or “smart-cut” process[3] has emerged as a promising approach to heterogeneous materials integration. The ion-cut process involves high-energy ion implantation into a sacrificial substrate which is then bonded to another substrate. Subsequent thermal annealing leads to the formation and coalescence of gas bubbles, resulting in fracture of the original substrate. This surface layer remains bonded to the new substrate, which we will refer to in general as a “receiver substrate,” and the original substrate may be re-used for additional thin film processing. Given the relatively high cost of GaAs substrates, the ability to recycle the original GaAs wafer is a distinct advantage over all of the wafer bonding techniques described in the previous section, for which subsequent removal or mechanical thinning of the original GaAs substrate is required.

Ion-cut was first demonstrated[3] for silicon-on-insulator technology as a means of transferring a crystalline silicon layer onto an amorphous insulating oxide layer. To date, the ion-cut technique has been expanded to include the transfer of several semiconductor and oxide layers to alternative receiver substrates.[4-12] For heterogeneous GaAs integration, the sole focus of ion-cut has been for the transfer of crystalline GaAs layers to Si.[13-18]

In all of these cases, light-ion (H^+ and/or He^+) implantation was used to accomplish ion-cut of GaAs. To our knowledge, the use of N implantation for layer transfer has not yet been explored. In addition, as discussed in Section 3.6, the implantation of N in GaAs is advantageous for ion-cut due to the low ion-matrix diffusivity and the apparent stability of bubble formation across a wide range of processing temperatures (and thus, presumably more uniform layer transfer) in comparison to higher-diffusivity systems such as GaAs:H.

5.2.3 Progress Toward Patterned Layer Transfer by Ion-cut

In general, the fabrication of a patterned device or structured film by ion-cut typically entails several processing steps subsequent to layer transfer. For example, nanopatterned Si surfaces have been created by ion-cut followed by a multi-step process including twist-bonding and chemical etching.[19] The transfer of patterned “islands” has been demonstrated for silicon-on-insulator[20] and patterned exfoliation (but not patterned transfer) has been achieved for InP and GaAs.[21] In these cases, localized exfoliation is accomplished by either the

deposition of a photoresist layer or the placement of a mesh grid on the sample surface prior to implantation. These masking techniques are limited in terms of the achievable spatial resolution as well as the additional processing steps required to remove the masking grid or photoresist layer. The transfer of Si-based device structures fabricated prior to ion-cut has also been demonstrated,[22] but many complications must be accounted for. For example, to ensure a uniform depth distribution of implanted ions (and consequently, uniform splitting) the device components must comprise materials in which the implanted ion has similar stopping powers.

To our knowledge, simultaneous patterning and layer transfer via ion-cut alone has not been accomplished. It is likely that both the precipitation of a new phase and bubble formation is not possible in high-diffusivity systems such as Si:H and GaAs:H. For example, in H-implanted Si, nanostructure and bubble formation have been observed to occur separately, but not simultaneously. In this case, high-dose ($1 - 3 \times 10^{17}$ cm^{-2}) H implantation and high-temperature (600 - 800 ºC) annealing leads to the formation of Si nanocrystals within an amorphous Si layer.[23] Bubble formation and ion-cut have been reported to occur only within lower dose[24] ($2 \times 10^{16} - 1 \times 10^{17}$ cm^{-2}) and temperature[25] (400 - 600 ºC) windows. The upper temperature bound observed for blister formation[26] and layer transfer[27] in high-diffusivity, light-ion-implanted systems is likely due to the out-diffusion of the implanted ions. In turn, this out-diffusion would prevent the high-temperature precipitation of a new phase.

In contrast, due to the low ion-matrix diffusivity of GaAs:N, precipitation of both nitrogen gas bubbles and nitride nanocrystals has been observed.[28] Based upon these observations, Weng *et al.*[29] proposed the ion-cut-synthesis technique for simultaneous nanostructure synthesis and layer transfer in N-implanted, bonded, and annealed GaAs. If the high-temperature-annealing induced layer splitting is caused by gas-bubble-induced pressure rather than thermal mismatch stress-induced delamination, then ion-cut-synthesis would be possible by the mechanism shown in Fig. 5.1. In this case, a nitrogen-implanted GaAs substrate is bonded to a receiver substrate using a spin-on glass (SOG) intermediate layer (Fig. 5.1(a)). A subsequent rapid-thermal-annealing (RTA) step would lead to both the precipitation of nanocrystals as well as the nitrogen-gas-pressure-induced splitting of the nanocomposite layer, as shown schematically in Fig. 5.1(b).

5.3 Experimental Procedures

This section describes the experimental procedures used to fabricate and characterize GaAs:N layers transferred by ion-cut-synthesis. First, the glass-mediated bonding procedures and thermal annealing steps for ion-cut-synthesis are outlined. This is followed by a description of the blade test technique used to estimate the interfacial toughness of these bonding layers. Finally, the electron and scanning probe microscopy techniques used to characterize the transferred GaAs:N layers are presented.

In all cases, N^+ implantation procedures were carried out as described in Section 2.2, with a substrate implantation temperature of -196 ºC unless otherwise noted. For layer transfer, the ~600 µm thick GaAs:N samples were bonded to ~100 µm thick Al_2O_3 or AlN substrates (both polycrystalline) with a commercial methylsilsesquioxane (MSSQ) SOG (Filmtronics 550F or FG65) or a MTMS-BTSE (methyltrimethoxysilane - 1,2-bis(triethoxysilyl)ethane) spin-on glass prepared at NIST,[30] as described in Section 2.6. In all cases, ~1 mL of SOG was deposited on the surface of the ceramic substrate using a syringe; in the case of the MTMS-BTSE SOG, a Teflon syringe filter (0.45 µm pore size) was used during deposition. Following deposition, the SOG films were planarized by high-speed rotation (~1000 rpm) in a Laurell 4NPP-Lite spin coater. Film thicknesses were varied by changing the rotational speed for planarization. In the case of the MSSQ films discussed in this chapter (FG65), the "thick" ~1000 nm film was achieved by spin-coating the FG65 solution at 3500 rpm for 30 seconds. To achieve the "thin" ~200 nm film, the FG65 solution was diluted by 25% with ethyl acetate and spun at 3000 rpm for 20 seconds. 200 nm thick MTMS-BTSE films were achieved by spin-coating at 1200 rpm for 15 seconds.

Prior to bonding, both the Al_2O_3 and AlN ceramic substrates were polished to a mirror-like finish using SiC polishing papers, as described in Section 2.7. All sample surfaces were cleaned with a sequence of deionized water, acetone, and methanol, followed by a final deionized water rinse. Subsequent bonding steps were performed at room temperature, followed by RTA in N_2 gas for 30 sec at either 800 °C or 900 °C to induce ion-cut-synthesis. The general bonding

procedure is outlined in Section 2.6, and details for each experiment are provided in Appendix B.

To quantify the interfacial toughness of the glass-bonded interfaces, blade test experiments were performed. Toughness is a measure of the energy required to fracture a unit area of interface (in Jm^{-2}). Typically, quantitative measurements of interfacial toughness involve an analysis of the critical values of the crack-tip moment, axial load, and/or transverse shear load required to propagate an interface crack. Due to issues such as crack-tip blunting, techniques which rely upon controlled crack-opening displacement and arrest, such as the blade test, are often preferable to those which determine critical loads for crack initiation.[31,32] For example, in the blade test, shown in Fig. 5.2(a), a blade (or wedge) of known thickness is inserted into the interface, which is clamped shut. Once the wedge is stationary, such that there are no applied torques, the clamping pressure across the interface is released. As shown in Figs. 5.2(b) and (c), the interface crack will advance and consequently come to rest at some distance ahead of the wedge. A measure of the final crack length then allows the toughness of the interface to be computed. If the crack length is more than about ten times the thickness of the wafer, which is typically true in our case, the transverse shear load contribution can be neglected. In the absence of any other loading effects, such as thermal expansion and/or curvature mismatch, the toughness of the interface, Γ, is related to the arrested crack length, a, thickness of the wedge, w, and the thicknesses, h_1 and h_2, and moduli, E_1 and E_2, of the two wafers:[33]

$$\Gamma = [3w^2 E_1 E_2 h_1^3 h_2^3]/[8a^4(E_1 h_1^3 + E_2 h_2^3)] \quad (5.1)$$

As with most techniques to measure interfacial toughness, the blade test relies upon accurate determination of the crack tip position. A special microscope system with an infrared (IR) sensitive CCD camera was set up for this purpose, as shown in Fig. 5.3. Since GaAs (and Si) are transparent to infrared radiation, the bonded interface and crack tip position were thus easily monitored.

To examine the morphology of transferred GaAs films on the ceramic substrates, we utilized low-vacuum-mode scanning electron microscopy (SEM) as well as atomic force microscopy (AFM), described in Sections 2.3.1 and 2.4, respectively. The structures of the transferred films were examined by transmission electron microscopy (TEM), using a JEOL 3011 HRTEM operating at 300 kV. Due to the localized nature of the transfer, as well as the multilayered structure of the transferred films, a focused ion beam (FIB) lift-out technique was utilized to fabricate cross-sectional TEM specimens, as described in detail in Appendix C. In each case, a section of transferred layer ~2 x 15 μm in area was selected for lift out, and Pt layers were deposited on this area to protect the near-surface nanostructured layers from normal-incidence ion-beam damage. A ~200 nm thick Pt layer was deposited first by electron-beam-assisted deposition (at a voltage and current of 5 kV and 1.6 nA), followed by a ~1000 nm thick Pt layer deposited by ion-beam-assisted deposition at 10 kV and 0.12 - 0.21 nA. The surrounding area was subsequently Ga^+ ion milled at 30 kV, 5.0 nA, followed by

a Ga+ ion "polishing" step at 20 kV, 0.38 nA. Final Ga+ ion polishing of the area to be examined by TEM was performed at 10 kV, 23 - 50 pA.

5.4 Bonding and Alternative Substrates

In this section, we describe our work identifying suitable alternative substrates and bonding layers to achieve ion-cut-synthesis. In particular, the substrate selection process and mechanics analysis used to realize simultaneous nanostructuring and layer transfer is described.

Spin-on glass (SOG) has emerged as a versatile bonding agent due to its variable thickness, mechanical properties, and thermal properties. Compared with other glass-layer deposition methods, including chemical vapor deposition[34] and e-beam evaporation,[35] the SOG processing steps are relatively simple, consisting of material deposition (e.g., via an eye dropper), spin-coating, and low-temperature curing. Examples of SOG-bonded structures include GaInAs-based vertical-cavity surface-emitting lasers (VCSEL) on silicon substrates[36] and layer transfer of GaAs to Si by ion-cut,[15,37] for which processing temperatures are relatively low (< 400 °C). However, ion-cut-synthesis requires RTA at > 750 °C. Therefore, alternative bonding layers and substrates need to be identified.

In Sections 5.4.1 and 5.4.2, we will describe the selection processes for SOG bonding layers and substrates suitable for high-temperature, SOG-mediated wafer bonding. First, in Section 5.4.1, the bonding problem is analyzed for the initial bonding step of the implanted GaAs wafer to a receiver substrate,

neglecting the thickness of the SOG layer. Next, in Section 5.4.2, the bonding problem is analyzed immediately following the high-temperature annealing step, in which case, much of the original substrate has been removed such that the SOG layer thickness is on the order of the transferred GaAs:N film thickness. We show that the thickness and thermal expansion coefficient of the SOG has a significant impact on the morphology of the transferred, nanostructured film.

5.4.1 Materials Selection: Substrates for Layer Transfer

For ion-cut-synthesis, several possible semiconductor and ceramic receiver substrates were considered. In this section, we will discuss the materials selection process first in terms of thermal expansion coefficient (TEC) matching and its impact on the driving force for delamination. Finally, within the subset of the materials identified for optimum TEC-matching, these candidate materials are also discussed in terms of their thermal conductivity, which should be maximized for applications in which thermal management issues are critical.

For applications requiring high temperature processing such as ion-cut-synthesis, the integration of GaAs with alternative substrates is limited by the differences in TEC with respect to GaAs, leading to thermal-mismatch-induced stresses at high temperatures. The temperature-dependence of the TEC for various semiconductor and ceramic materials in the temperature range of 25 to 750 ºC is presented in Fig. 5.4(a).[38-45] In this temperature range, the TECs of polycrystalline Al_2O_3 and spinel are most closely matched to those of GaAs. All

of the others, including single-crystal Si and SiC, and polycrystalline AlN and Si_3N_4, possess TECs much lower than those of GaAs.

To identify the most promising candidates for receiver substrates, the driving force for delamination of GaAs/receiver substrate pairs was calculated and compared with the estimated toughness of glass bonding layers. This driving force for delamination, or energy release rate, *G*, is shown in Fig. 5.5 for several materials combinations. When the mismatch in TEC is minimized, *G* is minimized. For this calculation, the bonding layer is neglected, as the SOG thickness (*O*(100 nm)) is much less than those of the substrates (*O*(100 μm)). Thus, the bonding layer is only included in the model in terms of its interfacial toughness. In this case, the "bonding temperature" is defined as the temperature at which the strain due to thermal expansion mismatch between the substrates is zero. In the calculation, we assume substrate thicknesses of 300 μm. In addition, both the elastic moduli and differences in thermal expansion coefficient with respect to GaAs ($TEC_{GaAs} - TEC_{Ceramic}$) were approximated by an average over the temperature range of 25 °C to 750 °C.[62-68] These energy release rate (*G*) values were then compared with the measured toughness (Γ) of the SOG bonding agents used, where failure is defined at a critical value of *G* ($G_c = \Gamma$). Using a blade test technique, (described in section 5.3) we estimated an interfacial toughness value of ~1.2 Jm^{-2} for the MSSQ SOG, similar to previously reported values for GaAs/SOG/Si.[46] In comparison, for the MTMS-BTSE copolymer SOG, a slightly higher toughness value (~3.5 Jm^{-2}) was estimated by Kim *et al*., from modified-edge-lift-off tests.[47] Thus, comparing the predicted

energy release rate values in Fig. 5.5 with measured bonding layer toughness, polycrystalline Al_2O_3 was identified as the most promising candidate for the receiver substrate, with the lowest overall *G*.

In device applications for which thermal management issues are critical, the thermal conductivities of the potential alternative substrate materials must be considered. Some candidates were chosen as a subset of the materials with similar TECs to GaAs, as shown in Fig. 5.4 (a). The temperature dependence of the thermal conductivity for these semiconductor and ceramic materials are presented in Figure 5.4(b).[45,48-51] In relative terms, Si has moderate values for thermal conductivity: polycrystalline AlN is better and SiC has the highest thermal conductivity of all of the materials considered. In contrast, polycrystalline Al_2O_3, SiN, and $MgAl_2O_4$ are relatively poor thermal conductors. Thus, in terms of thermal conductivity, AlN stands out as a promising alternative to Si. Among the ceramics considered, its thermal conductivity is second only to SiC, but has a lower price (on the order of the price of Si).[52]

5.4.2 Materials Selection: Bonding Agent

In this section, our investigation of the effects of the bonding agent thickness and TEC on the surface morphology of GaAs:N layers transferred via SOG-mediated bonding is presented. In the calculations of the driving force for delamination in Section 5.4.1, we neglected the influence of the SOG due to its negligible thickness with respect to the wafers to be bonded, as shown schematically in Fig. 5.1(a). However, as we will show in this section, the surface

morphology of the transferred GaAs:N layer is critically dependent on the thickness and the TEC of the SOG bonding layer. Indeed, immediately following RTA, much of the original substrate has been removed (via layer splitting) and thus, the thicknesses of the SOG and the transferred layers are very similar, as shown schematically in Fig. 5.1(b).

First, we examined the effect of the layer thickness of a commercial MSSQ SOG (Filmtronics FG65).[53] The ~1000 nm thick films are referred to as “thick,” and the ~200 nm thick films referred to as “thin.” The surface morphology of the transferred layer achieved with the thick SOG film is shown in the SEM image in Fig. 5.6(a). The transferred GaAs:N layers contain channel cracks that apparently extend into the bonding layer, as suggested by the AFM and corresponding line-cut in Fig. 5.6(b). The rms roughness (R_{rms}) of the transferred layer is 190±30 nm, as determined from areas similar to that shown by the dashed-line box in Fig. 5.6(b) (i.e., excluding channel cracks).

To eliminate this channel-cracking, we consider the predicted driving force for cracking in terms of the tensile misfit strain between the bonding layer and substrate. Neglecting the transferred GaAs:N film in the presence of the bonding layer, this driving force for crack propagation, *G,* may be described qualitatively by:

$$G \propto \left(\frac{\sigma_{film}^2 h_{film}}{E_{film}} \right) \tag{5.2}$$

where h_{film} and E_{film} are the film thickness and Young’s modulus, respectively. σ_{film} is the thermal-mismatch stress in the film, given by:

$$\sigma_{film} = E_{film}(\alpha_{substrate} - \alpha_{film})\Delta T \quad (5.3)$$

where $\alpha_{substrate}$ and α_{film} are the TEC of the substrate and film, respectively, and ΔT is the change in temperature from the bonding temperature.

Thus, the driving force, *G,* in Eq. 5.2 may be minimized by decreasing the thickness of the SOG bonding layer (h_{film}). The effect of reducing h_{film} is apparent in the SEM image of the GaAs:N film transferred with a "thin" SOG layer, as shown in Fig. 5.7(a), where channel-cracking is not apparent. In addition, the R_{rms} of the transferred area, indicated by the dashed-line box in Fig. 5.7(b), is 60±20 nm, roughly half that of the cracked layer in Fig. 5.6(b). AFM also reveals "hole" defects (highlighted with a dashed circle in Fig. 5.7(b)). The depths of these defects are on the order of the transferred film thickness, and of a similar diameter to the circular blisters observed in unbonded layers (see, for example, Fig. 3.4). Thus, it is likely that these defects are due to the formation of blisters in localized areas with insufficient bonding.

To further reduce this thermal-mismatch stress and thus reduce *G* (as shown in Eqs. 5.2 and 5.3), we explored an SOG with a TEC more similar to those of the GaAs and ceramic substrates. For this purpose, we used a MTMS-BTSE copolymer based SOG, which has been observed to exhibit composition-dependent TEC.[30] In particular, as shown in Fig. 5.8, the TEC of the copolymer decreases with increasing BTSE concentration (lower x-axis). For comparison, the TECs of GaAs and Al_2O_3 are ~6 $^{o}C^{-1}$ and the TEC of AlN is ~4 $^{o}C^{-1}$, suggesting that a BTSE concentration > 50% is desirable for TEC-matching of the SOG film to the GaAs or ceramic substrates. Due to issues regarding the

stability of the MTMS-BTSE copolymer solution with > 50% BTSE, a composition of 50% was chosen for this study.

Using the MTMS-BTSE SOG, we achieved layer transfer of GaAs:N to Al_2O_3 with an improved surface morphology. As shown in the SEM and AFM micrographs in Fig. 5.9(a) and 5.9(b), the surface of the transferred layer appears featureless, without the presence of cracking or "hole" defects. In addition, R_{rms} of the transferred layer has decreased by nearly an order of magnitude from R_{rms} = 190±30 nm for the cracked layer shown in Fig. 5.6(b) to R_{rms} = 20±5 nm in this case. The 20±5 nm rms roughness is larger than the R_{rms} of the as-implanted GaAs:N layer (~3 nm, as discussed in section 4.4), but it is comparable to the ~15 nm R_{rms} value reported for the low-temperature transfer of a crystalline GaAs layer to a silicon substrate using plasma-enhanced chemical vapor-deposited (PECVD) SiO_2 bonding layers.[13]

In all cases, the transferred layers are "patchy," with isolated areas of layer transfer in a fractal-like pattern, as shown in the SEM micrograph in Fig. 5.10. The patchiness of the transfer suggests initial crack propagation through the bubble layer, followed by crack deflection toward the GaAs/SOG interface. Presumably, this crack propagation is governed by the pressurized gas within the bubbles as well as stresses caused by the thermal expansion mismatch between the GaAs:N and the receiver substrate. Similar patchy morphologies have been observed previously for the transfer of GaAs and complex oxides to Si substrates.[54]

As a first step towards minimizing the patchiness of the transferred layer, we analyzed the crack behavior in terms of the stress intensity factor, K, which describes the driving force for crack propagation in terms of applied loads and geometry. The initial propagation of a crack through the bubble layer and subsequent deflection suggests both an "opening mode" (mode I or K_I) and "shearing mode" (mode II or K_{II}) contribution to the stress intensity factor,[55,56] where the K_{II} contribution will tend to deflect the crack out of the bubble layer and towards the GaAs/SOG interface, as shown in Fig. 5.11. The role of the K_{II} component on the "patchiness" of transfer may also be inferred from the transfer of GaAs:N to GaAs substrate, for which the thermal-expansion mismatch (and K_{II}) is presumably minimized. In this case, a relatively large area of transfer is apparent, as shown in Fig. 5.12, suggesting a lower tendency for crack deflection into the bonding interface. Since this approach involved minimal TEC mismatch between the bonding wafers and the SOG bonding layer, the layer splitting process is likely governed by gas bubble-induced pressure rather than thermal-mismatch stresses.

5.5 Layer transfer of GaAs:N Nanocomposite Layers to Alumina and Aluminum Nitride Substrates

In this section, the successful realization of ion-cut-synthesis for the integration of GaAs:N nanocomposites with alumina and aluminum nitride substrates is discussed, using the optimized MTMS-BTSE SOG bonding

approach described in section 5.4.2. The structures of the transferred GaAs:N layers are revealed by TEM.

To determine the overall structure of the near-surface layers as well as the crystallinity of the transferred GaAs:N layer, bright-field and dark-field TEM imaging was performed along with selected area electron diffraction (SAED). Figure 5.13(a) shows a bright-field TEM image of GaAs:N layers transferred to Al_2O_3 with a MTMS-BTSE SOG bonding layer. Several layers are apparent in the image, including the SOG bonding layer, the GaAs:N nanocomposite layer, and deposited Pt layers. In Fig. 5.13(b), {111} dark-field imaging of the GaAs:N layer reveals nanometer-sized bright features, suggesting the formation of nanocrystalline precipitates. The appearance of nanoscale bright features in the Pt layers suggests that they are also nanocrystalline. SAED from the transferred layer was collected with an aperture ~150 nm in diameter. The resulting SAED pattern, shown as an inset in Fig. 5.13(a), consists of spotty rings related to the polycrystalline zincblende (ZB) GaAs matrix as well as spotty rings associated with {111} and {113} ZB GaN.

The transfer of a GaAs:N nanocomposite layer to an AlN substrate is shown by the bright-field and {111} dark-field TEM images in Figs. 5.14(a) and 5.14(b), respectively. In particular, the bright-field image in Fig. 5.14(a) reveals abrupt GaAs:N/SOG and SOG/AlN bonded interfaces. The dark-field image in Fig. 5:14(b) shows nanometer-scale bright features associated with nanocrystal formation in the transferred layer. Similar to the case of Al_2O_3 transfer, the SAED

of the nanocomposite layer reveals spotty rings associated with the polycrystalline zincblende GaAs matrix, in addition to that of {111} ZB GaN.

The nanocrystalline nature of the nanocomposite layer is also confirmed by high-resolution TEM, as shown in Fig. 5.15(a) and Fig. 5.15(b) for GaAs:N layers transferred to Al_2O_3 and AlN substrates, respectively. In both cases, regions of crystallinity on the order of ~5 nm are apparent within a disordered matrix. Several examples of these nano-crystallites embedded in the disordered matrix are circled in the figure.

Thus, nanostructuring and transfer of GaAs:N layers to Al_2O_3 and AlN substrates was achieved. As shown in the XTEM micrographs in Figs. 5.13 and 5.14, the thicknesses of the layers transferred to both Al_2O_3 and AlN, respectively, are approximately 200 nm. Thus, it is likely that layer transfer has occurred by the formation and propagation of cracks along the depth of bubble formation, as shown schematically in Fig. 5.12.

5.6 Conclusions

In this chapter, we described the successful demonstration and optimization of the ion-cut-synthesis technique. In particular, nanostructuring and transfer of GaAs:N films to Al_2O_3 and AlN substrates were achieved using a spin-on glass bonding agent. Indeed, the low ion-matrix diffusivity of GaAs:N enabled the formation of both nanocrystals and gas bubbles at high temperature. First, the selection processes for SOG bonding layers and substrates suitable for high-

temperature, SOG-mediated wafer bonding was described. The bonding problem was analyzed for the initial bonding step of the implanted GaAs wafer to a receiver substrate, neglecting the thickness of the SOG layer. Next, the bonding problem was analyzed immediately following the high-temperature annealing step, in which case much of the original substrate had been removed such that the SOG layer thickness was on the order of the transferred GaAs:N film thickness. We showed that the thickness and thermal expansion coefficient of the SOG had a significant impact on the morphology of the transferred, nanostructured film.

The optimization of this SOG-assisted bonding process led the transfer of GaAs:N films with rms roughness comparable to that reported for low-temperature transfer of crystalline GaAs layers to Si substrates. Thus, the approaches described in this chapter may be applied generally to problems of bonding and layer transfer for high-temperature-stable heterogeneous materials integration. Furthermore, the integration of nanocomposite materials with a variety of substrates coupled with the ability to recycle the donor substrate makes ion-cut-synthesis attractive for high-efficiency, low-cost electronics, optoelectronics, and energy conversion devices.

5.7 References

[1] G. J. Sullivan, M. K. Szwed, D. A. Hardwick, J. A. Higgins, J. R. Waldrop, and M. F. Chang, Electron. Lett. **29**, 1890 (1993).

[2] R. Adam, M. Mikulicks, A. Förster, J. Schelten, M. Siegel, P. Kordoš, X. Zheng, S. Wu, and R. Sobolewski, Appl. Phys. Lett. **82**, 3485 (2002).

[3] M. Bruel, Electron. Lett. **31**, 1201 (1995).

[4] W. Chen, A. Zhang, P. Chen, J. E. Pulsifer, T. L. Alford, T. F. Kuech, and S. S. Lau, Appl. Phys. Express **2**, 022201 (2009).

[5] L. J. Huang, J. O. Chu, D. F. Canaperi, C. P. D'Emic, R. M. Anderson, S. J. Koester, and H.-S. P. Wong, Appl. Phys. Lett. **78**, 1267 (2001).

[6] H. Moriceau, F. Fournel, B. Aspar, B. Bataillou, A. Beaumont, C. Morales, A. M. Cartier, S. Pocas, C. Lagahe, E. Jalaguier, A. Soubie, B. Biasse, N. Sousbie, S. Sartori, J. F. Michaud, F. Letertre, O. Rayssac, I. Cayrefourcq, C. Richtarch, N. Daval, C. Aulnette, T. Akatsu, B. Osternaud, B. Ghyselen, and C. Mazuré, J. Electron. Mater. **32**, 829 (2003).

[7] L. Di Cioccio, F. Letertre, Y. Le Tiec, A. M. Papon, C. Jaussard, and M. Bruel, Mat. Sci. Eng. B **46**, 349 (1997).

[8] Q.-Y. Tong, T.-H. Lee, L.-J. Huang, Y.-L. Chao, and U. Gösele, Electron. Lett. **34**, 407 (1998).

[9] K. D. Hobart and F. J. Kub, Electron. Lett. **35**, 675 (1999).

[10] Y. Zheng, P. D. Moran, Z. F. Guan, S. S. Lau, D. M. Hansen, T. F. Kuech, T. E. Haynes, T. Hoechbauer, and M. Nastasi, J. Electron. Mater. **29**, 916 (2000).

[11] J. M. Zahler, C.- G. Ahn, S. Zaghi, H. A. Atwater, C. Chu, and P. Iles, Thin Solid Films **403-404**, 558 (2002).

[12] F. J. Kub, K. D. Hobart, J. M. Pond, and S. W. Kirchoefer, Electron. Lett. **35**, 477 (1999).

[13] E. Jalaguier, B. Aspar, S. Pocas, J. F. Michaud, M. Zussy, A. M. Papon, and M. Bruel, Electron. Lett. **34**, 408 (1998).

[14] B. Aspar, E. Jalaguier, A. Mas, O. Locatelli, H. Moriceau, S. Pocas, A. M. Papon, J. F. Michaud, and M. Bruel, Electron. Lett. **35**, 1024 (1999).

[15] I. Radu, I. Szafraniak, R. Scholz, M. Alexe, and U. Gösele, App. Phys. Lett. **82**, 2413 (2003).

[16] I. Radu, I. Szafraniak, R. Scholz, M. Alexe, and U. Gösele, J. App. Phys. **94**, 7820 (2003).

[17] G. Gawlik, J. Jagielski, and B. Piatkowski, Vacuum **70**, 103 (2003).

[18] L. Di Cioccio, E. Jalaguier, and F. Letertre, Phys. Stat. Sol. A **202**, 509 (2005).

[19] H. Moriceau, F. Rieutord, C. Morales, A. M. Charvet, O. Rayssac, B. Bataillou, F. Fournel, J. Eymery, A. Pascale, P. Gentile, A. Bavard, J. Mézière, C. Maleville, and B. Aspar, Solid State Phenom. **121-123**, 29 (2007).

[20] C. Y. Yun, A. B. Wengrow, N. W. Cheung, Y. Zheng, R. J. Welty, Z. F. Guan, K. V. Smith, P. M. Asbeck, E. T. Yu, and S. S. Lau, Appl. Phys. Lett. **73**, 2772 (1998).

[21] T. W. Simpson, I. V. Mitchell, G. O. Este, and F. R. Shepherd, Nucl. Instrum. Methods Phys. Res. B **148**, 381 (1999).

[22] B. Aspar, M. Bruel, M. Zussy, and A. M. Carter, Electron. Lett. **32**, 1985 (1996).

[23] V. P. Popov, I. E. Tyschenko, L. N. Safronov, O. V. Naumova, I. V. Antonova, A. K. Gutakovsky, and A. B. Talochkin, Thin Solid Films **403-404**, 500 (2002).

[24] B. Aspar, M. Bruel, H. Moriceau, C. Maleville, T. Poumeyrol, A. M. Papon, A. Claverie, G. Benassayag, A. J. Auberton-Herve, and T. Barge, Microelectron. Eng. **36**, 233 (1997).

[25] M. Bruel, Nucl. Instrum. Methods Phys. Res. B **108**, 313 (1996).

[26] Q.-Y. Tong, L.-J. Huang, and U. M. Gösele, J. Electron. Mater. **29**, 928 (2000).

[27] J. K. Lee, M. Nastasi, N. D. Theodore, A. Smalley, T. L. Alford, J. W. Mayer, M. Cai, and S. S. Lau, J. Appl. Phys. **96**, 280 (2004).

[28] X. Weng, W. Ye, R. S. Goldman, and J. C. Mabon, J. Vac. Sci. Technol. B **22**, 989 (2004).

[29] X. Weng and R. S. Goldman, U.S. Patent No. 7,056,815 (6 June 2006).

[30] H. W. Ro, K. Char, E.-C. Jeon, H.-J. Kim, D. Kwon, H.-J. Lee, J.-K. Lee, H.-W. Rhee, C. L. Soles, and D. Y. Yoon, Adv. Mater. **19**, 705 (2007).

[31] M. D. Thouless, Acta Metall. et Mater. **38**, 1135 (1990).

[32] M. D. Thouless, Scripta Metall. et Mater. **26**, 949 (1992).

[33] J. W. Hutchinson and Z. Suo, Adv. Appl. Mech. **29**, 63 (1992).

[34] D. M. Hansen, P. D. Moran, K. A. Dunn, S. E. Babcock, R. J. Matyi, and T. F. Kuech, J. Cryst. Growth **195**, 144 (1998).

[35] S. Weichel, R. De Reijs, and M. Lindahl, Sens. Actuators A **70**, 179 (1998).

[36] H. C. Lin, K. L. Chang, G. W. Pickrell, K. C. Hsieh, and K. Y. Cheng, J. Vac. Sci. Technol B **20**, 752 (2002).

[37] E. Jalaguier, B. Aspar, S. Pocas, J. F. Michaud, M. Zussy, A. M. Papon, and M. Bruel, Electron. Lett. **34**, 408 (1998).

[38] R. Feder and T. Light, J.Appl. Phys. **39**, 4870 (1968).

[39] K. Karch, P. Pavone, A. P. Mayer, F. Bechstedt, and D. Strauch, Physica B **220**, 448 (1996).

[40] Y. Okada and Y. Tokumaru, J. Appl. Phys. **56**, 314 (1984).

[41] A. E. Paladino and C. R. Snider, American Ceramic Society Bulletin **49**, 280 (1970).

[42] K. M. Taylor and C. Lenie, J. Electrochem. Soc. **107**, 308 (1960).

[43] O. J. Whittemore and N. N. Ault, J. Am. Ceram. Soc. 39, 443 (1956).

[44] R. M. Williams, J. Am. Ceram. Soc. **63**, 108 (1980).

[45] J. S. Blakemore, J. Appl. Phys. **53**, R123 (1982).

[46] M. Alexe, V. Dragoi, M. Reiche, and U. Gösele, Electron. Lett. **36**, 677 (2000).

[47] B. R. Kim, J. W. Kang, K. Y. Lee, J. M. Son, and M. J. Ko, J. Mater. Sci. **42**, 4591 (2007).

[48] T. B. Jackson, K. Y. Donaldson, and D. P. H. Hasselman, J. Am. Ceram. Soc. **73**, 2511 (1990).

[49] W. D. Kingery, J. Francl, R. L. Coble, and T. Vasilos, J. Am. Ceram. Soc. **37**, 107 (1954).

[50] H. R. Shanks, P. H. Sidles, P. D. Maycock, and G. C. Danielson, Phys. Rev. **130,** 1743 (1963).

[51] A. Sparavigna, Phys. Rev. B **66** (2002).

[52] University Wafer, Boston, MA; http://www.universitywafer.com

[53] Filmtronics, Inc., Butler, PA; http://www.filmtronics.com

[54] I. Radu, PhD Dissertation, Martin Luther Universität Halle-Wittenberg, 2003, Chapter 4.

[55] M. D. Drory, M. D. Thouless, and A. G. Evans, Acta Metall. **36**, 2019 (1988).

[56] Z. Suo and J. W. Hutchinson, Int. J. Fracture **43**, 1 (1990).

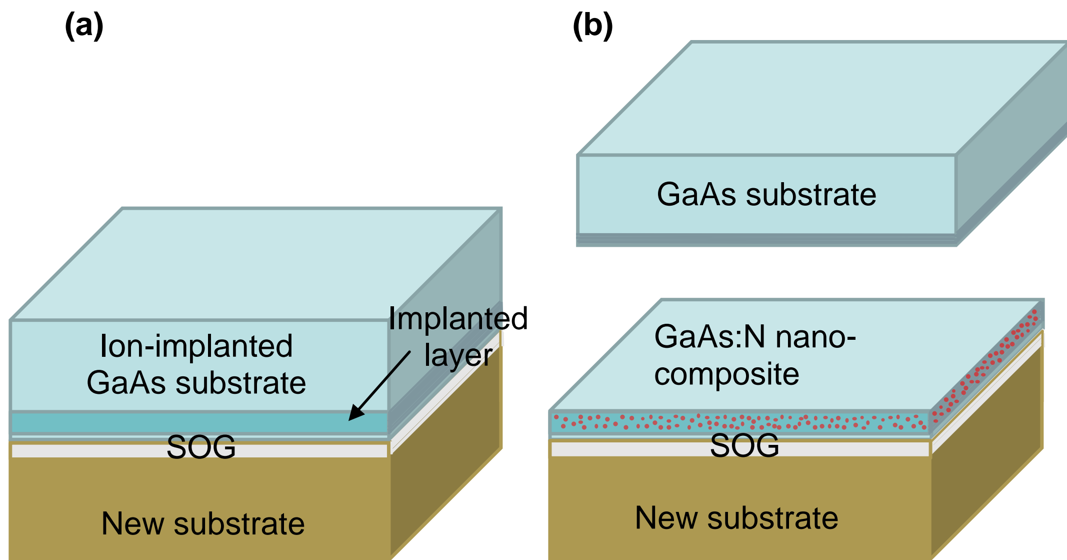

Fig. 5.1 Schematic of the ion-cut-synthesis process. In (a), an ion-implanted GaAs substrate is bonded to a new substrate with a spin-on glass (SOG) intermediate layer. In (b), following thermal annealing, the GaAs:N nanocomposite layer forms and splits from the GaAs substrate, and the layer transfer is accomplished.

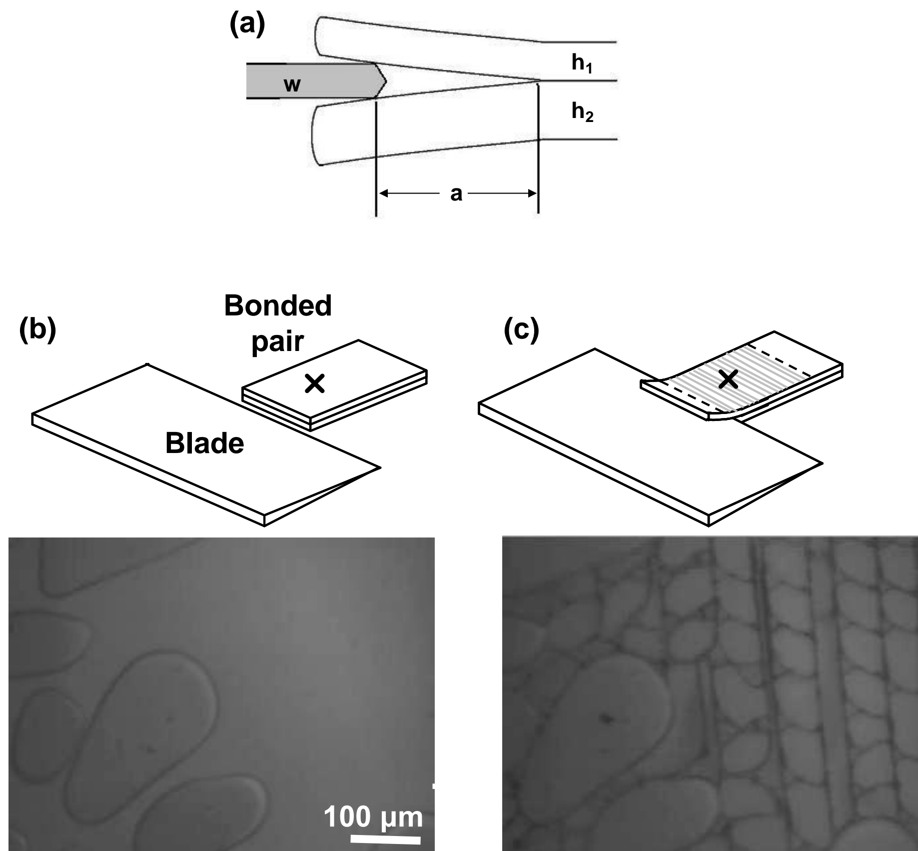

Fig. 5.2 (a) A schematic of the geometry used in the blade test. In (b) and (c), IR microscopy images of SOG-bonded GaAs/GaAs pair (b) before and (c) after delamination are shown. Note that the region shown in (c) is well behind the crack front, as shown in the accompanying schematic.

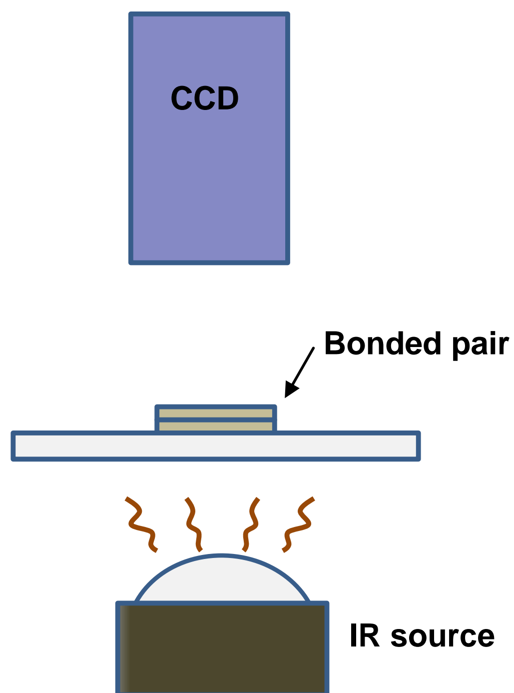

Fig. 5.3 Schematic of the IR microscope system. Infrared radiation from a halogen lamp is transmitted through the bonded sample, and captured by an IR-sensitive CCD camera.

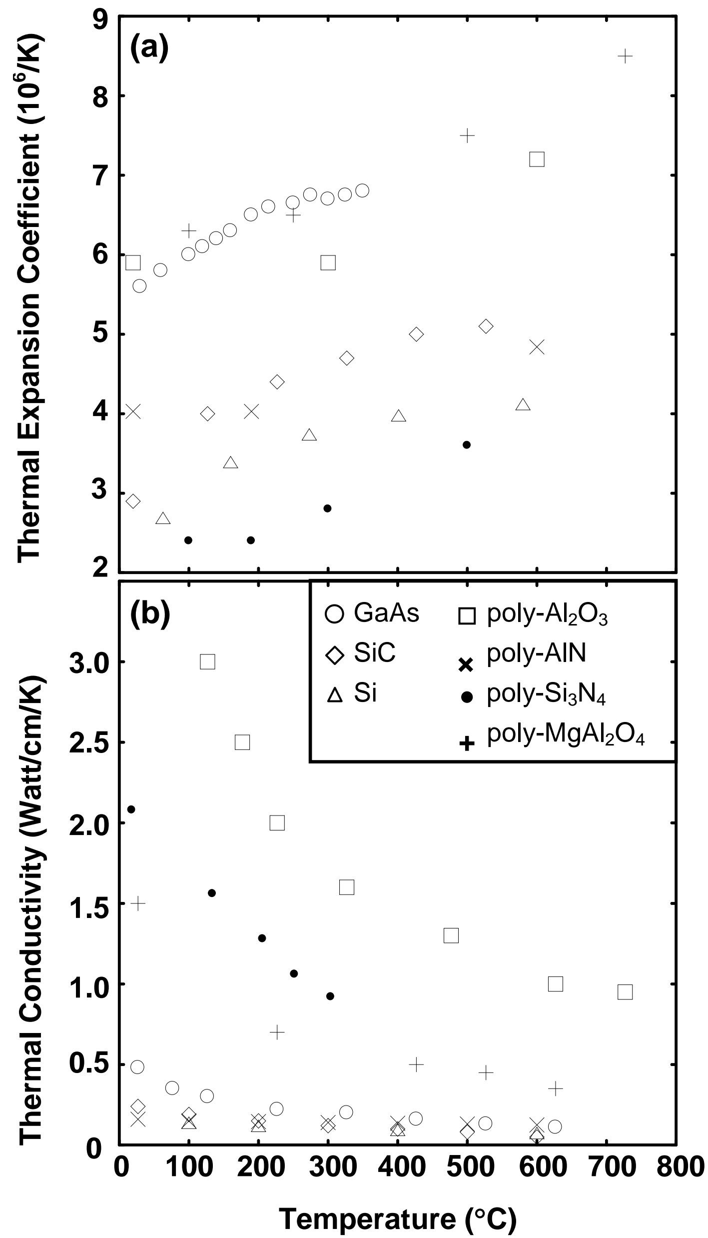

Fig. 5.4 (a) Thermal expansion coefficient and (b) thermal conductivity for various ceramic materials and Si over a range of temperatures.

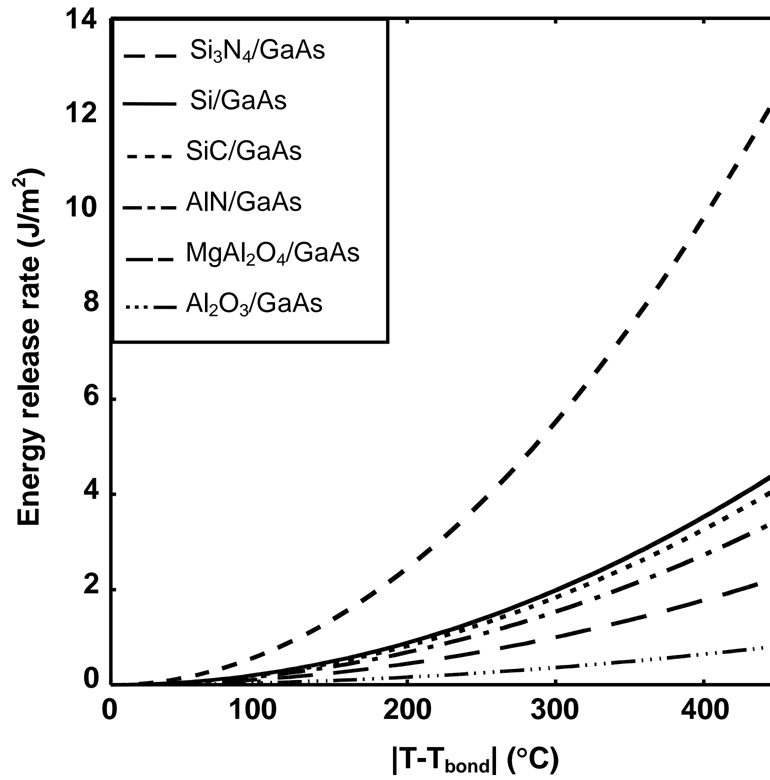

Fig. 5.5 Calculated values for the energy release rate for bonded samples (semiconductor or ceramic/GaAs) as the annealing temperature deviates from the bonding temperature, i.e., the temperature at which the mismatch strain is zero.

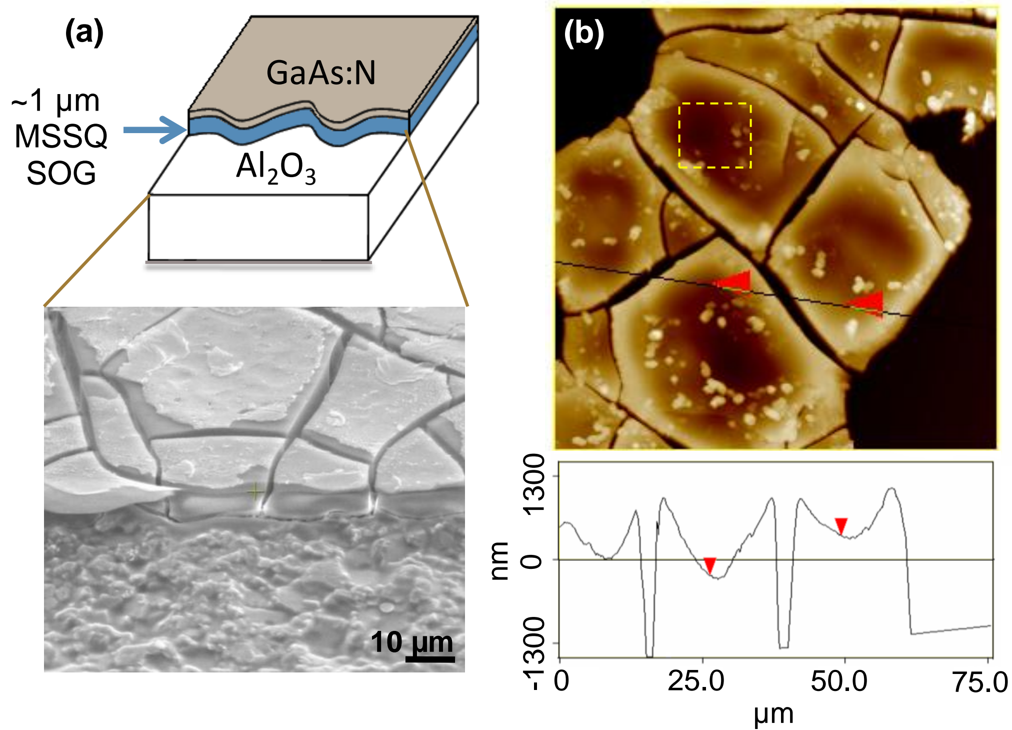

Fig. 5.6 Surface morphology of a GaAs:N layer transferred to an alumina substrate using 1 μm "thick" MSSQ SOG**.** The SEM image of the surface in (a) reveals "mud" cracking. The depth of these cracks, as shown in the AFM of the same layer in (b), suggest that the cracks originate in the SOG layer. Thus, the cracking is likely due to tensile stress in the SOG layer.

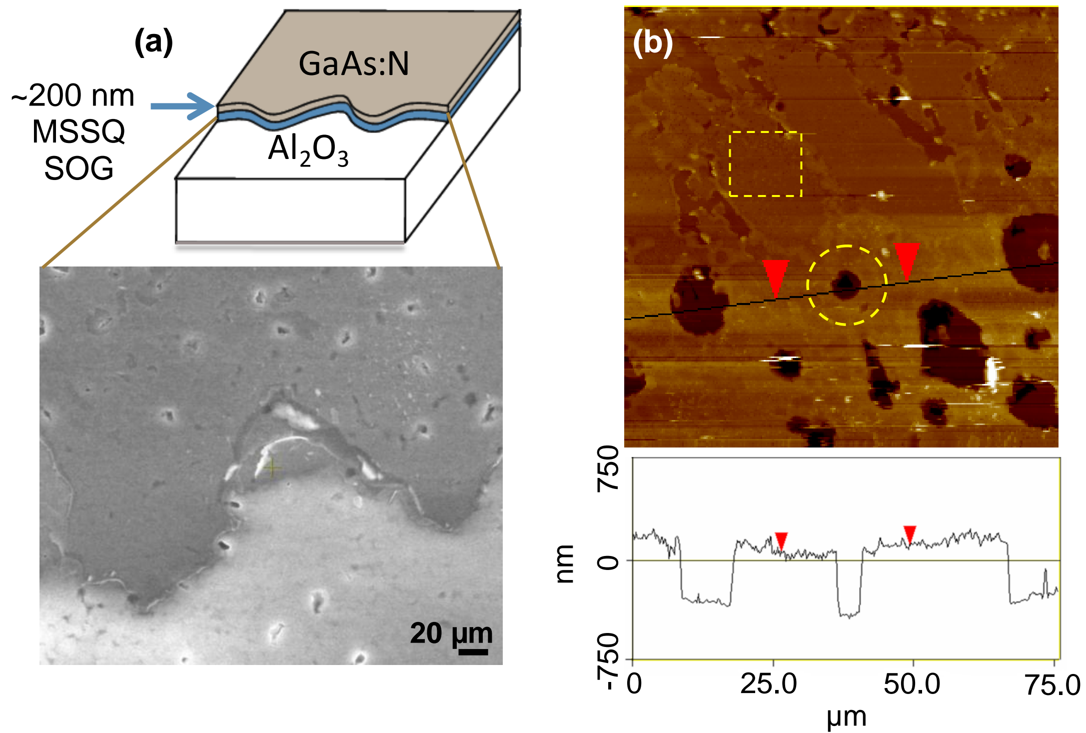

Fig. 5.7 Surface morphology of a GaAs:N layer transferred to an alumina substrate using a "thin" MSSQ layer. In (a), an SEM image of the transferred layer. In (b), AFM of this transferred layer reveals 'hole' defects (highlighted by dashed circles) with depths approximately equal to the transferred layer thickness, suggesting that localized blister formation occurs instead of layer transfer, possibly due to reduced bonding quality.

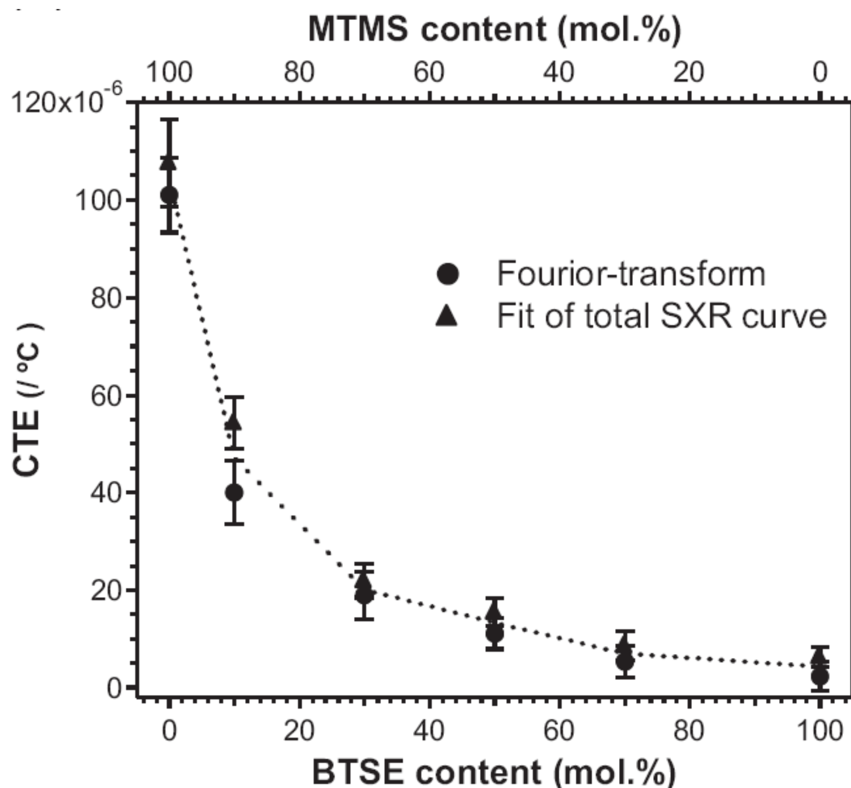

Fig. 5.8 The variation of measured coefficient of thermal expansion (CTE) with composition for a methyltrimethoxysilane - 1,2-bis(triethoxysilyl)ethane (BTSE-MTMS) co-polymer used as a bonding agent. The CTE decreases with increasing BTSE content (lower x-axis). For comparison, the CTE of GaAs is ~6 / ºC); thus, BTSE content > 50% is desirable for CTE-matching to GaAs. Reprinted from: H. W. Ro, K. Char, E.-C. Jeon, H.-J. Kim, D. Kwon, H.-J. Lee, J.-K. Lee, H.-W. Rhee, C. L. Soles, and D. Y. Yoon: High-modulus Spin-on Organosilicate Glasses for Nanoporous Applications. Advanced Materials **19**, p. 706. Copyright Wiley-VCH Verlag GmbH & Co. KGaA. Reproduced with permission.

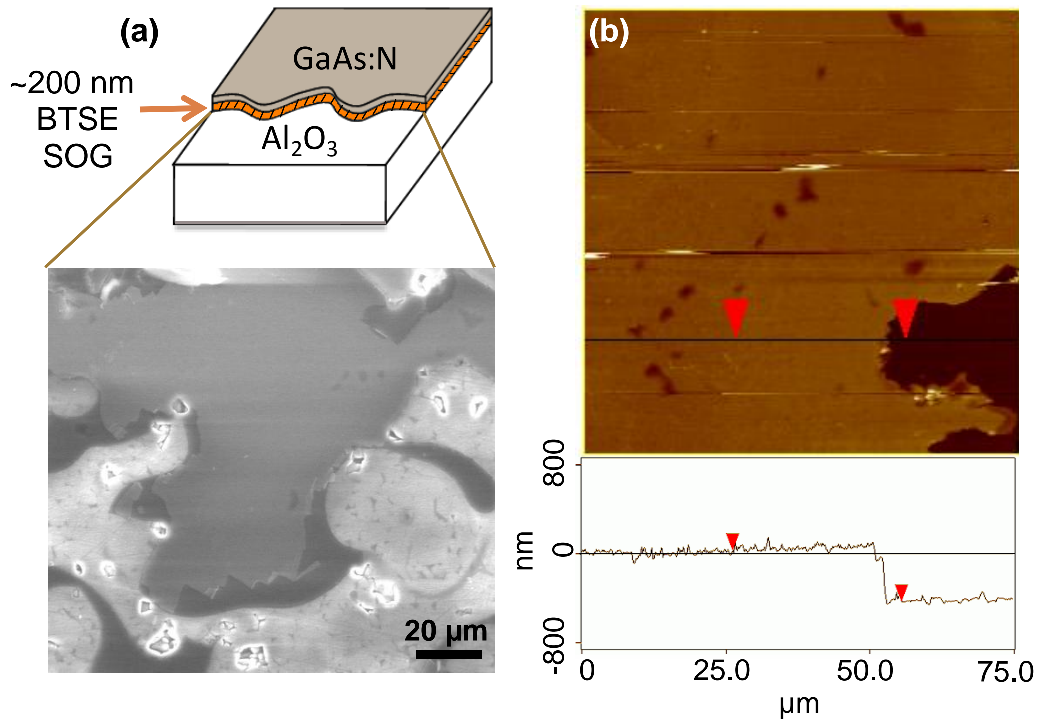

Fig. 5.9 Surface morphology of a GaAs:N layer transferred to an alumina substrate using ~200 nm thick thermally-matched BTSE layer. In (a), an SEM image of the transferred layer, revealing the apparent elimination of hole defects. In (b), AFM of this transferred layer reveals reduced roughness in comparison to the layer transferred with the non-thermally-matched SOG.

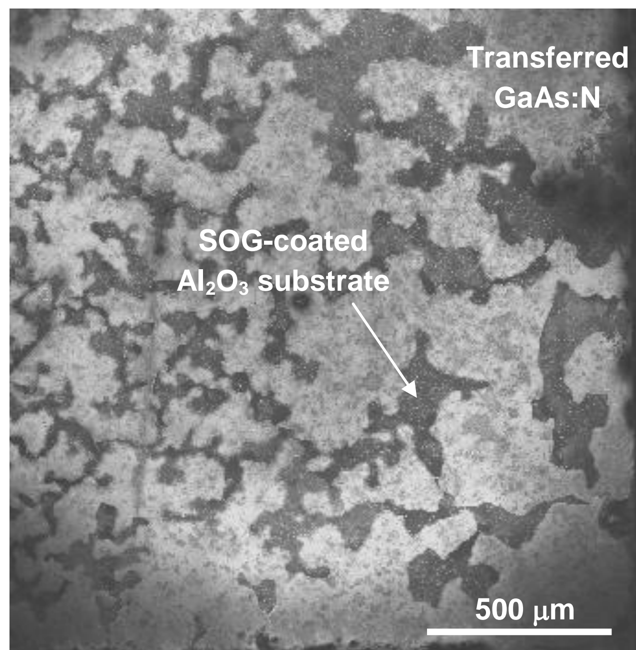

Fig. 5.10 SEM image of a GaAs:N layer transferred to an alumina substrate, illustrating the "patchy" morphology, with isolated areas of layer transfer in a fractal-like pattern.

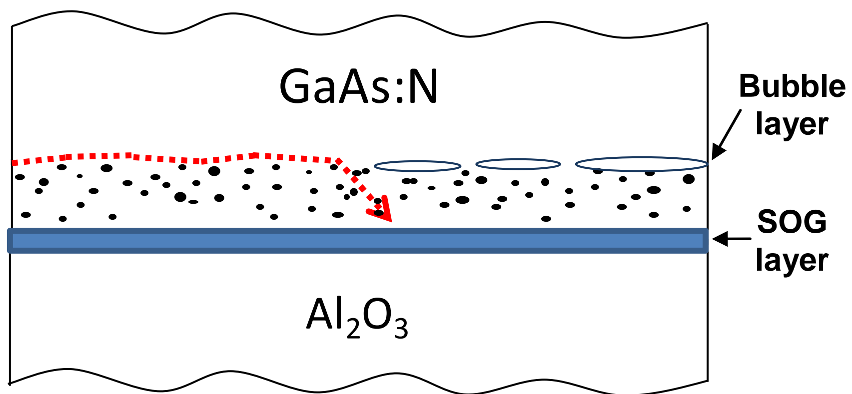

Fig. 5.11 Schematic of the predicted crack trajectory (indicated by the dotted line) leading to the “patchy” morphology layer transfer.

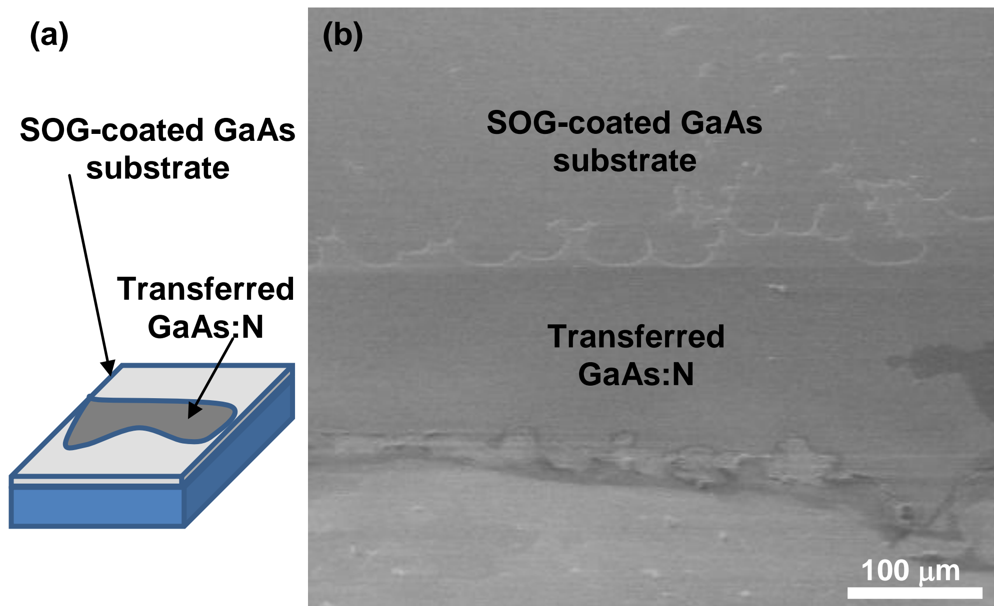

Fig. 5.12 (a) schematic and (b) SEM image (52º tilt) of a GaAs:N layer transferred to a GaAs substrate using a BTSE-SOG bonding layer, illustrating the relatively large area of transfer.

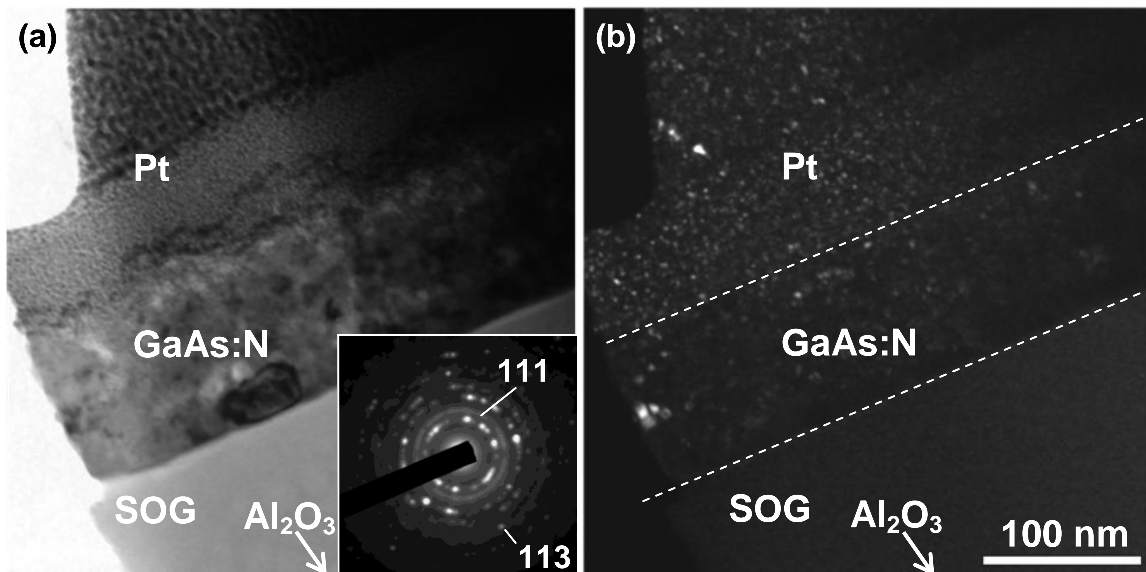

Fig. 5.13 (a) Bright-field and (b) {111} dark-field XTEM images of a GaAs:N layer transferred to an alumina substrate. A selected-area electron diffraction pattern of the GaAs:N layer is shown as an inset in (a) and indicates the presence of cubic GaN crystallites in addition to zincblende GaAs.

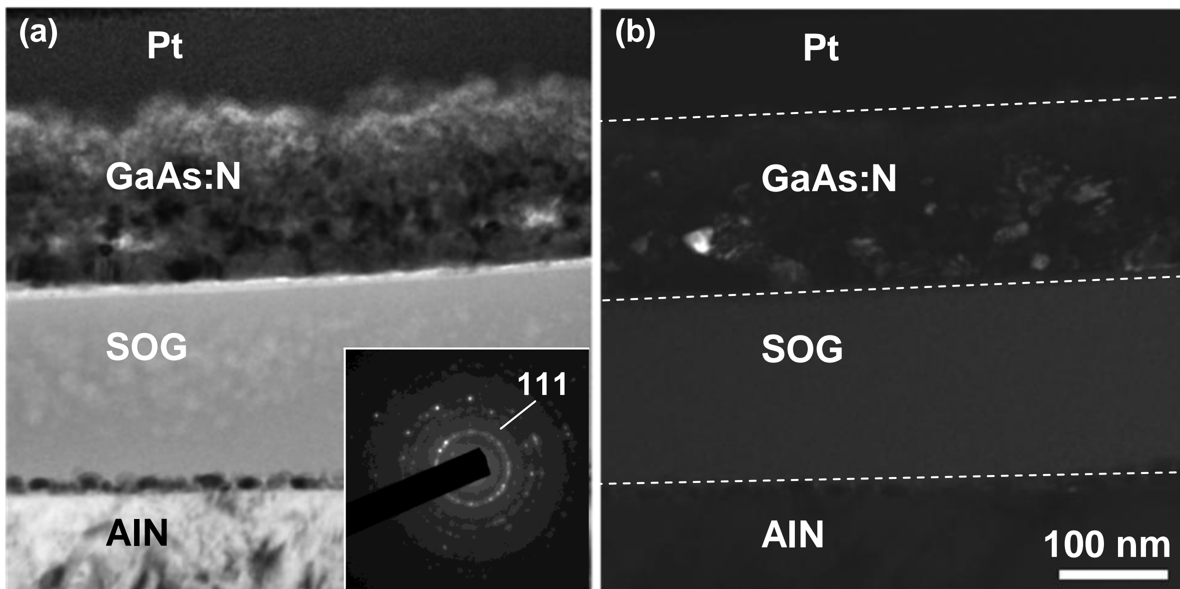

Fig. 5.14 (a) Bright-field and (b) {111} dark-field XTEM images of a GaAs:N layer transferred to an aluminum nitride substrate, A selected-area electron diffraction pattern of the GaAs:N layer is shown as an inset in (a) and indicates the presence of cubic GaN crystallites in addition to zincblende GaAs.

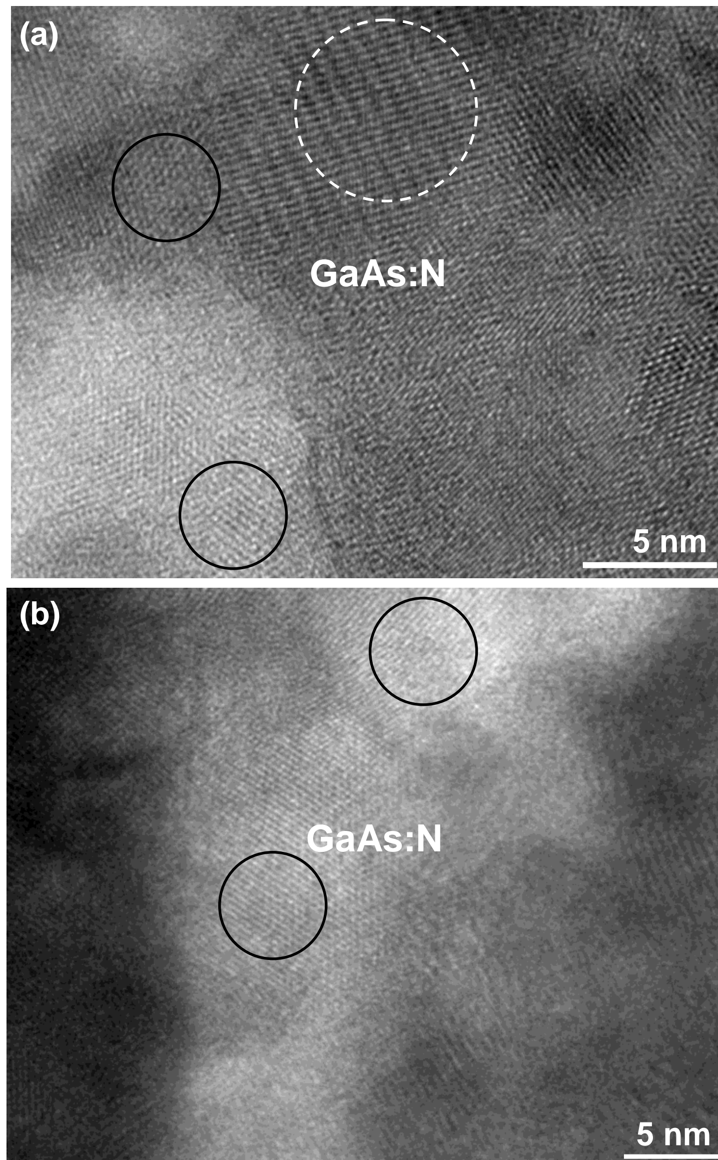

Fig. 5.15 High-resolution TEM micrographs of a GaAs:N layer transferred to (a) Al_2O_3 and (b) AlN substrates, illustrating the polycrystalline nature of the transferred layers. Several crystals with different orientations (suggested by lattice fringes) are highlighted with solid circles. The dashed-line circle shows apparent Moiré fringes, possibly due to the overlap of two crystals with different orientations.

CHAPTER 6

SUMMARY AND SUGGESTIONS FOR FUTURE WORK

6.1 Summary

In this thesis, the blister formation and layer transfer of GaAs:N nanocomposite layers produced by N-implantation, wafer bonding, and rapid thermal annealing (RTA) of GaAs were investigated. In addition, we examined the electrical and thermal transport properties of GaAs:N nanocomposite layers. In Chapter 3, the key role of diffusivity on blister formation in ion-implanted GaAs was revealed. The influence of implantation temperature on blister formation in GaAs:N was studied for low (-196 ^{o}C) and high (300 ^{o}C) implantation temperatures. Local crater depths, average damage depth profiles, and retained N doses were similar, independent of implantation temperature. This is in contrast to the implantation temperature-dependence of these parameters observed in light ion, high-diffusivity systems such as GaAs:H and Si:H. Thus, the low GaAs:N ion-matrix diffusivity, which is independent of the extent of lattice damage, leads to implantation temperature-insensitive exfoliation depths and damage depth profiles.

In Chapter 4, the influence of post-implantation RTA on the surface morphology, electrical properties, and Seebeck coefficient of GaAs:N films was examined. In the temperature regime between 800 and 900 ºC, a transition in surface morphology from circular to predominantly elongated features was observed, presumably due to two distinct delamination behaviors. For low-temperature RTA, circular features were observed, and are presumably associated with the formation of subsurface gas bubbles. For high-temperature RTA, elongated features were also apparent. The elongated features were associated with buckling at the interface between the surface polycrystalline and nanocomposite layers.

The influence of implantation and RTA on the free carrier concentration, *n*, and resistivity, *ρ*, of GaAs:N(Si) and GaAs:N (Te) was also examined. For GaAs, *ρ* follows a log-log dependence on *n*, independent of the dopant species and RTA conditions, consistent with literature reports. Following implantation plus RTA, decreased *n* and increased *ρ* were observed for both dopant types with a more significant increase in *ρ* for the Te-doped GaAs:N layer. Finally, for the implanted plus RTA GaAs:N nanocomposite layers, the measured Seebeck coefficient is slightly enhanced in comparison to that of GaAs.

In Chapter 5, the ion-cut-synthesis technique for nanostructuring and transfer of GaAs:N films to Al_2O_3 and AlN substrates was achieved using a spin-on glass (SOG) bonding agent. Indeed, the low ion-matrix diffusivity of GaAs:N enabled the formation of both nanocrystals and gas bubbles at high temperature. First, the selection processes for SOG bonding layers and substrates suitable for

high-temperature, SOG-mediated wafer bonding was described. The bonding problem was analyzed for the initial bonding step of the implanted GaAs wafer to a receiver substrate, neglecting the thickness of the SOG layer. Next, the bonding problem was analyzed immediately following the high-temperature annealing step, in which case much of the original substrate had been removed such that the SOG layer thickness was on the order of the transferred GaAs:N film thickness. We showed that the thickness and thermal expansion coefficient (TEC) of the SOG had a significant impact on the morphology of the transferred, nanostructured film. The optimization of this SOG-assisted bonding process led the transfer of GaAs:N films with rms roughness comparable to that reported for low-temperature transfer of crystalline GaAs layers to Si substrates.[1]

6.2 Suggestions for Future Work

6.2.1 Thermal Conductivity of GaAs:N Nanocomposite Films

Low-dimensional heterostructures are predicted[2,3] to lead to materials with enhanced thermoelectric figure-of-merit, *ZT*, in comparison to that of bulk materials. *ZT* may be defined as:

$$ZT = S^2 T / \rho\kappa \tag{6.1}$$

where S is the Seebeck coefficient, ρ is the resistivity, and κ is the thermal conductivity. In Chapter 4, room-temperature measurements of the ρ and S of

GaAs:N nanocomposite films were described. However, to fully characterize *ZT*, it is necessary to measure κ as well. In the case of GaAs:N nanocomposite layers, it is likely that phonon scattering due to both the disordered matrix as well as matrix/particle interfaces will contribute to a decrease in κ in comparison to that of the bulk. For example, the addition of ErAs particles to InGaAs layers has been shown to decrease κ by at least a factor of 2.[4]

To characterize the room-temperature *ZT* (Eq. 6.1), thermal conductivity measurements of both MBE-grown GaAs films and GaAs:N nanocomposite films are suggested. For this purpose, the 3ω technique,[5] shown in Fig. 6.1, would be used. For the 3ω technique, a metallic strip with contact pads is deposited on the film surface by photolithography or evaporation though a mask. An AC current is applied at the outermost contacts, and the voltage response measured at the inner contacts is attributed to the thermal response.[6,7]

6.2.2 Alternative Substrates for Ion-cut-synthesis

In Chapter 5, we described the substrate and SOG bonding layer selection processes which led to our successful demonstration of ion-cut-synthesis, using MTMS-BTSE SOG and Al_2O_3 and AlN polycrystalline ceramic substrates. In terms of alternative substrate materials, glass is an attractive candidate for ion-cut-synthesis due to its relatively low cost.[8] Glass-substrate materials integration

has been demonstrated via ion-cut for the transfer of silicon to crystalline quartz[9] as well as the transfer of InP[10] and silicon[11,12] to silicate glasses. These materials combinations are of interest for applications requiring an optically transparent substrate, such as active displays.

Table 6.1: Compositions and properties of selected glasses for alternative substrates for ion-cut-synthesis. The softening point is the temperature at which glass will deform under its own weight. For comparison, the TEC of GaAs at room temperature is ~6.0x10^{-6} /°C.

Glass Type	Wt% SiO_2	Wt% Na_2O	Wt% B_2O_3	Wt% Al_2O_3	Wt% Ba_2O_3	Wt% Others	TEC@RT (10^{-6} /°C)	Softening Point (°C)
Borosilicate	81	3.5		2.5	13		3.25	821
Soda Lime	74	16		1		4 MgO 5 CaO	8.6	726
Barium Borosilicate	18-30	25-48	8-22		25-48	0-6 SnO_2 10-30 La_2O_3	4.6	844
Zinc Borosilicate	74.1	2.8	12.9			9.4 ZnO 0.8 TiO_2	7.38	720
Alkali Borosilicate	63-65	6-9	26-27	3.5			5.15	718
Fused Silica	99.5							1585

In terms of the high temperatures required for ion-cut-synthesis, glasses are promising from the standpoint of their TECs and softening points, as shown in Table 6.1.[13-15] Many of the glasses have TECs similar to those of GaAs. In

addition, the softening point, the temperature at which the glass will deform under its own weight, is similar to the annealing temperature (800°C) needed for the combined formation of nanocrystals and bubbles. Since the ion-cut-synthesis annealing time is very brief (~30 seconds), those glasses with softening points within 100°C of the typical annealing temperature are likely to exhibit minimal deformation.

In all cases, the glass composition must be considered, due to the possibility of cation diffusion into the nanocomposite layer, which may influence the nanocomposite properties, and the performance of fabricated devices. For example, Na contamination is considered to be partly responsible for inferior performance of CdTe/CdS solar cells fabricated on soda-lime glass substrates.[16] Therefore, considering the TEC mismatch with respect to GaAs, the softening point, and the concentration of Na_2O in the glass, alkali borosilicate appears to be the most promising candidate for ion-cut-synthesis. Future work should include layer transfer experiments for ion-cut-synthesis of GaAs:N nanocomposite films to alkali borosilicate glass substrates using a BTSE-MTMS SOG film, as described in Section 5.3.

6.2.3 Photoluminescence of Transferred GaAs:N Layers

The N-incorporation induced bandgap reduction of GaAs is attractive for applications including photovoltaics as well as long-wavelength light emitters and

detectors.[17] In recent years, several groups have explored the optical properties of ion-beam synthesized GaAs:N.[18-21,25] However, in all cases, the ion-beam-synthesized films remain on the parent substrate. For applications in which cost reduction or different-functional substrates are desirable, it would be useful to characterize the properties of GaAs:N nanocomposite films transferred to other substrates by ion-cut-synthesis, as discussed in Chapter 5. There are few reports to date of the optical properties of layers transferred by ion cut. For example, Tajima *et al.*[22] studied the photoluminescence (PL) response of silicon-on-insulator layers, to confirm the presence of oxygen precipitates. Zahler *et al.*[23] also studied PL emission from solar cell structures grown on Ge layers that were transferred to Si by ion cut; however, in this case the transferred Ge layer was only a template for subsequent epitaxy and not part of the active device.

The PL responses of non-transferred GaAs:N layers versus GaAs:N layers transferred to an Al_2O_3 substrate by ion-cut-synthesis are presented in Fig. 6.2. In this case, micro-PL was performed in the Sih lab in the Physics Department at UM, with the assistance of Tim Saucer. The excitation source was a HeNe laser (632 nm), and the laser spot size on the sample was ~2 μm. The PL signals from transferred and non-transferred layers were collected with a liquid-nitrogen-cooled CCD array.[24] For the non-transferred layers, PL features similar to those observed previously by our group are apparent, including the ~1.5 eV emission associated with the fundamental band gap transition of GaAs, as well as a ~1.27 eV emission associated with nitride-rich nanocrystals.[25] However, no PL emission is apparent from the transferred layers. For future

studies of the PL response of transferred layers, studies in which the spot size and/or excitation power of the laser are systematically varied are suggested.

6.3 References

[1] E. Jalaguier, B. Aspar, S. Pocas, J. F. Michaud, M. Zussy, A. M. Papon, and M. Bruel, Electron. Lett. **34**, 408 (1998).

[2] L. D. Hicks and M. S. Dresselhaus, Phys. Rev. B **47**, 12727 (1993).

[3] L. D. Hicks and M. S. Dresselhaus, Phys. Rev. B **47**, 16631 (1993).

[4] J. M. Zide, A. C. Gossard, W. Kim, S. Singer, A. Majumdar, R. Singh, Z. Bian, Y. Zhang, and A. Shakouri, Appl. Phys. Lett. **88**, 113502 (2006).

[5] D. G. Cahill, Rev. Sci. Instrum. **61**, 802 (1990).

[6] D. G. Cahill and R. O. Pohl, Phys. Rev. B **35**, 4067 (1987).

[7] D. J. Kim, D. S. Kim, S. Cho, S. W. Kim, S. H. Lee, and J. C. Kim, Int. J. Thermophysics **25**, 281 (2004).

[8] MTI Corporation, Richmond, CA; http://www.mtixtl.com/fusedsilicasubstratessio2.aspx

[9] C. Maleville and C. Mazuré, Solid State Electron **48**, 1055 (2004).

[10] W. Chen, A. Zhang, P. Chen, J. E. Pulsifer, T. L. Alford, T. F. Kuech, and S. S. Lau, Appl. Phys. Express **2**, 022201 (2009).

[11] M. Cai, D. Qiao, L. S. Yu, S. S. Lau, C. P. Li, and L. S. Hung, J. Appl. Phys. **92**, 3388 (2002).

[12] K. K. Maurya, S. K. Halder, S. P. Chowdhury, and M. B. Dutt, Mater. Lett. **61**, 3017 (2007).

[13] Corning, *Lighting Materials Key Products*, http://www.corning.com/lightingmaterials/

[14] G. B. Hares and D. W. Morgan, *Barium Borosilicate Optical Glasses,* Corning Glass Works, US Patent No. 3964918 (June 22, 1976).

[15] R. M. Wiker, *Zinc Borosilicate Opal Glasses,* Corning Glass Works, US Patent No. 4376170 (March 22, 1982).

[16] R. Dhere, K. Ramanathan, J. Keane, J. Zhou, H. Moutinho, S. Asher, and R. Noufi, 31st IEEE Photovoltaics Specialists Conference and Exhibition (2005), NREL/CP-520-37368

[17] M. Kondow, T. Kitatani, S. Nakatsuka, M. C. Larson, K. Nakahara, Y. Yazawa, M. Okai, and K. Uomi, IEEE J. Sel. Areas. Commun. **3**, 719 (1997).

[18] M. Mikulics, M. Marso, I. Camara Mayorga, and R. Güsten, Appl. Phys. Lett. **87**, 041106 (2005).

[19] S. Dhara, P. Magudapathy, R. Kesavamoorthy, S. Kalavathi, K. G. M. Nair, G. M. Hsu, L. C. Chen, K. H. Chen, K. Santhakumar, and T. Soga, Appl. Phys. Lett. **87**, 261915 (2005).

[20] K. M. Yu, W. Walukiewicz, M. A. Scarpulla, O. D. Dubon, J. Wu, J. Jasinski, Z. Liliental-Weber, J. W. Beeman, M. R. Pillai, and M. J. Aziz, J. Appl. Phys. **94**, 1043 (2003).

[21] X. Weng, R. S. Goldman, V. Rotberg, N. Bataiev, and L. J. Brillson, Appl. Phys. Lett. **85**, 2774 (2004).

[22] M. Tajima, A. Ogura, T. Karasawa, and A. Mizoguchi, Jpn. J. Appl. Phys. **37**, L1199 (1998).

[23] J. M. Zahler, C.-G. Ahn, S. Zaghi, H. A. Atwater, C. Chu, and P. Iles, Thin Solid Films **403-404**, 558 (2002).

[24] Princeton Instruments Model Spec 10:100, www.princetoninstruments.com

[25] X. Weng, S. J. Clarke, W. Ye, S. Kumar, R. S. Goldman, A. Daniel, R. Clarke, J. Holt, J. Sipowska, A. Francis, and V. Rotberg, J. Appl. Phys. **92**, 4012 (2002).

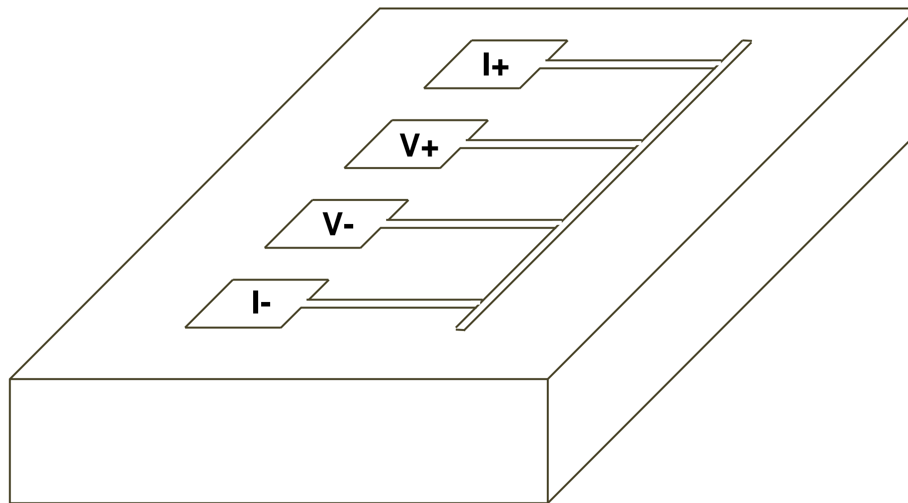

Fig. 6.1 Schematic of the sample geometry for the “3ω” measurement of the thermal properties of a film. A metallic line with contact pads is deposited on the film surface, and an AC current input at the outermost pads (indicated by the solid line) with frequency ω. The metal line acts as a heat source as well as a thermometer, due to its temperature-dependent resistivity. The voltage response ,which varies as 3ω, is measured at the inner contacts (indicated by the dashed line), and can be related to the thermal conductivity of the film. Adapted from Ref. 5.

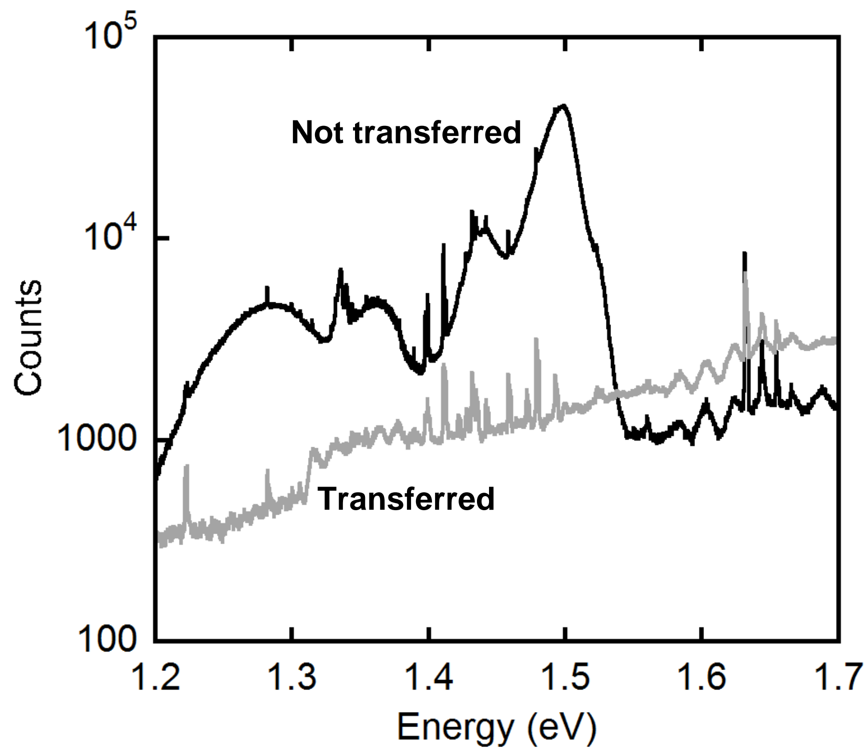

Fig. 6.2 Photoluminesence spectra from GaAs:N layers still on the parent GaAs substrate ("not transferred") and GaAs:N layers transferred to an alumina substrate ("transferred").

APPENDICES

APPENDIX A

Data Analysis

A.1 Retained N Dose Calculation

To estimate the retained N dose, the nuclear reaction analysis (NRA) spectra of GaAs:N films were compared with spectra of TiN standards of known thickness and composition. NRA was performed on N-implanted GaAs and TiN samples and the integrated counts Y under the alpha-particle peak compared. Using the following expression:

$$Y = N_s \sigma(\theta) Q \Omega \qquad \text{(A.1)}$$

where Q is the number of incident particles measured by the charge integrator, Ω is the solid angle of the detector, and $\sigma(\theta)$ is the scattering cross section for a given detection angle θ, the retained fluence of N in GaAs may be correlated to the TiN standard according to:

$$N_{GaAs:N} = N_{TiN} \frac{Y_{GaAs:N}\, Q_{TiN}}{Y_{TiN}\, Q_{GaAs:N}} \qquad \text{(A.2)}$$

For measurements taken for the same experimental setup, it is assumed that Ω and $\sigma(\theta)$ may be treated as constants. Furthermore, it is assumed that the TiN samples are stoichiometric. The uncertainty in the retained dose calculation is estimated from the reported error-bars of the measured cross-section[1] at 1.2 MeV and is ~7%.

A.2 Depth Profiling of RBS Data

To determine the depth profile of lattice damage, channel-to-energy and energy-to-depth conversions were performed, as described below.

A.2.1 Channel-to-energy Conversion

A backscattered He^{++} ion from a target atom will have a characteristic energy corresponding to the kinetics of the backscattering event as well as any energy lost to collisions as it travels in and out of the target material. The collected signal from a backscattered ion will be converted to an electron-hole pair in the detector, and the resulting charge pulse converted to a voltage signal. This voltage signal is processed by an amplification system and multichannel analyzer which 'bins' the signals into a raw counts vs. channel spectrum. To

correlate the channel numbers to backscattered energy values, a backscattering spectrum is recorded from a Au film and a Si substrate. The high-energy edges of these signals, corresponding to backscattering from surface layers, are used to fit a linear channel-to-energy profile.

A.2.2 Energy-to-depth Conversion

The energy *E*(x) of backscattered He^{++} particle after traversing some depth *x* in a material is given by the following equation:

$$E(x) = E_0 - \int_0^x \frac{dE}{dx'}(E(x'), x')dx' \quad \text{(A.3)}$$

where the integral term describes the energy- and depth-dependent stopping power.[2] Differentiating this expression with respect to *x* gives the following relationship:

$$\frac{dE}{dx} = -\epsilon(E) \quad \text{(A.4)}$$

where $\epsilon(E)$ is the energy-dependent stopping cross-section. To relate the measured spectrum to a depth profile for N-implanted GaAs, SIMNRA[2] software was used to simulate the backscattered energy, based on stopping cross-section data from Ziegler.[3] For this analysis, it is assumed that the channeling stopping power is the same as the random stopping power (i.e, the “Aarhus convention”).[4] Assuming a constant density of the GaAs matrix equal to that of stoichiometric

GaAs,[5] the simulated He^{++} backscattered energy from GaAs can be fit to a linear profile, as shown in Fig. A.1.

A.4 References

[1] S. Pellegrino, L. Beck, and P. Trouslard, Nucl. Instrum. Methods Phys. Res. B **219-220**, 140 (2004).

[2] M. Mayer, SIMNRA Users Guide, Report IPP 9/113 (Max-Plank-Institut für Plasmaphysik, Garching, Germany, 1997).

[3] J. F. Ziegler, J. P. Biersack, and U. Littmark, The Stopping and Range of Ions in Matter, Pergamon, New York, 1985.

[4] M. L. Swanson, in *Handbook of Modern Ion Beam Materials Analysis,* Pittsburgh: Materials Research Society, (1995), p. 248.

[5] J. S. Blakemore, J. Appl. Phys. **53**, R123 (1982).

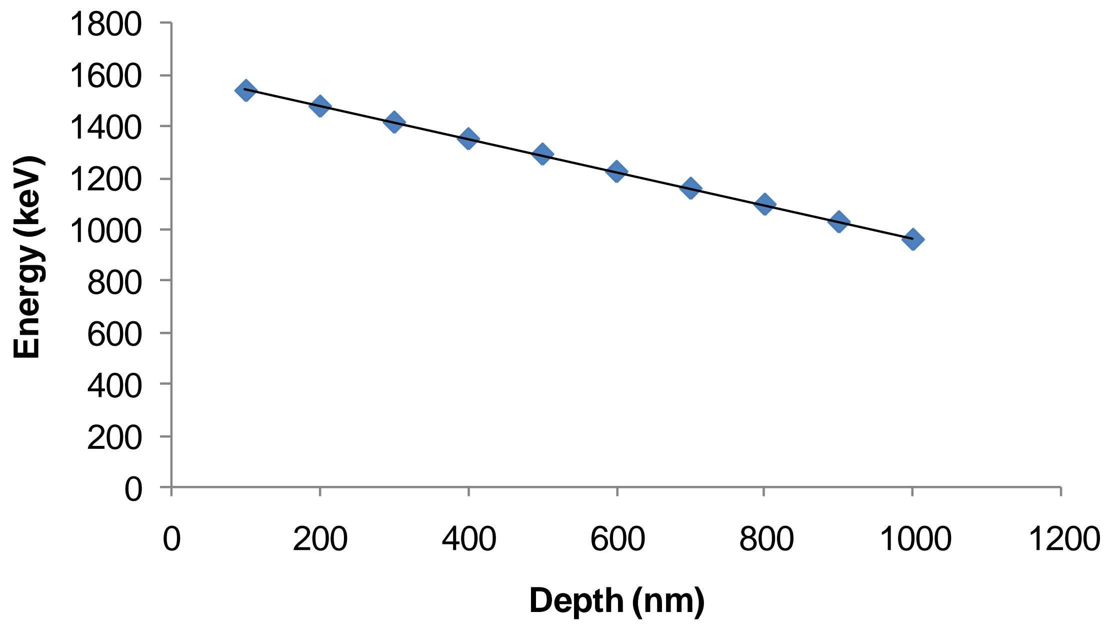

Fig. A.1 Backscattered He^{++} energy with depth in GaAs as given by SIMNRA simulations, used to relate experimental backscattered energy to depth in GaAs:N layers (in Fig. 3.7).

APPENDIX B

Wafer Bonding Experiments

B.1 Overview

This appendix describes the wafer bonding experiments used for bonding GaAs or N-implanted GaAs with alternative substrates. First, efforts at high-temperature stable bonding of GaAs and Si are described in Table B.1. Next, experiments for bonding GaAs to glass, alumina, or aluminum nitride are listed in Table B.2. Finally, all attempts at ion-cut-synthesis by bonding N-implanted GaAs to any of these substrates are detailed in Table B.3. In all cases, either a spin-on glass (SOG) or a combination of spin-on glass and plasma-enhanced chemical vapor deposited (PECVD) silica were used as a bonding agent, as detailed below. Often the semiconductor or ceramic substrates were mechanically thinned by polishing; the final thicknesses of the wafers as measured by a micrometer are listed in each case. In some cases, blade test experiments were performed to measure interfacial toughness as listed in notes column; details of the experimental procedures are provided in Section 5.3.

Table B.1: Summary of wafer bonding experiments for GaAs/SOG/Si integration. In all cases, the silicon wafers were cleaned using a standard RCA procedure.[1] GaAs wafers were cleaned with a sequence of deionized water, methanol, acetone, isopropanol, ammonium hydroxide and hydrochloric acid, except where noted. Samples were bonded at room temperature using pressure applied by tweezers unless otherwise noted. Many of these experiments were performed with the aid of Ellen Burgunder, Tao Sun, or Da Mao.

Trial #	Si (µm)	GaAs (µm)	SOG	Bake procedure before anneal?	Max. anneal *T*	Bonded ?	Notes
1	~500	625	Methylsiloxane (MSQ) (500F)	Yes –1 min @ 85ºC	N/A	No	*clamped for 1 hr in XTEM clamp*
2	~500	625	(MSSQ) (550F)	No	400ºC	No	
3	~500	625	MSSQ 550F	Yes – 175ºC,10 min; 220ºC,15 min	300ºC	Yes	*Bonding pressure applied by two 1x1x5 cm copper blocks (~ 0.05kg each)*
4	~500	625	MSSQ 550F	Yes (as above)	350ºC	Yes	*Bonding pressure applied by two Cu blocks (~ 0.05kg each)*
5	~500	625	MSSQ 550F	Yes (as above)	425ºC	No	*Bonding pressure applied by two Cu blocks (~ 0.05kg each)*
6	~500	625	MSSQ 550F	Yes (as above)	385ºC	No	*Bonding pressure applied by two Cu blocks (~ 0.05kg each)*
7	~500	625	MSSQ 550F	No	300ºC	Yes	*As of this trial: adding H_2O_2 to $NH_4OH:H_2O$ solution for GaAs clean.*

Table B.1, continued

Trial #	Si (μm)	GaAs (μm)	SOG	Bake procedure before anneal?	Max. anneal *T*	Bonded ?	Notes
8	~500	625	MSSQ 550F	No	350ºC	No	*Noticed filmy appearance of GaAs. Bonding pressure applied by two Cu blocks (~ 0.05kg each)*
9	~500	~360	MSSQ 550F	No	350ºC	Yes	*Noticed filmy appearance of GaAs again. Cleaned it twice.*
10	~500	~360	MSSQ 550F	No	385ºC	Yes, but debond ed later	*Noticed filmy appearance of GaAs again.*
11	~355	~270	MSSQ 550F	No	425ºC	No	*Noticed filmy appearance of GaAs again.*
12	~290	~285	MSSQ 550F	No	N/A	N/A	
13	~245	~300	MSSQ 550F	No	425ºC	No	
14	~245	~245	MSSQ 550F	No	425ºC	No	
15	~245	~250	MSSQ 550F	No	425ºC	No	*As of this experiment, changed GaAs cleaning procedure to that described in Ref. 2*
16	~170	~150	MSSQ 550F	No	425ºC	No	
17	~150	~150	MSSQ 550F	No	425ºC	No	
18	~175	~175	MSSQ 550F	No	385 ºC	Yes	
				No	405 ºC	Debond ed later	*further anneal of the bonded sample*
19	~150	~190	MSSQ 550F	No	385 ºC	Yes	
20	~150	~180	MSSQ 550F	No	405 ºC	Yes, Debond ed later	

Table B.1, continued

Trial #	Si (µm)	GaAs (µm)	SOG	Bake procedure before anneal?	Max. anneal *T*	Bonded ?	Notes
21	~170	~150	MSSQ 550F + PECVD Silica	No	385 ºC	Yes	*After wafer clean: deposit 80 nm PECVD SiO_2, anneal, apply SOG and bond, and anneal again*
22	~230 And ~240	N/A	MSSQ 550F	No	425 °C	Yes	
23	N/A	~240 and ~270	MSSQ 550F	No	425 °C	Yes	
24	~230 and ~240	N/A	N/A; PECVD silica only	No	850 ºC	No	*Annealed samples before and after stacking.*
25	N/A	~250 and ~260	N/A; PECVD silica only	No	850 ºC	Yes	*Annealed samples before and after stacking. A white film appeared on silica-coated surface after annealing.*
26	~150	~150	N/A; PECVD silica only	No	850 ºC	No	*Same procedure as exps. 24 and 25. A white film appeared on the GaAs as before.*
27	~250 and ~250	N/A	MSSQ 550F	-No	350 ºC	Yes	
28	N/A	~430 and ~470	MSSQ 550F	No	350 ºC	Yes	*Blade test inconclusive*
29	N/A	~160 and ~150	MSSQ 550F	No	350 ºC	Yes	*Blade test: ~2 Jm^{-2}*
30	N/A	~180 and ~200	MSSQ 550F	No	350 ºC	Yes	*Blade test: inconclusive: fractured through thickness of wafer*
31	N/A	~150 and ~150	MSSQ 550F	No	350 ºC	Yes	*Blade test: inconclusive: fractured through thickness of wafer*

Table B.1, continued

Trial #	Si (μm)	GaAs (μm)	SOG	Bake procedure before anneal?	Max. anneal *T*	Bonded ?	Notes
32	N/A	~190 and ~210	MSSQ 550F	No	350 ºC	Yes	*Blade test: ~1.4 Jm^{-2}*
47	~160	~180	FOX-12 HSQ	No	385 ºC	No	*No bonding at room temperature either*
48	~170	~200	FG65 MSSQ	No	385 ºC	Yes	
					800 ºC subseq uent anneal	No	
49	~170	~200	FG65 MSSQ	No	425 ºC	Yes	

Table B.2: Summary of wafer bonding experiments for GaAs/SOG/Al_2O_3, GaAs/SOG/AlN, or GaAs/SOG/glass integration. From this point on, no prior bake step was performed for the SOG layers. The ceramic and GaAs substrates were cleaned with a sequence of deionized water, acetone, and methanol, as described in Ref. 2, unless otherwise noted. Samples were bonded at room temperature using pressure applied by tweezers.

Trial #	Material (μm)	GaAs (μm)	SOG	Max. anneal *T*	Bonded?	*Notes*
33	Al_2O_3 ~100	~290	MSSQ	350 ºC	Yes	*Blade test inconclusive: cannot discern crack length*
34	Al_2O_3 ~100	~230	MSSQ	350 ºC	Yes	*Blade test: ~1.2 Jm^{-2}*
35	Al_2O_3 ~100	~190	MSSQ	425ºC	Yes	*Blade test inconclusive: cannot discern crack length, checked sample afterwards: debonded completely… during test or afterward?*

Table B.2, continued:

Trial #	Material (μm)	GaAs (μm)	SOG	Max. anneal *T*	Bonded?	*Notes*
36	Al_2O_3 ~100	~190	MSSQ	425 ºC	Yes	*Blade test inconclusive: fractured through thickness of GaAs wafer*
37	Al_2O_3 ~100	~220	MSSQ	425 ºC	Yes	*Blade test: crack appears to run 'diagonally' w.r.t. blade: toughness ~0.075-0.3 Jm^{-2}*
38	Al_2O_3 ~100	~240	MSSQ	425 ºC	Yes	*Blade test: entire sample delaminated. Estimate upper bound on toughness of only ~0.1 Jm^{-2}*
39	Soda lime glass ~1000	~210	MSSQ	300 ºC	Yes	*Blade test: Estimated toughness at ~6 Jm^{-2}?*
41	Al_2O_3 ~100	~190	MSSQ	300 ºC	Yes	
42	Al_2O_3 ~100	~220	MSSQ	385 ºC	Yes	
43	Al_2O_3 ~100	~220	MSSQ	385 ºC	Yes	
50	GaAs ~200	Al_2O_3 ~100	MSSQ	425 ºC	Yes	
				800 ºC subsequent RTA	Yes	
64	GaAs ~600	AlN~380	MSSQ	800 ºC, RTA	No bond	*Spin: 4000rpm*
65	GaAs ~220	AlN~380	MSSQ	800 ºC, RTA	Bonded, debonded later	*Spin: 4000rpm (debonded later)*
68	GaAs ~200	AlN (polished) ~380	MSSQ	800 ºC, RTA	Bonded, debonded later	

Table B.3: N-implanted GaAs (GaAs:N) bonding experiments for ion-cut-synthesis. All GaAs:N samples were fabricated from epitaxial GaAs samples grown in the Goldman Group Varian Gen II MBE system. The MBE sample number and doping type is indicated where applicable. The implantation conditions were N^+ at an energy of 100 keV and targeted fluence of $5x10^{17}$ cm^{-2} unless noted otherwise. Samples were bonded at room temperature using pressure applied by tweezers.

Trial #	GaAs:N (doping)	Material (µm)	SOG	Impl. *T*	Max. anneal *T*	Bonding/ splitting	*Notes*
40	295C undoped ~250	GaAs ~190	550F MSSQ	300ºC	850 ºC	Bonded	*Initially, rapid thermal anneal (30s), later 8 hrs; no layer splitting observed. SEM images of interface.*
44	187B undoped ~480	GaAs ~140	550F MSSQ	300ºC	850 ºC	Bonded	*RTA (30s); no layer splitting observed. Longer anneal (8h): still no splitting SEM images of interface.*
45	443D $\sim 1x10^{18}$ ~600	GaAs ~500	550F MSSQ	300ºC	900 ºC	Bonded, no splitting	*RTA(30s). Sample broke during dicing: imaged implanted sample in SEM*
46	13F ~600	Si ~240	550F MSSQ	300ºC	900 ºC	No bonding	*RTA(30s): SOG appears to coat both wafers. Possible exfoliation?*
51	187G3 undoped 75keV implant	Al_2O_3 ~100	FG65 MSSQ	300ºC	800 ºC, RTA, later: 10h at 800 ºC	Bonded, no splitting	

Table B.3, continued:

Trial #	GaAs:N (doping)	Material (µm)	SOG	Impl. *T*	Max. anneal *T*	Bonding/ splitting	*Notes*
52	295D1 undoped	Al_2O_3 ~100	FG65 MSSQ	300ºC	800 ºC, RTA	Split, layer transfer	
53	295D2 undoped	Al_2O_3 ~100	FG65 MSSQ	300ºC	800 ºC, RTA	Bonded, no splitting	
54	295D3 undoped	Al_2O_3 ~100	FG65 MSSQ	300ºC	800 ºC, RTA	Split, layer transfer	
55	539J2 ~6x10^{17}	Al_2O_3 ~100	FG65 MSSQ	300ºC	800 ºC, RTA	Bonded, no splitting	
56	187H3 undoped	Al_2O_3 ~100	FG65 MSSQ	300ºC	800 ºC, RTA	Split, layer transfer	
57	539J4 ~6x10^{17}	Al_2O_3 ~100	FG65 MSSQ	300ºC	800 ºC, RTA, then 900 ºC RTA	Bonded, no splitting	*Repeating #55*
58	295D4 undoped	GaAs ~600	FG65 MSSQ	300ºC	800 ºC, RTA	Bonded, no splitting	
59	IQE-04L-1undoped	Al_2O_3 ~100	FG65 MSSQ	77K	800 ºC, RTA	Split, layer transfer	*Little layer transfer apparent.*
60	IQE-04L-2undoped	Al_2O_3 ~100	FG65 MSSQ	77K	900 ºC, RTA	Split, layer transfer	
66	LANL04-IQE-11 undop	Al_2O_3 (polished) ~100	FG65 MSSQ (175nm)	77K	800 ºC, RTA	Bonded at RT; debonded after RTA, no layer transfer	
69	LANL04-IQE-12 undop	Al_2O_3 (polished) ~100	FG65 MSSQ (175nm)	77K	800 ºC, RTA	Small amount of layer transfer?	*Bonded in Van Vlack lab hood*

Table B.3, continued:

Trial #	GaAs:N (doping)	Material (µm)	SOG	Impl. *T*	Max. anneal *T*	Bonding/ splitting	*Notes*
70	LANL04-IQE-10 undop	Al_2O_3 (polished) ~100	FG65 MSSQ (175nm)	77K	800 ºC, RTA	Small amount of layer transfer?	
72	LANL04-IQE-9 undop	Al_2O_3 (polished) ~100	FG65 MSSQ	77K	800 ºC, RTA	No bonding	*Spin: 2000rpm, t?*
73	IQE-I2-A1 undop.	Al_2O_3 (polished) ~100	NIST SOG 30% BTSE	77K	800 ºC, RTA	No bonding	*Spin: 1500rpm 60s*
74	IQE-I2-A2 undop.	Al_2O_3 (polished) ~100	NIST SOG 30% BTSE	77K	800 ºC, RTA	No bonding	*2nd attempt with 30% BTSE formula: same spin speed, shorter time Spin: 1500rpm 30s*
75	IQE-I2-A3 undop.	Al_2O_3 (polished) ~100	NIST SOG 30% BTSE	77K	800 ºC, RTA	Split, layer transfer	*3rd attempt, lower spin speed Spin:1000rpm, 30s*
76	295G3A undop.	Al_2O_3 (polished) ~100	NIST SOG 50% BTSE	77K	800 ºC, RTA	Split, layer transfer	*Spin:1500rpm, 20s*
77	295G3B undop.	Al_2O_3 (polished) ~100	NIST SOG 50% BTSE	77K	800 ºC, RTA	Split, layer transfer	*Spin: 1500rpm 20s*
78	295G3C undop.	Al_2O_3 (polished) ~100	NIST SOG 50% BTSE	77K	800 ºC, RTA	Split, small layer transfer	*Spin: 1500rpm 20s*
79	295G3D undop.	Al_2O_3 (polished) ~100	NIST SOG 50% BTSE	77K	900 ºC, RTA	Split, layer transfer	*This was run 1st in sequence: TC in RTA bent; temperature measurement may have been off* Spin: 1500rpm 20s

Table B.3, continued:

Trial #	GaAs:N (doping)	Material (μm)	SOG	Impl. *T*	Max. anneal *T*	Bonding/ splitting	*Notes*
80	295G3E undop.	Al_2O_3 (polished) ~100	NIST SOG 50%	77K	800 ºC, RTA	Split, no layer transfer	*Tried bonding w/o spin; just applied with syringe. Debonded during anneal*
81	295G3F undop.	Al_2O_3 (polished) ~100	NIST SOG 50% BTSE	77K	900 ºC, RTA	Split, some layer transfer	*Did not bond at RT on first try Spin: 1500rpm 20s*
82	295G3H undop.	AlN (polished) ~300um	NIST SOG 50% BTSE	77K	800 ºC, RTA	Split, small layer transfer	*Did not bond at RT on first try Spin: 1500rpm 20s*
83	535C3E n-dop.	Al_2O_3 (polished) ~100	NIST SOG 50% BTSE	77K	800 ºC, RTA	Split, some layer transfer	*Spin: 1500rpm 15s*
84	535C3F n-dop.	Al_2O_3 (polished) ~100	NIST SOG 50% BTSE	77K	800 ºC, RTA	No bonding	*Before RTA: low-T cure ~100C for 20min; did not bond. Further cure for ~2h, still no bonding Spin: 1500rpm 15s*
85	535C3J n-dop.	Al_2O_3 (polished) ~100	NIST SOG 50% BTSE	77K	900 ºC, RTA	Split, some layer transfer	*Spin: 1500rpm 15s*
86	535C3K n-dop.	AlN (polished)	NIST SOG 50% BTSE	77K	800 ºC, RTA	Split, no layer transfer	*Spin: 1000rpm 15s*
87	535C3G n-dop.	Al_2O_3 (polished) ~100	NIST SOG 50% BTSE	77K	800 ºC, RTA	Split, layer transfer	*Spin:1000rpm 15s*
88	535C3N n-dop.	GaAs ~600	NIST SOG 50% BTSE	77K	800 ºC, RTA	Split, layer transfer	*Spin:1200rpm 15s*
89	535C3O n-dop.	AlN (polished)	NIST SOG 50% BTSE	77K	800 ºC, RTA	Split, very little layer transfer	*Spin:1200rpm 15s*

Table B.3, continued:

90	535C3P n-dop.	Al_2O_3 (polished) ~100	NIST SOG 50% BTSE	77K	800 ºC, RTA	Split, layer transfer	*Spin:1200rpm 15s*
90	535C3P n-dop.	Al2O3 (polished) ~100	NIST SOG 50% BTSE	77K	800 ºC, RTA	Split, layer transfer	*Spin:1200rpm 15s*
91	IQE-I2-A4 undop.	Al_2O_3 (polished) ~100	NIST SOG 50% BTSE	77K	800 ºC, RTA	Split, layer transfer	*For PL experiments Spin:1200rpm 15s*
92	IQE-I2-A5 undop.	Al_2O_3 (polished) ~100	NIST SOG 50% BTSE	77K	800 ºC, RTA	Split, layer transfer	*Spin:1200rpm 15s*

B.2 References

[1] S. Wolf and R. N. Tauber in: *Silicon Processing for the VLSI Era, Volume 1: Process Technology*. (Lattice Press, Sunset Beach, 1986).

[2] Y. Xiong, Y. Zhou, Z. H. Zhu, Y.-H. Lo, C. Ji, S. A. Basher, A. A. Allerman, T. Hargett, R. Sieg, and K. D. Choquette, IEEE Photon. Technol. Lett. **12**, 110 (2000).

APPENDIX C

Focused-ion-beam (FIB) Lift-out

FIB lift-out is a TEM sample preparation method suited to samples for which only a small area is of interest that may not be accessible by conventional mechanical-grinding methods, such as locally-patterned surfaces. For layer transfer samples, FIB lift-out is performed to target only the areas of layer transfer. All lift-out samples were prepared with a FEI Quanta 200 3D, outfitted with electron-beam and Ga^+ ion-beam columns, a micro-manipulator needle (Autoprobe[1] v. 100.5), and a chemical-vapor-deposited[2] (CVD) Pt deposition system. These components are shown schematically in Fig. C.1, along with a typical lift-out sample consisting of GaAs:N layers transferred to a ceramic substrate with a spin-on glass (SOG) bonding layer.

In all cases, TEM specimens were created by lifting out a rectangular section (shown by the dashed line in Fig. C.1) normal to the sample surface, and extending into the SOG bonding layer and ceramic substrate, in order to view all layers in cross-sectional TEM. To minimize surface charging in high-vacuum

SEM due to the insulating SOG and ceramic layers, samples were sputter-coated with a ~50 Å layer of AuPd or C. In the area to be lifted-out, typically ~2x15 μm, the sample is coated with two layers of Pt which act as protective layers during subsequent FIB-processing. An example of the deposited Pt layer is shown in the SEM image of Fig. C.2(a). First, ~200 nm of electron-beam-assisted CVD Pt is deposited (at a voltage and current of 5 kV and 0.16 nA), followed by ~2 μm of ion-beam-assisted CVD Pt (at 10 kV and 0.21 nA).

The lift-out process is outlined in the following SEM images: first, trenches are milled around the sample, leaving only a tab of material attached, as shown in Fig. C.2(b). This material removal step is typically performed at 30 kV, 5.0 nA. Next, the micro-manipulator needle is welded to the sample surface using ion-beam-assisted CVD Pt (at 10 kV, 0.21 nA), as shown in Fig. C.2(c). The last tab of material keeping the sample attached is then milled away, and the sample lifted out of the trench (Fig. C.2(d)). The sample is then welded to a post on a Cu or Mo grid supplied by Omniprobe[1] and specifically designed for liftout samples, as shown in Fig. C.2(e). Next, the micro-manipulator needle is milled off, leaving the sample attached to the grid as shown in Fig. C.2(f). Finally, the sample is polished with FIB at normal-incidence, as shown in Fig. C.2(g), to a thickness suitable for transmission in XTEM (Fig. C.2(h) and (i). A typical polishing sequence (in terms of FIB voltage and current) consists of a 20 kV, 0.38 nA milling step followed by final polishing steps at 10 kV, 0.12 nA, and 10 kV, 50 pA.

C.2 References

[1] Omniprobe, Inc., Dallas, TX; http://www.omniprobe.com/systems.htm

[2] B. Van Leer, L. A. Gianuzzi, and P. Anzalone, in *Scanning Microscopy for Nanotechnology: Techniques and Applications* (Springer, New York, 2006), p. 231.

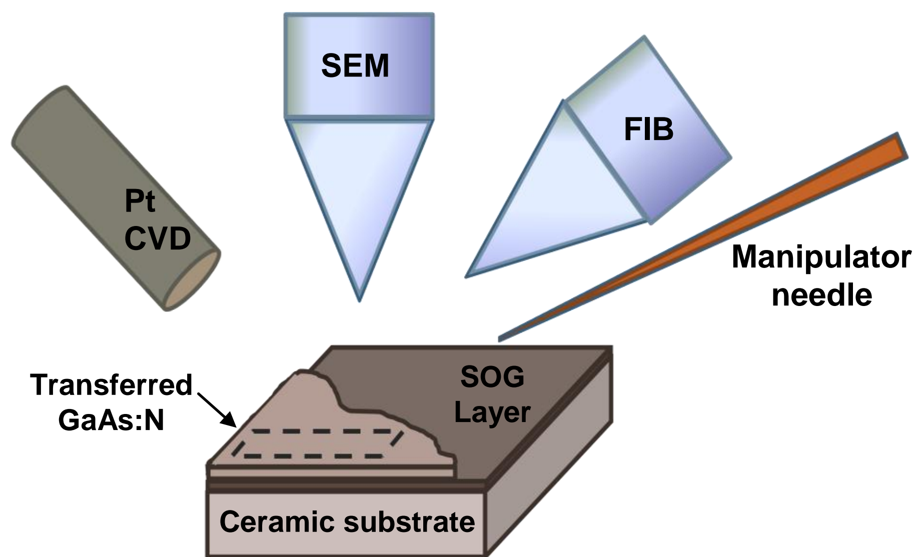

Fig. C.1 Illustration of the components used for FIB lift-out, including electron and focused ion beam columns, a Pt CVD needle, and a micro-manipulator needle for handling the lift-out specimen. An area of layer transfer selected from the sample for lift-out is marked by a dotted line.

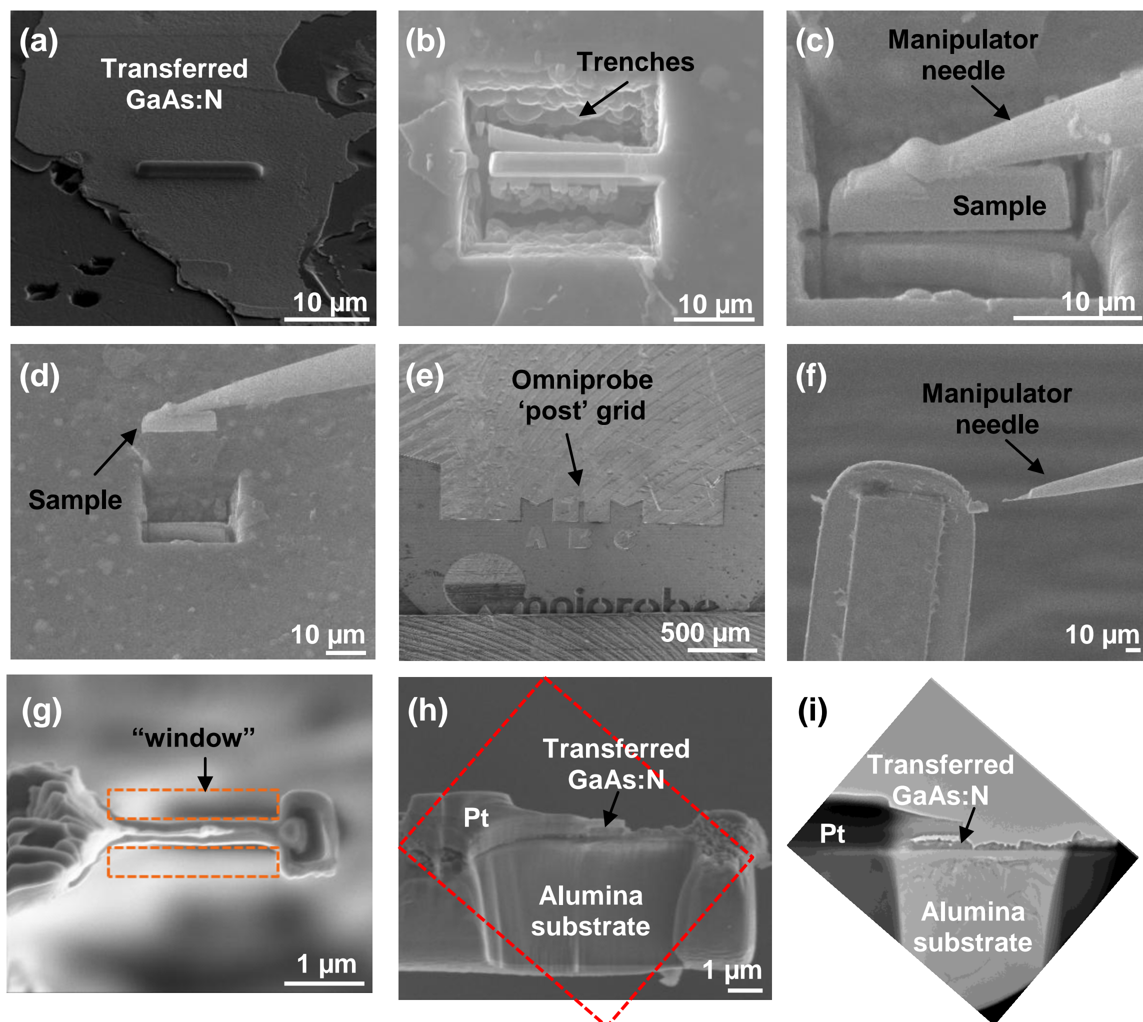

Fig. C.2 (a) – (h): SEM images of the lift-out process for XTEM sample preparation of transferred GaAs:N layers. In (a), Pt is deposited on the surface as a protective layer. The sample area is cut out by FIB-milling trenches, in (b), and a manipulator needle welded to the sample in (c). The last tab of material is then milled away and the sample is removed from the trench (d) and placed on a post grid (shown in (e)). After welding the sample to the grid, the needle tip is milled away by FIB (f). The sample is FIB-thinned and polished in a ~2 μm "viewing window" for TEM using FIB, as shown in normal incidence in (g) and in cross-section in (h). The same sample is shown in an XTEM image in (i), exhibiting sufficient electron transmission for TEM studies.

APPENDIX D

Materials Parameters

D.1 Materials Parameters

This appendix lists the materials parameters used in this thesis work. Various mechanical and physical properties of GaAs, Si, polycrystalline-alumina and polycrystalline-aluminum nitride are given in Table D.1. Table D.2 lists the reported thermal expansion coefficients of several semiconductor and ceramic substrates as a function of temperature. Finally Table D.3 summarizes the predicted and experimental elastic constants of GaAs.

Table D.1: Mechanical and physical properties of the substrate materials used in this thesis work.

	GaAs	Si	Poly-Al_2O_3	Poly-AlN
Young's modulus *E* (GPa)	85.5 (<100> orientation) Ref. 1	129 (<100> orientation) Ref. 2	303 Ref. 2	308 Ref. 3
Poisson's ratio ν	0.31 (<100> orientation) Ref. 1	0.28 (<100> orientation) Ref. 2	0.21 Ref. 2	0.245 Ref. 4
Thermal conductivity κ (at room temperature) ($Wm^{-1}K^{-1}$)	45.5 Ref. 2	141 Ref. 2	25.2 Ref. 5	140 Ref. 6
Lattice parameter (nm)	5.6533 Ref. 1	5.4306 Ref. 7	n/a	n/a

Table D.2: Reported thermal expansion coefficients ($x10^{-6}$ K^{-1}) of several semiconductor and ceramic substrates as a function of temperature (see references in the table).

Temp (°C)	GaAs[8]	poly-Al_2O_3[9]	SiC[10]	poly-AlN[11]	poly-$MgAl_2O_4$[12]	Si[13]	poly-Si_3N_4[14]
20		5.9	2.9	4.03			
30	5.6						
60	5.8					2.69	
100	6				6.3		2.4
120	6.1						
127			4				
140	6.2						
160	6.3					3.39	
190	6.5			4.03			2.4
215	6.6						
226			4.4				
250	6.65				6.5		
270						3.74	
275	6.75						
300	6.7	5.9					2.8
325	6.75		4.7				
350	6.8						
400						3.98	
426			5				
500					7.5		3.6
526			5.1				
580						4.12	
600		7.2		4.84			
726					8.5		

Table D.3: Elastic constants of crystalline and amorphous GaAs (c-GaAs and a-GaAs, respectively), including experimentally-determined values as well as those predicted by molecular dynamics (MD) simulations (see references in the table).

	c_{11} (GPa)	c_{12} (GPa)	c_{44} (GPa)
c-GaAs, experiment[15]	119.0	53.8	59.5
c-GaAs, MD[16]	119.0	53.7	65.8
a-GaAs, MD[16]	98.8	46.6	26.7

D.2 References

[1] J. S. Blakemore, J. Appl. Phys. **53**, R123 (1982).

[2] W. D. Callister, *Materials Science and Engineering: An Introduction,* 6th ed., (John Wiley & Sons, Hoboken, 2003), Appendix B.

[3] D. Gerlich, S. L. Dole, and G. A. Slack, J. Phys. Chem. Solids **47**, 437 (1986).

[4] P. Boch, J. C. Glandus, J. Jarrige, J. P. Lecompte, and J. Mexmain, Ceramics International **8**, 34 (1982).

[5] Cetek Technologies, http://www.cetecktechnologies.com

[6] N. Kuramoto, H. Taniguchi, and I. Aso, IEEE Trans. Components, Hybrids, and Manufacturing Technology **9**, 386 (1986).

[7] B. J. Isherwood and C. A. Wallace, Nature **212**, 173 (1966).

[8] R. Feder, T. B. Light, J. Appl. Phys. **39**, 4870 (1968).

[9] O. J. Whittemore Jr. and N. N. Ault, J. Am. Ceram. Soc. **39**, 443 (1956).

[10] K. Karch, P. Pavone, A. P. Mayer, F. Bechstedt and D. Strauch, Physica B 219-**220**, 448 (1996).

[11] K. M. Taylor and C. Lenie, J. Electrochem. Soc. **107**, 308 (1960).

[12] A. E. Paladino and C. R. Snider, Am. Ceram. Soc. Bull. **49**, 280 (1970).

[13] Y. Okada and Y. Tokumaru, J. Appl. Phys. **56**, 314 (1984).

[14] R. M. Williams, J. Am. Ceram. Soc. **63**, 108 (1980).

[15] R. I. Cottam and G. A. Saunders, J. Phys. C. **6**, 2105 (1973).

[16] I. Ebbsjö, R. K. Kalia, A. Nakano, J. P. Rino, and P. Vashishta, J. Appl. Phys. **87**, 7708 (2000).